2012

Microstructure, rheology, and mixing of suspensions

Bu Xu
Lehigh University

Microstructure, rheology, and mixing of suspensions

by

Bu Xu

Presented to the Graduate Committee and Research Committee

of Lehigh University

in Candidacy for the Degree of

Doctor of Philosophy

in

Chemical Engineering

Lehigh University

May 2012

Approved and recommended for acceptance as a dissertation in partial fulfillment of requirement for the degree of Doctor of Philosophy.

_____
Date

_____
Dr. James F. Gilchrist

_____
Accepted Date

Committee members:

_____
Dr. Anthony J. McHugh

_____
Dr. Hugo S. Caram

_____
Dr. Eugenio Schuster
(Mechanical Engineering and Mechanics)

_____
*

Acknowledgments

This work is conducted under the guidance of my advisor, Dr. James Gilchrist to whom I pay great gratitude and respect. Jim is always positive, supportive and constructive, regardless of my performance. His care surpasses the area of research and work, and instigates me with an energetic spirit.

Dr. Changbao Gao provided me the basic lab trainings before I took over his project, the experimental part of this work. Other people in my lab have been friendly and cooperative. Dr. Pisist Kumnorkaew taught me many tips for doing lab work and cheered me up with his optimism; Alex Weldon supervised my particle synthesis experiments and proof-read my journal paper and PhD proposal; Yajun Ding likes printing many papers and discussing theoretical problems, which benefit me with refreshing knowledge; Tanyakorn Muangnapoh, Tharanga Perera and Midhun Joy are all kind and ready to give a hand.

I also acknowledge collaborators from outside my lab: Prof. Mark Snyder and Zheng Tian; Prof. Anand Jagota and Ying Bai; Prof. Xuanhong Cheng and Bu Wang, Chao Zhao, Krissada.

I would like to express my gratefulness to my course instructors in graduate school, especially Professors Philip Blythe, Anthony McHugh, Anand Jagota, Hugo Caram and Manoj Chaudhury. As the only committee member who has never taught me

in classroom, Prof. Eugenio Schuster is acknowledged for his time in examination of this thesis.

Last but not the least, I will never reach this point without my friends around who seemingly do not have direct contributions to this research. Their friendship always offers momentous joy and hope. They are: Chih-Hsiu Lin, Fan Ni, Shi Wang, Jon Longley, Aishuang Xiang, Gautam Kumar, Reza Arastoo, Yuzhen Yang, Funian Zhao, Chip Roberts, Chris Keturakis, etc.

Contents

List of Figures

Abstract

A concentrated suspension of solid microspheres dispersed in a Newtonian fluid exhibits complex non-Newtonian behaviors. Rheological studies in the past few decades have pointed out that a strong coupling between suspension microstructure and rheology exists. The key to understanding flow property therefore lies in comprehension of microstructural information. However, due to practical difficulties, most previous work on microstructure is produced through numerical simulations.

This study provides an innovative experimental approach based on previous work in our group (Gao *et al.*, 2010; Gao, 2010), which combines confocal microscopy and microfluidics. The former allows for accurately resolving local structure and the latter enables high shear-rate conditions. This method yields highly consistent microstructural data in terms of the pair distribution function with previous numerical studies. Viscometric functions are calculated in the light of the known pair distribution, and qualitative agreements are established. Our results also testify between two competing mechanisms about the shear-thickening of suspensions, namely hydrocluster formation (Brady & Bossis, 1985) and order-disorder transition (Hoffman, 1972). Our findings strongly supports the former and a nearly linear correlation between the hydrocluster size and Pe is found. Existence of shear-induced crystallinity in our experiment does not support the order-disorder transition as the mechanism of

shear-thickening.

As a consequence of the microstructure in sheared suspensions, an interesting phenomenon, namely shear-induced migration occurs in nonlinear shear field. Shear-induced migration has been modeled as either a diffusive process (Leighton & Acrivos, 1987*b*) or a stress relaxation (Nott & Brady, 1994). Shear-induced migration has significant effects on practical handling of suspensions as it causes inhomogeneity out of uniform concentration and thus complicates the rheology. The demixing nature of shear-induced migration in one-dimensional straight channel is explored based on a suspension stress model (Morris & Boulay, 1999) with a fitting parameter obtained from experimental data (Gao *et al.*, 2009). A systematic investigation on the interplay between chaotic advection and shear-induced migration is then carried out for a suspension confined in a two-dimensional rectangular container using a diffusive-flux model developed by Phillips *et al.* (1992). Variation of relative strength between the flow topology and migration generates various patterns of concentration distribution. This study reveals the limitation of conventional wisdom in chaotic mixing of Newtonian fluids and heralds mixing of suspension as a new area for investigation.

Chapter 1

Introduction

The behavior of materials when subjected to stress are commonly delineated as solid- or fluid-like. However, this clear distinction in everyday life is questioned by modern rheology, e.g. when a system of mixture of the two is encountered. Properties of solids and fluids often coexist in these mixtures, which produces fascinating versatility. Humans began to realize the intriguing nature of such systems in primeval time. Mythological accounts for creation and human origin are often involved with suspensions or systems alike. For example, Chinese myth states people were created by the goddess Nü-Wa out of mud; the Wyandot Indians tell a story in which Toad spit on the back of Big Turtle a bit of soil she dived to obtain underwater and this little solid mass eventually grew into a huge island, that is today's North America (*Native Universe– Voices of Indian America*, edited by G. McMaster and C. E. Trafzer); by throwing stones over their shoulders onto flooded land, the Greek legendary couple Deucalion and Pyrrha gave birth to the first men and women of our epoch (*Bibliotheca*, Pseudo-Apollodorus); the most well-known is probably the biblical account: "And the LORD God formed man of the dust of the ground, and

breathed into his nostrils the breath of life; and man became a living soul" (Genesis **2**:7, KJV). It appears that in the dawn of civilization, people had already grasped that combination of solidity and fluidity produces flexibility and complexity that to a great extent constitute, sustain and replenish the world and ourselves.

One simplest solid-fluid system is a suspension: solid particles dispersed in a fluid phase. Suspensions are ubiquitously encountered and applied in natural and artificial processes. Humans, through adaptation in their ability to control their environment, have necessarily developed a working understanding of geological suspensions, e.g. rivers, mudslides and volcanic lavas. Likewise, through early industrialization of consumer goods such as porridge, tea, soup, curd, herbal medicine, pottery, ink, paper, paint, plaster, cement, rubber, fiber and skincare products, the challenges of processing suspensions commonly enters daily life. Moving from small batch-wise processing using heuristics largely derived from trial-and-error observations to the industrial era strongly motivates the ability to develop constitutive equations that enable process scalability. Because of these ongoing needs, the establishment of rheology of suspensions as a modern science was inevitable.

Along the line from Archimedes, Newton, Bernoulli, Euler, Lagrange and Stokes, fluid mechanics reaches its maturity, rendering scientific analysis on suspension systems. Sir George Stokes' calculation of the drag force by a viscous flow passing a sphere (or a sphere translating in quiescent fluid), namely Stokes' law, sets out the starting footstep into suspension hydrodynamics. His student, Sir Horace Lamb gave the solution of Stokes equation in spherical coordinate using spherical harmonic functions (Lamb, 1932), which provides the basis for study of suspension mechanics.

A boom time for modern sciences, the twentieth century has seen this area of research greatly extended in various directions. The author will discuss developments in people's understanding to suspension systems; and although a general definition of suspensions span many physical situations, this thesis will focus on the ideal case of a stable dispersion of equal sized rigid spheres in a Newtonian fluid limited to flows having vanishing inertia. Particles have roughly the same density as the fluid and their interactions with the fluid can be either purely hydrodynamic or a combination of hydrodynamic, Brownian, and repulsive electrostatic inter-particle interactions.

1.1 Computational Hydrodynamics

Consider a single solid particle situated in a flow of Newtonian fluid under low Reynolds number. The rigidity of solid will resist deformation from the fluid phase and create a velocity disturbance; the resulting force and torque are given by Faxén's laws (Happel & Brenner, 1965). In a series of articles, Brenner solves the Stokes resistance, i.e. force, torque and stress of a single particle in unbounded fluid, covering arbitrary-shaped particle (Brenner, 1963, 1964*a*) in uniform shearing flow (Brenner, 1964*b*) and arbitrary flows (Brenner, 1964*c*, 1966). These results are applicable only to very dilute conditions. Particles interact with each other through the fluid medium because their rigidity alters the flow field from that of a pure fluid, which in turn disturbs the velocity of all other particles. This hydrodynamic interaction is the key interaction between particles, scaling as $1/r^2$, and is responsible for the rich variety of physical properties of flowing suspensions. Although thought to be mathematically described exactly, hydrodynamic interaction is known for its difficulty to approach through analytical methods.

Study of two-particle interaction, though in the infinitely dilute regime, bridges our understandings into concentrated conditions. Lin *et al.* (1970) used general solution of Stokes equation in bipolar spherical coordinates to study interaction between two spheres in a shear field. Batchelor & Green (1972*b*) presented a simpler approach in which the authors gave general forms for the unknowns, i.e. the relative translational velocity, rotational velocities and force dipole strengths of two spheres with arbitrary radii in a linear flow field. The scalar coefficients involved in these forms are calculated for far- and near-field conditions. The relative trajectories between two

equal spheres are also analyzed to reveal that in a linear shear flow, two spheres are easily swept to proximity by the ambient shearing motion, confirming earlier experimental observation (Darabaner & Mason, 1967). Batchelor carried on this method to study Brownian motion in one of his later publications (Batchelor, 1976), where the pair-interaction is posed as a mobility problem and can be written as (not originally in the paper)

$$\mathbf{u} = \mathbf{b} \cdot \mathbf{f} \tag{1.1}$$

where $\mathbf{u} = [\mathbf{u}_1 \ \mathbf{u}_2]^T$ is the velocity vector for two spheres, and $\mathbf{f}$ the force vector; $\mathbf{b}$ is the coefficient tensor containing the configuration-dependent scalars which later are called mobility functions.

On the other hand, Brenner & O'Neill (1972) formulated the pair/multi-particle hydrodynamics in terms of a resistance problem by extending Brenner's method for single-particle analysis:

$$\mathbf{F} = -\mu[\mathbf{R} \cdot \mathbf{U} + \Phi \cdot \rho] \tag{1.2}$$

Here $\mathbf{F}$ is the force-torque vector, $\mathbf{U}$ the velocity-spin vector, ρ the rate-of-strain vector/tensor and μ the viscosity of the fluid. Scalar coefficients, or resistance functions, which describe the linear relation between kinematics(translational/angular velocities and rate of strain) and mechanics(force and torque) and depend on particle geometry and system configuration, are arrayed in the two matrices $\mathbf{R}$ and Φ.

Tabulation of these mobility and resistance functions (Jeffrey & Onishi, 1984; Kim & Mifflin, 1985) claims the pair-interaction problem. However, analytic methods generally fall short on many-body hydrodynamic interactions due to the overwhelming computational load. Thanks to the development of computer technology in last

century, people were able to develop numerical tools for computing and simulating multiparticle hydrodynamics. Durlofsky *et al.* (1987) resolved the many-body effect by inversion of the grand mobility matrix M, defined in the mobility problem:

$$\begin{bmatrix} \mathbf{U} - \mathbf{U}^{\infty} \\ -\mathbf{E}^{\infty} \end{bmatrix} = M \cdot \begin{bmatrix} \mathbf{F} \\ \mathbf{S} \end{bmatrix} \tag{1.3}$$

where $\mathbf{U}^{\infty}$ is the velocity-spin vector of the undisturbed flow field, $\mathbf{E}^{\infty}$ the undisturbed rate-of-strain tensor; $\mathbf{U}$, $\mathbf{F}$ and $\mathbf{S}$ are the N-particle velocity-spin vector, force-torque vector and stresslet tensor, respectively.

The near-field lubrication is solved in a pairwise fashion based on aforementioned results for the two-body problem. Combination of the two constructs the grand resistance matrix and therefore solves the whole resistance problem:

$$\begin{bmatrix} \mathbf{F} \\ \mathbf{S} \end{bmatrix} = R \cdot \begin{bmatrix} \mathbf{U} - \mathbf{U}^{\infty} \\ -\mathbf{E}^{\infty} \end{bmatrix} \tag{1.4}$$

This methodology, termed Stokesian Dynamics (Brady & Bossis, 1988) provides accurate reflection of actual particle interactions in flows and is widely recognized as a powerful tool for study of suspensions. Brady and coworkers have also developed a variant version(Accelerated Stokesian Dynamics, or ASD) for faster CPU time (Sierou & Brady, 2001; Banchio & Brady, 2003). Application of SD/ASD to low-Reynolds-number suspension systems successfully predicts and reproduces phase transition, migration (Nott & Brady, 1994) and numerous rheological behaviors to be mentioned later.

Other notable numerical methods include Dissipative Particle Dynamics (Hoogerbrugge & Koelman, 1992; Pan *et al.*, 2010), the lattice Boltzmann (Chen & Doolen, 1998; Ladd & Verberg, 2001; Aidun & Clausen, 2010) and Boundary-Multipole Collocation methods (Kim & Karrila, 1991), etc.

1.2 Colloid science

A system with micron- or submicron-sized particles(e.g. particles, drops and bubbles) dispersed in a fluid, is usually referred to as a "colloid" which is transliterated from the Greek word $\kappa\acute{o}\lambda\lambda\alpha$, meaning glue (Russel *et al.*, 1989). Recent decades have seen surging research activities on colloids. Leave alone practical reasons that colloids are encountered in many fields, e.g. environmental engineering, catalysis, food industry, optics and bioengineering, what makes them theoretically appealing is the close similarity and even scalability between colloidal and atomic systems (Kose *et al.*, 1973; Arora & Tata, 1998). Since the former is much easier to control and monitor, study of model colloidal systems provides precious insight for condensed-matter physics (Murray & Grier, 1996). Colloidal systems are also fascinating on their own account by demonstrating intriguing phase behaviors, which is the result of interplay between various forces present in the system (Russel *et al.*, 1989; Murray & Grier, 1995).

When the length scale goes down to that of colloidal particles, certain forces become pronounced to take effect in the behavior of colloidal suspensions. These forces arise from thermal agitation of solvent molecules (Brownian or thermal force), surface charge or potential on colloidal particles (electrostatic force), summation of London- van der Waals force (dispersion force), interaction between adsorbed polymer chains (steric force) and exclusion of non-adsorbing polymers between two particle surfaces (depletion force), etc. In suspensions without polymer in the solvent, the first three are predominant, illustrated in more details herein.

1.2.1 Brownian force

Brownian motion is the constant random movement of colloidal particles as a consequence of the molecular agitation from the solvent. Diffusion, a familiar and important process, originates from Brownian motion. Combining the thermodynamic concept of osmotic pressure and Stokes' Law in fluid mechanics, in 1905 Einstein (1926) obtained the Stokes-Einstein-Sutherland formula for diffusion coefficient of an isolated sphere with radius a in a fluid of viscosity η:

$$D = \frac{kT}{6\pi\eta a} \tag{1.5}$$

where $k = 1.38 \times 10^{-23} K^{-1}$ is the Boltzmann constant and T is absolute temperature.

On the other hand, from a dynamic viewpoint, the well-known Langevin equation gives a Newtonian force-balance account for Brownian motion of a spherical particle having mass m and radius a:

$$m\frac{d^2\mathbf{x}}{dt^2} + 6\pi\eta a\frac{d\mathbf{x}}{dt} = \mathbf{f}(t) \tag{1.6}$$

The Brownian force $\mathbf{f}$ is random and satisfy (Russel *et al.*, 1989)

$$< \mathbf{f}(t) >= \mathbf{0} \tag{1.7}$$

$$< \mathbf{f}(t)\mathbf{f}(t+\tau) >= 12\pi\eta akT\mathbf{I} \tag{1.8}$$

where $\mathbf{I}$ is the second-order identity tensor.

A useful dimensionless number quantifying the relative strength between hydrodynamic and Brownian force is the Péclet number

$$Pe = \frac{\dot{\gamma}a^2}{D} = \frac{6\pi\eta\dot{\gamma}a^3}{kT} \tag{1.9}$$

Pe characterizes the state of suspension in that it is zero when the system is at equilibrium and approaches infinity in suspensions of large particles, viscous fluids and high shear rates conditions.

1.2.2 Electrostatic force

When put in an ionic solution, almost all solid surfaces will become charged due to various mechanisms (Russel *et al.*, 1989), e.g. preferential adsorption of certain species. The charged surface attracts free ions in the liquid phase to form a double layer: an inner immobilized layer of predominately counterions (the Stern layer) and an outer layer of ions of the same sign as the surface charge (the diffuse layer) (Adamson & Gast, 1997). When the suspension is under shear, the Stern layer around a particle is not affected and the mobilized shear layer lies somewhere outside the division between the Stern and diffuse layers.

It is not always easy to measure the surface potential, and the potential at the shear layer, the zeta-potential ζ becomes a frequently-used parameter to determine the electrostatic force. For a stable colloidal suspension, ζ typically ranges from 10 to 100 millivolts.

Another important parameter is the Debye length κ^{-1}, which is the characteristic thickness of the electrical double layer. Over this distance away from a particle, the electrical field is essentially unfelt because of screening of free ions. Debye length is given as (Russel *et al.*, 1989):

$$\kappa^{-1} = \sqrt{\frac{\epsilon\epsilon_0 kT}{2e^2 \sum n_i z_i^2}} \tag{1.10}$$

where $\epsilon\epsilon_0$ is the dielectric constant of the medium, $e = 1.60 \times 10^{-19} C$ is the elementary charge, n_i and z_i are number density and valence of species i.

Eq. 1.10 indicates that κ^{-1} can be controlled by manipulating ionic strength.

Electrostatic repulsion between particles is crucial in stabilizing the suspension

in that the ever-present, attractive dispersion force will pull particles together to form clusters and aggregates under low ζ and small κ^{-1} conditions. Dispersion force, also called London-van der Waals force, arises from the dipole-dipole interactions on atomic or molecular level. However, the integral effect renders dispersion force long-range and attractive on colloidal length scale. Competition between dispersion and repulsive forces determines the stability of a colloidal suspension, resulting in complicated phase behaviors. The influential theory due to Derjaguin, Landau, Verwey and Overbeek (DLVO theory) sums attractive and repulsive forces into an interparticle potential to explain colloidal stability.

This research involves with charge-stabilized colloidal suspensions well above the stability criterion, so dispersion force is considered insignificant. Instead we will be mostly focused on the interplay between electrostatics and hydrodynamics. A dimensionless number representing comparison between these two may be defined in a similar way as Eq.1.9 (Stickel *et al.*, 2006).

$$\gamma^* = \frac{6\pi\eta\dot{\gamma}a^2}{F_0} \tag{1.11}$$

where F_0 is the characteristic magnitude of the electrostatic repulsive force.

Many of the works mentioned in Section 1.3 are carried out with colloidal suspensions. However, the influence from the Brownian and interparticle forces further complicates the measurement or computation and it is clear that any sound rheological model must not neglect careful characterization of the colloidal forces (Jeffrey & Acrivos, 1976). As a matter of fact, the impact of interparticle forces on rheology is evident (Russel, 1980). For example, the electroviscous effect, effect of particle electrostatic interactions on rheology, has been a long-standing interest since the work of

Stone-Masui & Watillon (1968) which reveals an enhanced low-shear viscosity due to electrostatics at dilute concentration. Systematic studies (Berend & Richtering, 1995; Horn *et al.*, 2000) have shown a transition from elastic to viscous behaviors as ionic strength is dropped. In light of the discussions in Section 1.3 about microstructure-dependent rheology of suspensions, these findings suggest a significant role played by electrostatic force in determining the microstructure. An investigation of this effect will be essential for construction of a predictive rheological theory, which is still lacking (Russel, 2009).

1.3 Rheology

A newly emerged science in the twentieth century, rheology studies deformation and stress in materials typically displaying both fluidity and solidity. After decades of evolution, this discipline has developed a uniquely insightful view of flowing matters and had at its disposal a variety of theoretical and experimental tools which are readily applicable to suspensions. In the scope of rheology, particulate suspensions are fully illuminated such that their properties are classified and characterized in an unprecedented, rigorous scientific manner.

Initiation of suspension rheology actually predates the formal establishment of "rheology" as a proclaimed subject in 1929. Originally published in German language in 1906, Einstein (1926) proposed a relation between viscosity and volume fraction for a suspension of isolated hard spheres,

$$\frac{\eta}{\eta_0} = 1 + 2.5\phi + O(\phi^2) \tag{1.12}$$

where η_0 is viscosity of the interstitial fluid.

For decades, this achievement had led researchers to strive for a full functional description of η vs. ϕ which would asymptote to Eq.1.12. One widely accepted result (Krieger, 1972) out of such endeavor gives:

$$\eta_{1r} = (1 - \phi/0.68)^{-1.82} \tag{1.13}$$

$$\eta_{2r} = (1 - \phi/0.57)^{-1.50} \tag{1.14}$$

where η_{1r} and η_{2r} are steady-state relative viscosities for high-shear and zero-shear

limit, respectively.

The constants 0.68 and 0.57 in Eqs. 1.13 and 1.14 are considered maximum volume fraction of a suspension before a suspension jams and loses it flowability, or in other words, its viscosity diverges. The exact value of this quantity is still under debate.

While empirical relations like Eqs.1.13 and 1.14 can be made through curve-fitting of experimental data, theorists had little breakthrough until Batchelor & Green (1972*a*) extended Einstein's result to less dilute condition by consideration of pair-interactions and obtained the exact coefficient for the second-order term. However, the volume-fraction dependence of viscosity is inadequate to characterize the rheology. In fact, Krieger (1972) certainly demonstrates that viscosity is shear-rate- and time-dependent as well. Rheological experiments on suspensions in steady shear flow reveal shear-thinning behavior at intermediate shear rate (de Kruif *et al.*, 1985; van der Werff & de Kruif, 1989; Gondret & Petit, 1996) and thickening at high shear rate (Hoffman, 1972; D'Haene *et al.*, 1993; Bender & Wagner, 1996). Normal (Zarraga *et al.*, 2000) and yield stresses (Heymann *et al.*, 2002) have been measured in concentrated suspensions as well. Oscillatory shear experiments also discovered thixotropy (Gondret & Petit, 1996) and strain-dependent behavior in complex viscosity (Breedveld *et al.*, 2001; Bricker & Butler, 2006) and normal stresses (Narumi *et al.*, 2002). Generally the viscosity of a suspension follows the trend in Fig. 1.1: stays constant near equilibrium, first decreases and then increases dramatically with shear rate.

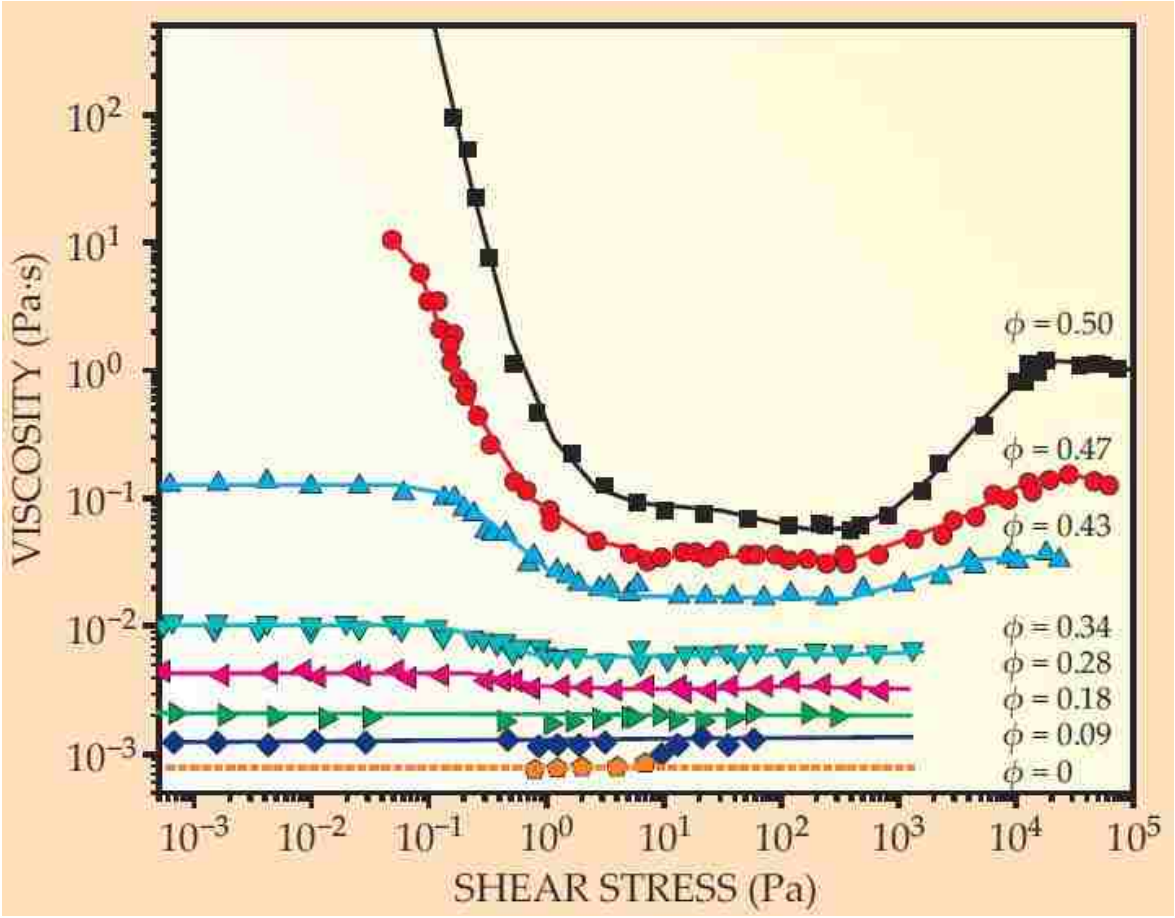

Figure 1.1: Variation of viscosity of a typical suspension with shear rate (Wagner & Brady, 2009).

Hoffman (1972) conducted light-scattering experiments coupled with rheological measurement when he observed an abrupt change in diffraction pattern associated with the outset of a discontinuous shear-thickening process. Hoffman concluded that an order-disorder transition in the suspension microstructure is responsible for its rheology. This finding led people to realize the coupling between suspension microstructure and rheology, and has influenced this area of research ever since. On the other hand, conventional rheological experiments also strongly suggest a microstructure-dependent behavior, most pronounced in the transient nonlinear response when the shear on suspension is reversed (Gadala-Maria & Acrivos, 1980; Breedveld *et al.*, 2001; Narumi *et al.*, 2002, 2005; Blanc *et al.*, 2011). For example, Fig. 1.3 shows in the experiment by Gadala-Maria & Acrivos (1980) it is found that when shearing is stopped, and then restarted in the original direction, the measured torque rapidly reaches its steady-state value; whereas if shear is restarted in opposite direction, the torque will readjust as a function of strain until the same steady-state value is achieved. This phenomenon infers a microstructure retainment for the first case and destruction and reformation for the second, clearly impacting a proper description of microstructure-dependent rheology.

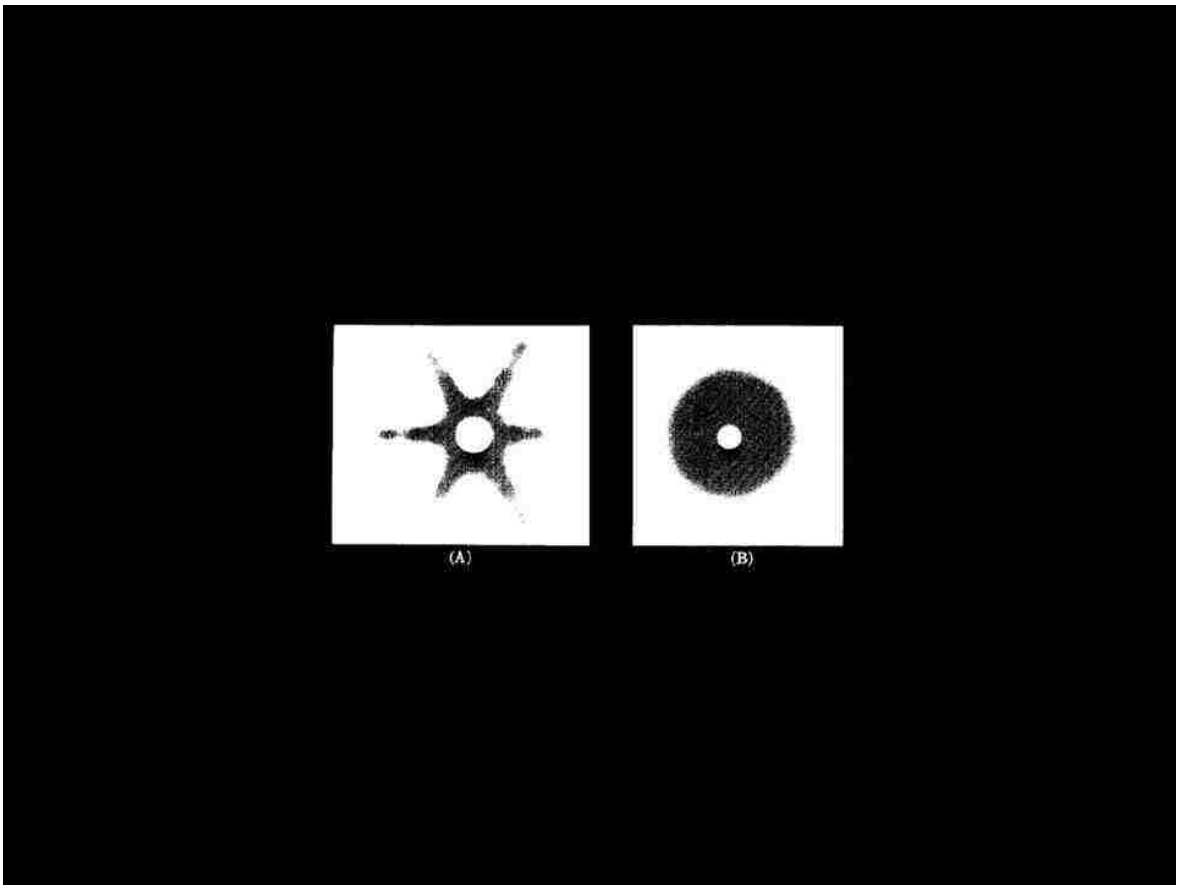

Figure 1.2: Light diffraction pattern before (A) and after (B) shear-thickening (Hoffman, 1972).

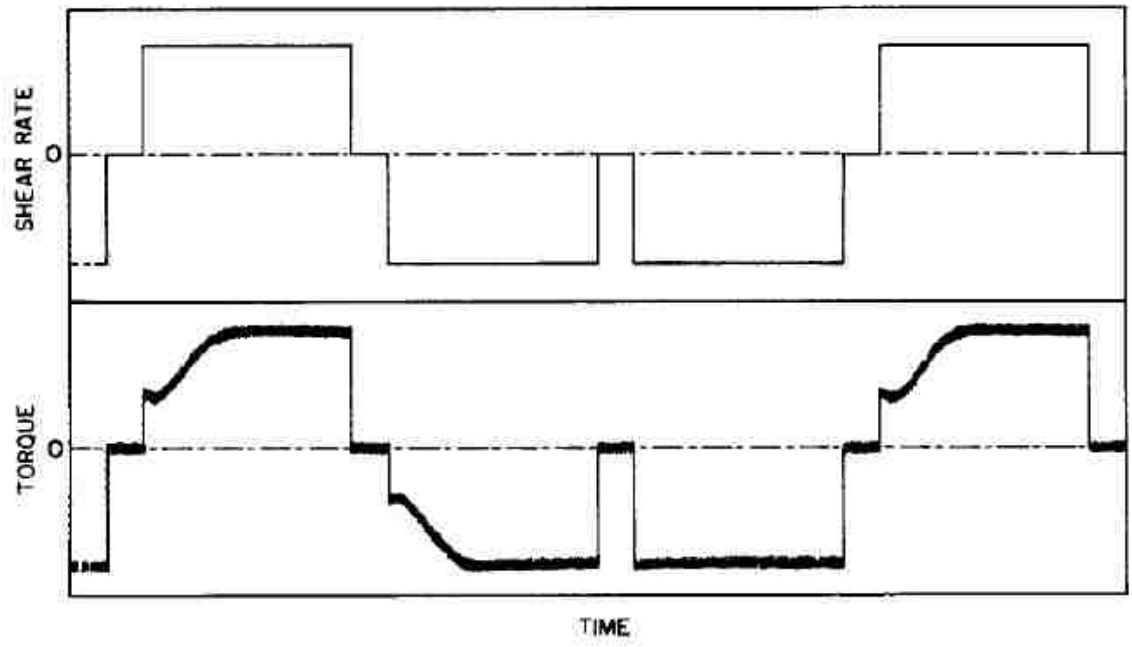

Figure 1.3: Measured torque and shear rate of a concentrated suspension in Couette device; transients only appear when shear is reversed (Gadala-Maria & Acrivos, 1980).

In a suspension of solid spheres, microstructure means the spatial arrangement of particles with respect to each other. A complete description of the microstructure is the N-particle configuration probability, $P_N(\mathbf{x}_1, \mathbf{x}_2 \cdots, \mathbf{x}_N)$, of which the evolution obeys the Smoluchowski equation (Morris, 2009),

$$\frac{\partial P_N}{\partial t} + \nabla_\alpha \cdot \mathbf{j}_\alpha = 0 \tag{1.15}$$

where $\mathbf{x}_\alpha$, $\alpha = 1, 2 \cdots, N$ are particle locations, and $\mathbf{j}_\alpha$ is probability flux related to particle α.

The difficulty in solving Smoluchowski equation or obtaining P_N is obvious, consequently the simplest and most readily used function to represent microstructure is the pair distribution function (Batchelor & Green, 1972*a*), $g(\mathbf{r})$, obtained by integrating P_N over $N-2$ particles. Analytic theory on microstructure is only available for conditions with low concentration or pairwise hydrodynamic interactions (Russel & Gast, 1986; Brady & Morris, 1997).

At pair level, it is believed the hydrodynamic interaction is reversible (Batchelor & Green, 1972*a*), though interparticle forces arising from factors like surface roughness (Rampall *et al.*, 1997; Popova *et al.*, 2007) may incur irreversibility. At high concentration, the pairwise approach does not suffice to describe the system and irreversible interaction arises due to the chaotic nature of multibody effects (Leighton & Acrivos, 1987*b*). For instance, Husband & Gadala-Maria (1987) reports fore-aft symmetry in microstructure of dilute suspension as opposed to the asymmetry in concentrated suspension (Parsi & Gadala-Maria, 1987). Pine *et al.* (2005) reveals there is a concentration-dependent threshold of irreversibility in the total strain experienced by a suspension. When shear rate and volume fraction are high, strong irreversibility

and structure asymmetry are expected. Numerical and experimental studies have confirmed this hypothesis based on obtained $g(\mathbf{r})$ for concentrated suspensions under high shear rates.

One of the earliest appearing in the literature is based on light scattering by Parsi & Gadala-Maria (1987), which shows a fore-aft asymmetry of $g(\mathbf{r})$ on flow-gradient plane(Fig. 1.4). Rampall *et al.* (1997) utilized laser imaging method to measure the pair-distribution function in dilute or semidilute suspensions of noncolloidal spheres, focusing on the effect of particle surface roughness that renders particle interactions irreversible and causes anisotropy. Small-angle neutron scattering (SANS) method is also an effective way to study microstructure of flowing suspensions (Ackerson *et al.*, 1986; Butera *et al.*, 1996; Newstein *et al.*, 1999). Experimental results, although qualitatively agree with those obtained by Stokesian Dynamics simulations (Foss & Brady, 2000; Morris & Katyal, 2002; Wagner & Brady, 2009), generally suffer from relatively large scatter of data, coarse quality and inability to resolve 3D structure, as is evidenced in Fig. 1.4. Recently a high-resolution experimental procedure was proposed by Gilchrist and coworkers (Gao *et al.*, 2010; Gao, 2010). This technique combines confocal laser imaging and microfluidics and is able to produce simulation-level quantitative results for $g(\mathbf{r})$, as is outlined in Chapter 2.

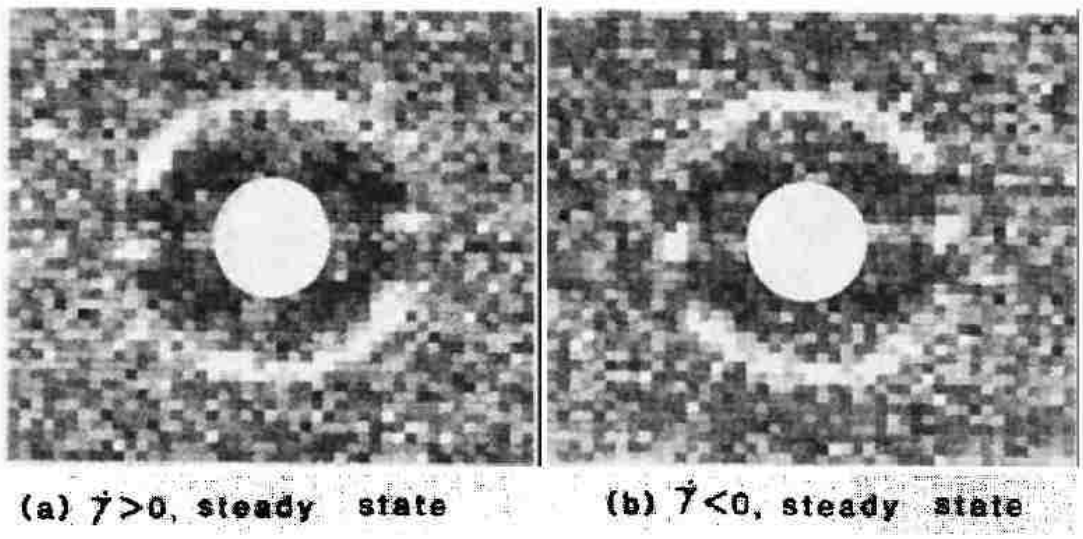

Figure 1.4: Experimentally obtained pair distribution function on **v**- ∇**v** plane showing a broken fore-aft symmetry (Parsi & Gadala-Maria, 1987).

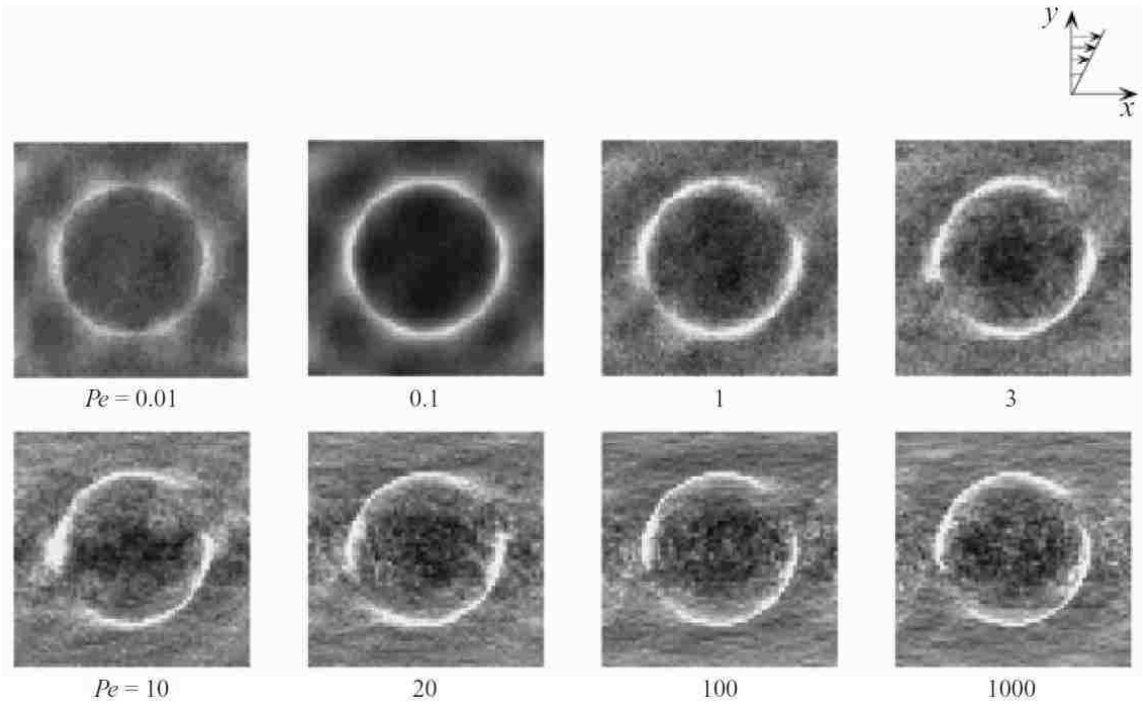

Figure 1.5: Anisotropic microstructure of sheared suspension displayed by pair distribution function on $\mathbf{v}$- $\nabla\mathbf{v}$ plane. From Stokesian Dynamics simulation in Foss & Brady (2000).

Besides shear viscosity, normal stress differences are also important viscometric functions:

$$N_1 = \Sigma_{11} - \Sigma_{22} \tag{1.16}$$

$$N_2 = \Sigma_{22} - \Sigma_{33} \tag{1.17}$$

where Σ is the total stress tensor, and subscripts "1", "2" and "3" respectively refer to directions of flow, velocity gradient and vorticity.

For Newtonian fluids under shear, the deviatoric normal stresses are identically zero. In polymer solutions and melts, normal stresses arise from the elasticity of the polymer chains which are stretched along flow direction. Because of the tensile nature of molecular resistance to this stretching, the first normal stress difference N_1 is generally large and positive (Tanner, 2000). The second normal stress difference N_2 is often negative and much smaller. For convenience people scale N_1 and N_2 with $\dot{\gamma}^2$.

For noncolloidal suspensions, the circumstance is different. Interactions happen mostly along direction of velocity gradient when particles with relative velocities pass each other, producing an effective "dilatancy". The compressive normal stress in velocity-gradient direction therefore gives rise to a large and negative N_2. Also N_1 and N_2 will scale with $\dot{\gamma}$ as the hydrodynamic interaction does. SD/ASD simulations (Singh & Nott, 2000; Sierou & Brady, 2002) and experiments (Zarraga *et al.*, 2000) demonstrate that N_1 and N_2 are both negative and the former is smaller in magnitude; while for colloidal systems N_1 changes to positive sign when Brownian motion starts to dominate (Foss & Brady, 2000).

The normal stresses generated in sheared suspensions entail cross-streamline motions of particles, or shear-induced particle diffusion (Eckstein *et al.*, 1977; Leighton & Acrivos, 1987*a*). This diffusive motion is caused by interactions between particles and therefore is stronger than the Brownian diffusion by thermal fluctuation of the much-smaller solvent molecules. Shear-induced diffusion has profound influences on suspension-related processes, e.g. viscous resuspension (Leighton & Acrivos, 1986). Interestingly, since normal stresses scale with shear stress (Zarraga *et al.*, 2000) and increases with ϕ, if shear gradient exists in the flow, imbalance of normal stress (or shear-induced diffusion flux) will drive particles from high-shear to low-shear areas, a phenomenon called shear-induced migration (Leighton & Acrivos, 1987*b*). The resulting inhomogeneity in particle distribution is theoretically interesting and raises concerns for practical consideration as well. Chapter 5 will address problems involving shear-induced migration to great extent.

1.4 Thesis layout

This dissertation is arranged as follows: Chapter 2 describes the complete procedures for experimental investigation on suspension microstructure; subsequently Chapter 3 presents the results and discusses our acquired understanding from a fundamental point of view; a connection into reality is made in Chapter 4 by a study of demixing caused by shear-induced migration as a consequence of the microstructure-dependent rheology; finally Chapter 5 attempts to suppress demixing by introducing chaotic advection and demonstrates results that are potentially illuminative for practical handling of suspensions.

Chapter 2

Methods

The experimental procedure can be streamlined into three parts: 1) preparation of silica microspheres, and then making suspensions using these particles; 2) fabrication of PDMS-based microfluidic device; 3) flowing the suspensions into the device and scanning the sample with confocal microscope. Each step is elaborated as follows.

2.1 Synthesis of fluorescent particles and preparation of suspension

We performed Stöber synthesis (van Blaaderen & Vrij, 1992) to fabricate silica microspheres . The procedure is summarized as follows.

1) Preparation of dye: 32 mg of RITC (Rhodamine B isothiocyanate, Sigma-Aldrich) and 0.07 ml liquid APS (3-aminopropyl-triethnoxysilane, Acros, 99%) were dissolved into 7.5 ml 200-proof ethanol in a small vial wrapped with aluminium foil. The solution was stirred for 12 hours in order for bonding reaction between APS and

the fluorescent RITC to be completed.

2) Synthesis of fluorescent cores: A base solution consisting of 17.28 ml 200-proof ethanol, 24.88 ml deionized water and 7.81 ml ammonia hydroxide (NH_4OH) was prepared in a 250 ml HDPE bottle. The dye solution prepared in 1) was added into the base. 4.52 ml TEOS (tetraethyl orthosilicate, Aldrich, reagent grade 98%) was dissolved in 45.48 ml ethanol and gently poured into the batch while the system was stirred vigorously and smoothly by a magnetic stir bar. The hydrolysis of TEOS produces solid silica particles, which keep growing with the reaction. The dye-bonding APS hydrolyzes at a slower rate, rendering the particle fluorescent.

The system was kept being stirred during the whole process. TEOS/ethanol solutions with the same composition were added periodically into the bottle and after each addition the system was left for reaction for at least 6 hours.

3) Collection of core particles: After three additions, the particles look very monodisperse under scanning electron microscope with an average diameter of 520 nm, ideal for imaging purpose. The batch was then stopped and centrifuged to separate out the fluorescent particles. The particles were washed by ethanol and DI water for several times and dispersed in 200-proof ethanol to form a suspension with volume fraction ϕ=0.33.

4) Core-shell restart: The same base solution in 2) was again prepared in a clean HDPE bottle. 3 ml of the well-dispersed fluorescent particle suspension was added in order to provide seed particles. The system being well stirred, the same addition and reaction of TEOS/ethanol solution as in 2) was repeated. Samples were taken for SEM imaging every one or two additions to make sure good particle growth. After five additions the particle average diameter reached 880 nm with a satisfactory

monodispersity. The solution was then centrifuged and washed many times to harvest a batch of clean silica microspheres with fluorescent cores.

Such core-shell structure is crucial in controlling species in suspension and sustaining imaging requirement in our experiments: by sealing the fluorescent with a shell of pure silica, contamination from dye has been avoided.

Dried particles were mixed with a liquid mixture of glycerol and water (volume ratio 3:1) which has the same refractive index as silica. Proper amount of solutions of sodium hydroxide (NaOH) and sodium chloride (NaCl) were added to the suspension so that the pH=8 and [NaCl]=10^{-3} M. This configuration makes sure the suspension is charge-stabilized, but the screening length is small compared with particle size (the Debye length κ^{-1}=8 nm). A colloidal system like this approximates a hard-sphere suspension where interparticle force is present only if particles touch one another.

Before being pumped into microchannel, the suspension was sonicated for sufficiently long time till appearing stable, clear and homogeneous.

2.2 Flow device

Straight microchannels with a rectangular cross section were molded from a silicon wafer mask having two-level etched structures, fabricated at Cornell Nanoscale Facility by Dr. Changbao Gao. Two plastic connectors (Harvard Apparatus) filled with water are put at each end of the ridge structure on the wafer to serve as inlet and outlet. Next, polydimethylsiloxane (PDMS, Dow Corning) mixed with proper amount of curing agent was gently poured onto the wafer and cured at 80°C for at least 60 minutes. We treated the solidified structure and a glass coverslip(cleaned by Piranha solution beforehand) in a plasma cleaner (Harrick Plasma) for 45 seconds and subsequently attach the two together to form a closed channel structure which has a dimension of 100 μm×40 μm×50 mm(width×height×length). The channels were kept for at least 48 hours before usage in order to neutralize charges generated during plasma-bonding. Fig. 2.1 depicts a typical straight microchannel for the flow experiment.

The suspension would be injected into channel inlet and compressed nitrogen be connected to drive the suspension flow. An electropneumatic converter (Omega Engineering) transforming analytic signal to pneumatic response was interfaced with a PC, which enabled us to control the nitrogen flow precisely and smoothly. Such setting allowed quick flow cessation with minimal reversal.

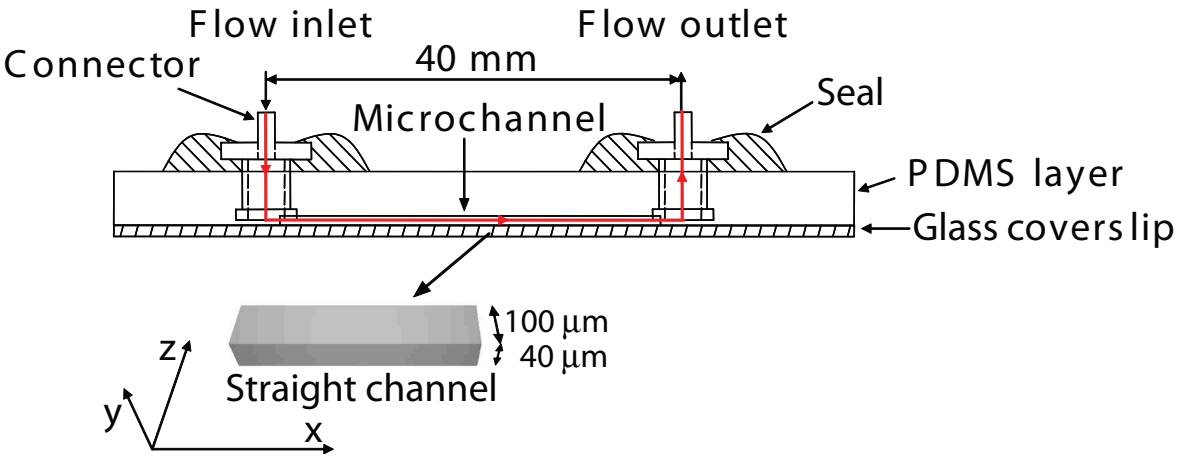

Figure 2.1: Illustration of a straight microchannel. Edited from Gao (2010).

2.3 Confocal microscopy

As a common tool for studying colloidal system, confocal laser scanning microscopy (CLSM) is powerful in that it reveals the local structural information *inside* the sample while scattering methods generally can only resolve global average under limited conditions and conventional optical video microscopy is not able to obtain data far away from the surface (Arora & Tata, 1998). CLSM has been used to study colloidal crystals (Morinaga *et al.*, 2008; Wu *et al.*, 2009), gels (Ohtsuka *et al.*, 2008), phase separation (Ito *et al.*, 1994), sedimentation (Royall *et al.*, 2005; Beckham & Bevan, 2007) and shear-induced migration (Frank *et al.*, 2003; Gao & Gilchrist, 2008; Gao *et al.*, 2009), etc.

A VT-Eye confocal microscope (VisiTech International) was used to probe the structure of suspension flow in microchannel. This high-speed microscope is able to scan as fast as 400 frames per second (fps) over a thin focal plane (0.5μm in thickness). A 100-times-magnification oil objective is controlled by a piezoelectric motor which enables it to move vertically up to 100 μm distance and scan every 0.1 μm. The scan rate can be as high as 100 fps for 512×512 pixel^2 images. In the experiments the channel (with the glass coverslip downward) was put on top of the objective so that microscope would scan through the suspension in the direction of velocity gradient.

The experimental framework is described by Fig. 2.2(a). Confocal scannings in our experiments were comprised of two parts: velocimetry measurement and stopped-flow measurement. In the former, the microscope scanned from the bottom toward top of the sample along the vertical or velocity-gradient direction, taking 10 images every 0.1 μm while the suspension is flowing. The velocity at each point could then be

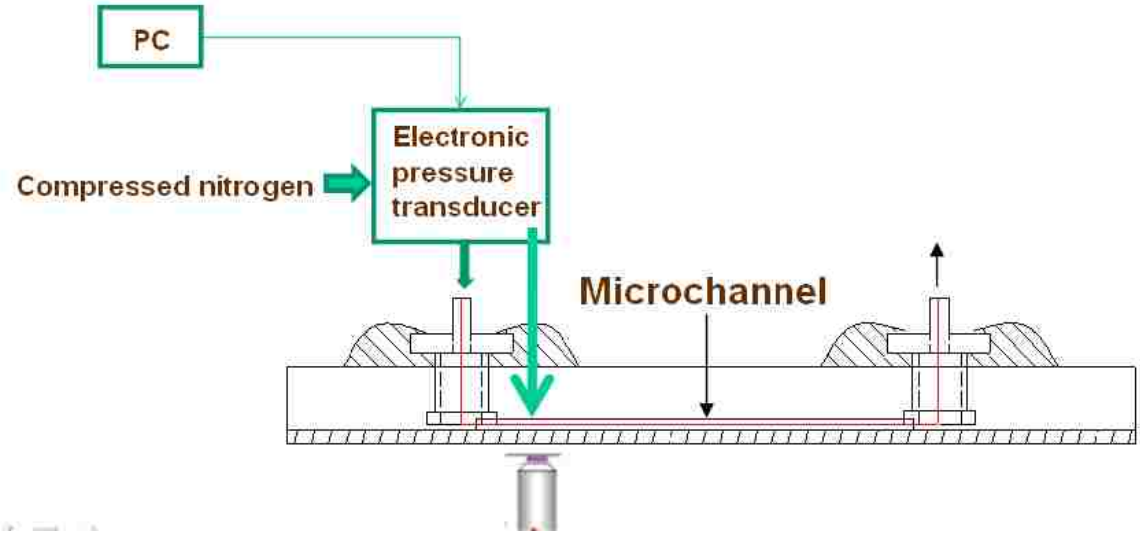

(a)

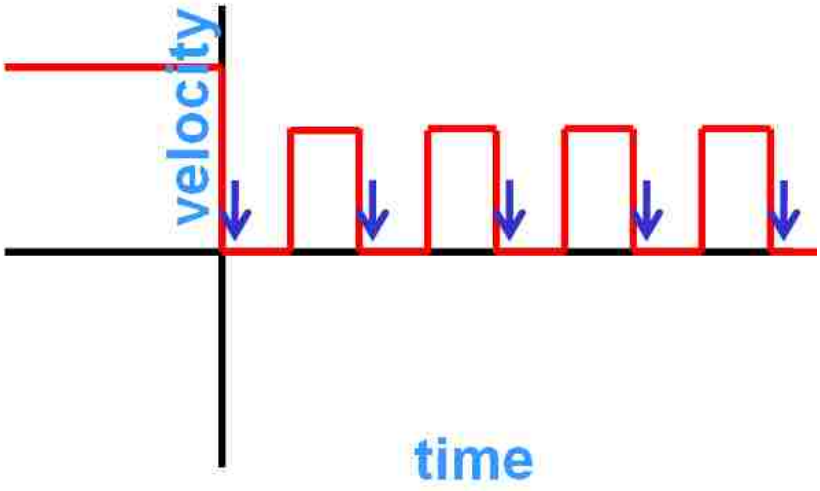

(b)

Figure 2.2: Experimental setup. (a): objective scanned at bottom of channel and flow was finely controlled by electronic devices; (b): multiple stopped-flow scans were performed immediately after flow cessation.

calculated by comparing displacements of the same particle between frames differed by certain time interval and averaging over at least ten particles. In the stopped-flow measurement, after the flow had reached steady state for some time, it was carefully stopped by reducing the nitrogen pressure, manipulated by the electropneumatic converter. Immediately after flow cessation(Fig. 2.2(b)), confocal scan through the system was started, same fashion as in velocimetry measurement except that now we took 1 image per 0.1 μm at 100 fps. After the scan, flow was restarted and the process was repeated for at least ten times for each system. The stopped-flow scans were processed in IDL. Particle-tracking routines developed by Dr. Eric Weeks at Emory University were used to reconstruct the three-dimensional particle distribution in the experiments. $g(\mathbf{r})$ was then calculated from these renderings, using improved IDL and Matlab routines initially developed by Dr. Changbao Gao.

Because in pressure-driven channel flow the shear rate varies along velocity-gradient direction, $g(\mathbf{r})$ has to be obtained locally. After determining the shear rate or Péclet number at a certain shear plane, only particles within one particle diameter distance from that plane were cropped for the calculation. On the other hand, it means we are able to acquire microstructure at different Pe's in one single experiment.

Chapter 3

Microstructure and rheology of sheared colloidal suspensions

3.1 Introduction

As is discussed in Chapter 1, when subject to flow, concentrated suspension of particles can demonstrate intricate and irregular behaviors such as shear-thinning/thickening, thixotropy/rheopexy, yield stress and normal stresses, etc (Stickel & Powell, 2005); and the key behind this complexity is the suspension's underlying microstructure, i.e. how particles arrange themselves with respect to each other under convection, thermal fluctuation and interparticle forces. Zarraga *et al.* (2000) calculated the stress of a dilute suspension of doublets based on the constitutive equation of Nir & Acrivos (1973), and showed the normal stress differences are functions of the orientation of the doublets. Gadala-Maria & Acrivos (1980) discovered the stress recaptures its original value when the suspension experiences shear-arrest and then

restart of shear in the same direction; but the stress will undergo some transients before reaching steady state if the shear restarts in the opposite direction. This finding is a strong indication that shear-induced anisotropic structure exists in suspensions and this microstructure determines rheology. Later experimental study on shear flow of suspensions were based on light scattering (Husband & Gadala-Maria, 1987; Parsi & Gadala-Maria, 1987) and laser sheet imaging (Rampall *et al.*, 1997), which obtained the pair distribution function and pointed out that anisotropy exists on flow-velocity gradient plane. Specifically there is higher correlation around the compressive axis and lower around the extensional.

Microstructure is also the main theme of shear-thickening mechanism of suspensions. Hoffman (1972) carried out one of the earliest experimental study on the coupling between rheology and microstructure of suspensions: by means of white light diffraction, it was observed an order-disorder transition in particle arrays parallel to shear plane, associated with a viscosity discontinuity, or an abrupt shear-thickening. Hoffman's theory is supported by the experiments of Gondret & Petit (1996) in their rheo-optical measurement that disordered structures always produce larger viscosity than ordered ones. However, an alternative mechanism (Brady & Bossis, 1985; Bossis & Brady, 1989) seems more promising, which states that thickening is the result of formation of dynamic hydroclusters under shear. Small-angle neutron scattering experiments (Bender & Wagner, 1995, 1996) confirmed this theory. Very recently observation from confocal microscopy (Cheng *et al.*, 2011) also reinforced its validity. However the experimental design of Cheng *et al.* (2011) might be problematic, because their flow cell is too narrow to rule out wall effects.

Therefore the microstructural information is crucial in explaining suspension rheology and has been the focus of extensive studies. In spite of the limited number of experimental studies and their relatively low quality, up to date, the most fruitful and informative results on suspension microstructure have been realized from numerical simulations. Stokesian Dynamics (Brady & Bossis, 1988) and accelerated Stokesian Dynamics (Sierou & Brady, 2001) are the most extensively used methods. For instance, SD/ASD have been applied to obtain microstructural data in order to investigate rheology of Brownian suspension at different Pe's (Foss & Brady, 2000; Morris & Katyal, 2002), velocity fluctuation in sheared suspensions (Drazer *et al.*, 2004), phase/order transition (Kulkarni & Morris, 2009), shear-thickening (Melrose & Ball, 2004*b*,*a*) and cluster formation (Yurkovetsky & Morris, 2006). Pan *et al.* (2010) adopted Dissipative Particle Dynamics (DPD) to simulate suspension flow and obtained similar outcome as SD. These computational results are mostly finely plotted and reveal details of the microstructure such as shape of the near-contact boundary layer. While computational methods and new theoretical frameworks are quickly evolving, experiments are likely to catch up because of recent application of various optical methods to obtain microstructural data.

The paucity and coarseness of experimental outcomes have been due to practical difficulties and applicability of the methods, e.g. opacity of the sample which obstructs light scattering and critical requirements on solvents for neutron and X-ray scattering approaches (Mewis & Wagner, 2009). Gao *et al.* (2010); Gao (2010) devised a novel approach, in which suspension flowing in a straight microchannel is stopped quickly and scanned by a confocal microscope. Gao and Gilchrist anticipate to obtain a "frozen" structure of suspension of silica microspheres under flow,

since when Brownian motion is weak, ideally there is no apparent driving force to alter the structure shortly after flow cessation. This method produces high-quality data with high throughput. It also explores in one single experiment the structure resulting from a range of shear rates or Pe's, given the nonlinear nature of channel flow. The pair distribution function obtained by Gao *et al.* (2010); Gao (2010) agrees reasonably well with computations; nevertheless, from Fig. 3.1 notable discrepancies also exist. This work aims to address the deviation and conduct a more complete microstructural study of nearly hard-sphere suspension.

Before presenting this work, some background on pair distribution function, the indicator for microstructure in our study, is given below.

The Smoluchowski equation (Eq.1.15) describes evolution of microstructure in terms of the N-particle configuration probability, $P_N(\mathbf{x}_1, \mathbf{x}_2 \cdots, \mathbf{x}_N)$.

Given the difficulty in solving Eq.1.15, a much more accessible way is to use the pair distribution function $g(\mathbf{r})$ (Batchelor & Green, 1972a), obtained by integrating P_N over $N-2$ particles. Another way to define it is:

$$g(\mathbf{r}) \equiv \frac{P_{1|1}(\mathbf{r})}{n} \tag{3.1}$$

where $P_{1|1}(\mathbf{r})$ is the conditional probability of finding a particle at position $\mathbf{r}$ with respect to a reference particle, and n is the particle number density.

In this system the maximum particle Reynolds number $Re_p = 3.2 \times 10^{-5}$, so inertia plays an insignificant role. The remaining key parameter affecting $g(\mathbf{r})$ is the Péclet number, $Pe = \frac{6\pi\eta\dot{\gamma}a^3}{kT}$, since Pe reflects the competition between hydrodynamic and Brownian forces from which the microstructure is dictated. Foss & Brady (2000) conducted systematic study on $g(\mathbf{r})$ at different Pe's for a hard-sphere suspension

and anisotropy is observed on velocity-velocity gradient plane when Pe is raised, as opposed to isotropic structure near equilibrium. This anisotropy shows accumulation of correlation around compressional axes and depletion around the extensional axes. It signals shear-thickening and normal stresses and is one strong evidence of the coupling between rheological properties and the underlying microstructure.

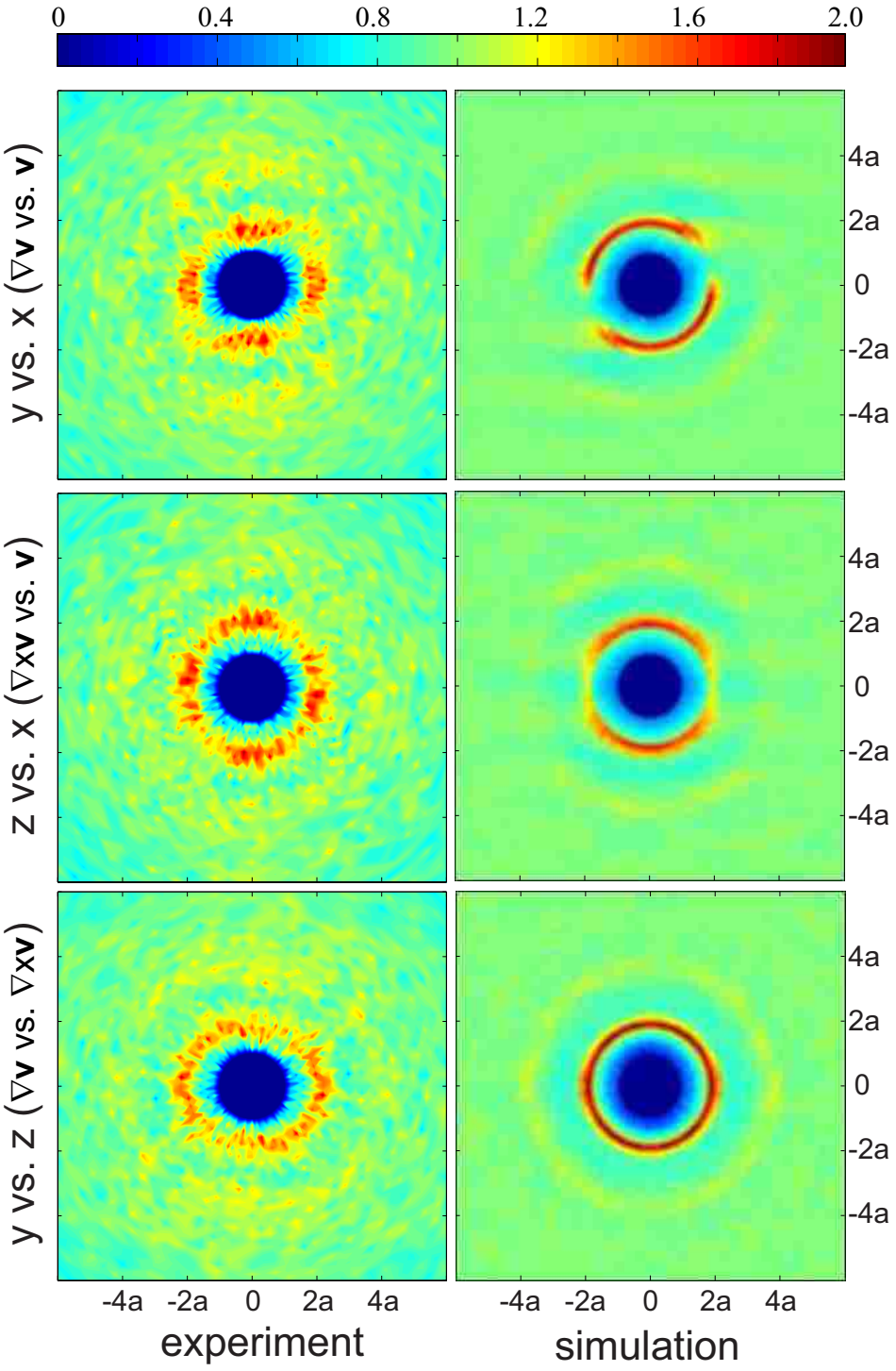

Figure 3.1: $g(\mathbf{r})$ plots on three orthogonal planes obtained experimentally (left column) and computationally (right column) by Gao *et al.* (2010) at Pe=1700 and ϕ=0.32.

3.2 Experimental

It is found that the discrepancy between experiment and simulation in Gao *et al.* (2010) is most likely induced by the fluorescent dye (rhodamine B) dissolved in the suspending fluid, for imaging purpose. Rhodamine B is acidic, pK_{a1}=1.42 (Ramette & Sandell, 1956), which disfavors the stability of silica colloidal suspension (Russel *et al.*, 1989). This effect may not be ignored at the experimental Rhodamine B concentration, 0.1 mM, while pH is only 8 and salt concentration 0.025 mM (Gao *et al.*, 2009).

In order to obtain more accurate results, it is necessary to keep the suspension from impurities such as rhodamine B, but in the meantime retain the fluorescence of the particles. The two-stage Stöber synthesis is one solution: synthesized particles all have a fluorescent core which is enclosed by a pure silica shell to prevent any chemical influences. Fig. 3.2 demonstrates an image of the final product under scanning electron microscope (SEM). The diameter is 880±80 nm, less than 10% variation.

Particle suspensions are prepared in the way described in Section 2.1. The overall volume fraction is controlled to be approximately 0.4. After long-time sonification, suspension is injected into the connector at channel inlet. The channel is then put onto the platform of confocal microscope, the objective sitting below the cover slip (channel bottom) a few millimeters downstream from the inlet. Compressed nitrogen is then connected to the inlet to drive suspension flow. Instead of a three-way valve used by Gao *et al.* (2010), the pressure of nitrogen is finely tuned by an electropneumatic converter (Omega Engineering) which receives analog signals from a computer.

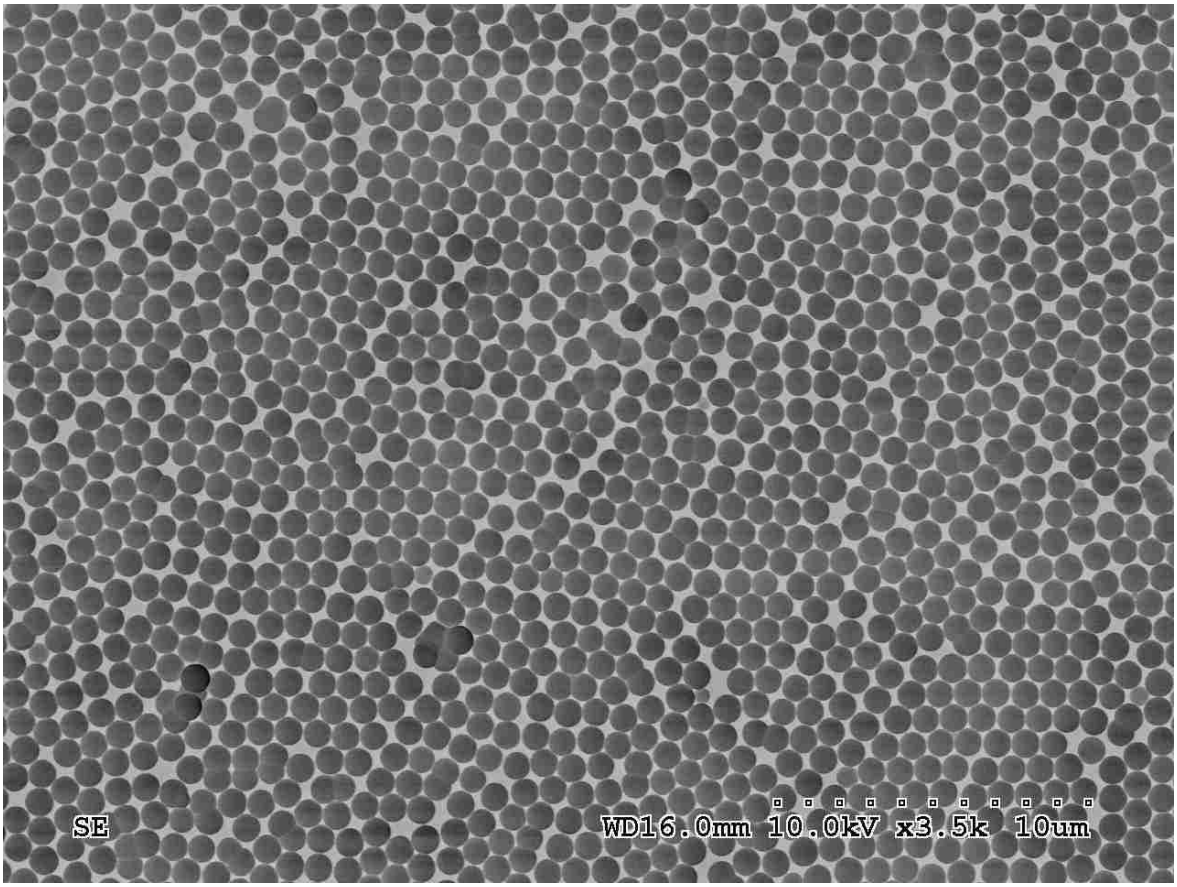

Figure 3.2: SEM image of synthesized silica particles, taken by Alex Weldon.

One can raise or drop the inlet pressure rapidly by scrolling a button on the computer screen, therefore easily manipulating the flow rate. This improvement reduces disturbances and enables flow cessation within a few seconds with minimal backflow.

Suspension was flowed for a few minutes, a time scale longer than the average residence time of particles in the channel, and then quickly stopped and scanned by the confocal microscope. This cycle is repeated for at least ten times for each sample. The scans were processed in IDL and $g(\mathbf{r})$ calculated for specific Pe and ϕ.

3.3 Results and discussion

3.3.1 Pair correlation

A suspension with $\kappa^{-1} = 8$nm and pH = 8.0 was examined. Given the small Debye length relative to particle size, this highly screened system can be regarded as suspension of hard spheres with negligible interparticle forces and has been studied through simulations (Foss & Brady, 2000; Gao *et al.*, 2010) and experiment (Gao *et al.*, 2010). The experiment in this study is a refinement of the one by Gao et al.

First the velocity and shear rate profiles across the lower half of the channel are presented in Fig. 3.3. The distance is zero at the first layer of particles next to channel bottom and normalized by particle diameter. Velocity profile is obtained by tracking movement of 10 particles at each distance within given time interval. Due to fluctuations and system errors, the flow curve is not perfectly smooth. But the data are sufficient for us to obtain local shear rate and Péclet number with good accuracy. Although it may appears familiar in shape, a parabolic curve is not used to fit the velocity data, for it is indicated by previous research (Lyon & Leal, 1998) that velocity profile of concentrated suspension in a channel flow can deviate from the common parabolic shape.

For each specific Péclet number, we calculate the local $g(\mathbf{r})$, which is plotted on three orthogonal planes formed by three axes along directions of flow (x), velocity gradient (y) and vorticity (z). We ignore the near-wall particles (distance < 4) in order to exclude hydrodynamic effects caused by the channel bottom. In Fig. 3.4, the left column arrays $g(\mathbf{r})$ plots obtained experimentally on x-y, x-z and z-y planes at Pe=1.1×10^3 and ϕ=0.30; and the right column plots obtained computationally by

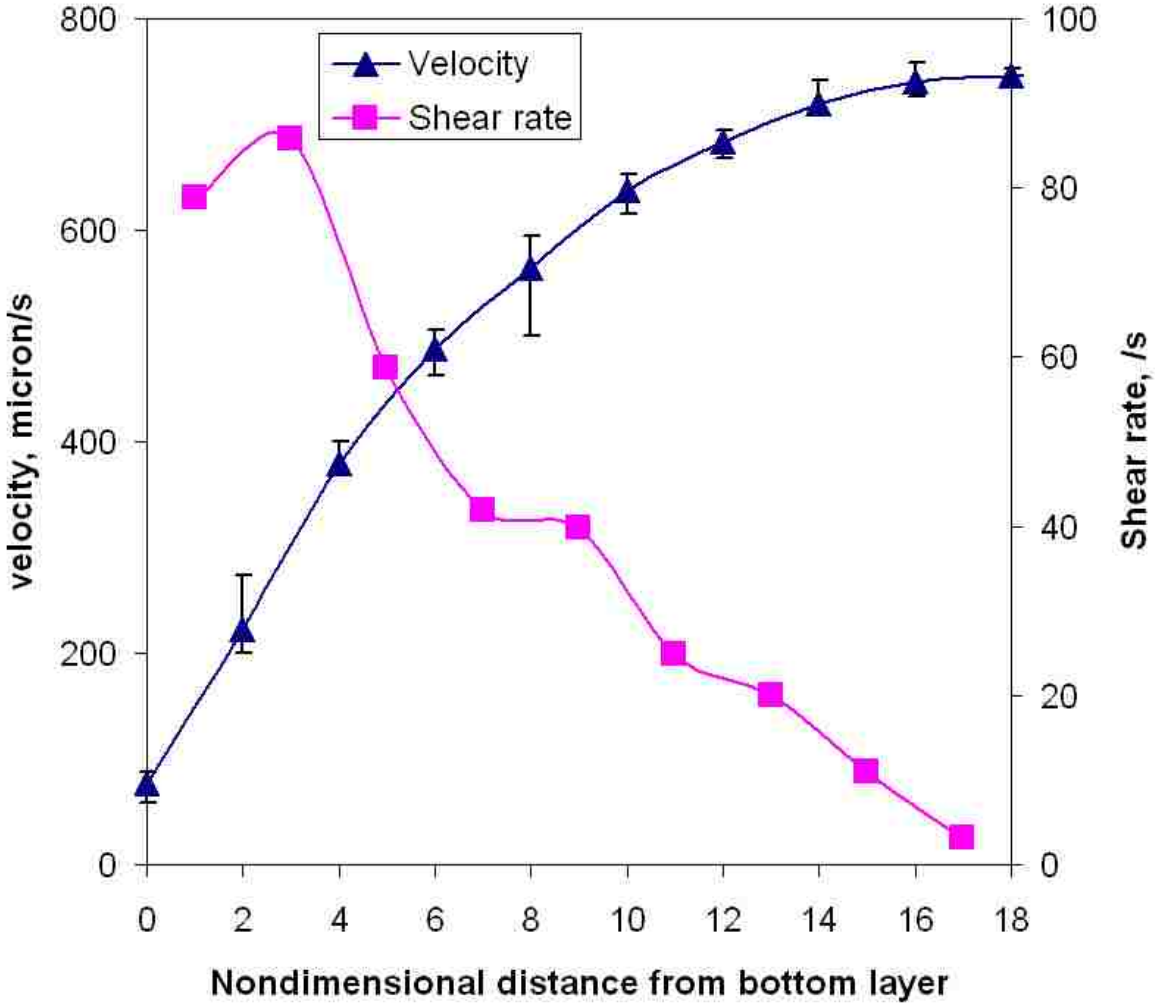

Figure 3.3: Measured velocity and estimation of shear rate from bottom layer toward the center of a suspension of hard spheres.

Accelerated Stokesian Dynamics (Gao *et al.*, 2010) at Pe=1700 ϕ=0.32. It should be noted that the boundary is smooth and particles experience slip near the boundary. The spatial coordinates are normalized by particle diameter and color indicates magnitude of $g(\mathbf{r})$. However, for better contrast, an upper cut-off value at $g(\mathbf{r})$=2 is imposed, which is denoted by the maximum redness (see color bar).

A quick comparison with Fig. 3.1 reveals that this new result holds more fidelity to theory and computation, e.g. Foss & Brady (2000). On x-y plane, not only the signature anisotropy is confirmed, but such details as vague tails near the opening of the innermost ring are also matched between the two different approaches; however the experiment suggests stronger correlation along flow direction with two red dots around 0° and 180° directions, while simulation shows a uniform high-probability incomplete ring. On x-z plane both results agree on a stronger correlation along z- than x-direction in the first ring, except a short string structure between the first and second rings along x-direction is seen in experiment, but absent from the simulation. A uniform first ring on z-y plane is achieved by both methods, although the experiment reveals some layering along y-direction. Multiple reasons may give rise to these disagreements, including mismatch of Pe and ϕ in the two separate studies, near-wall effect in experiment or simplifications made in the simulation regarding particle interactions.

Microstructure at different Pe's from one single experiment, are shown in Fig. 3.5. Since ϕ changes with shear rate as a result of shear-induced migration, effects of Pe and ϕ are always coupled in our system. From left to right, with Pe decreasing and ϕ increasing, structural ordering and symmetry is enhanced as a consequence of reduced hydrodynamic force as well as increase in volume fraction. The evidence is, on all

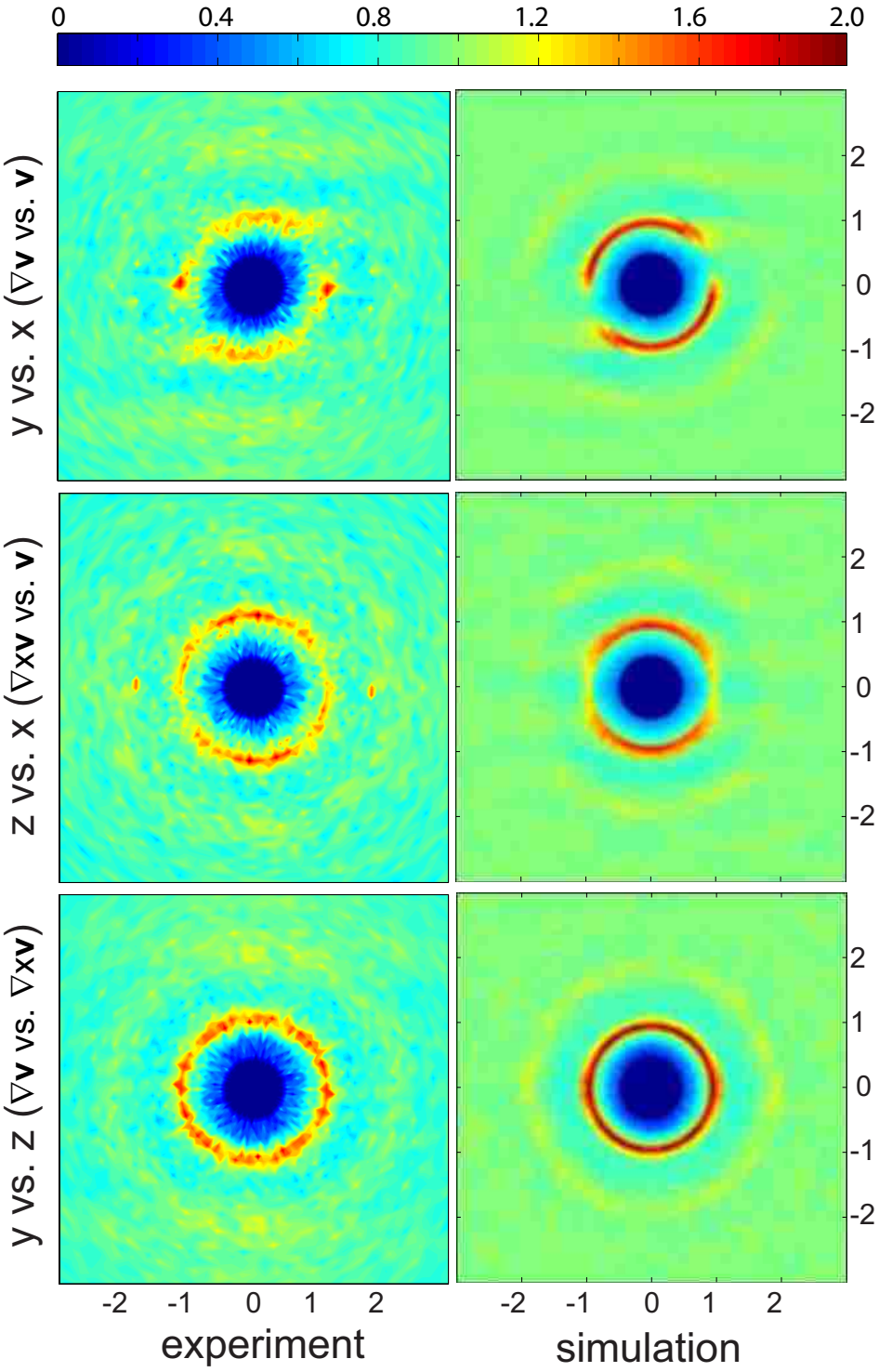

Figure 3.4: Comparison of experimental and computational $g(\mathbf{r})$ at high Pe and ϕ.

three planes, the inner and outer rings of high-probability are being enhanced from left to right; e.g. in the last two columns the third outer ring becomes identifiable, implying longer range of correlation. In meantime, although all x-y plots demonstrate the fingerprint anisotropy, it is gradually reduced. This is particularly clear on the x-y plane: the accumulation of probability near the compression axes in Fig. 3.5a) and b) starts to relax toward extensional axes in c) and d), and eventually joins to form a fairly uniform inner ring in e). Along the columns these plots also confirm that with decreasing Pe, the three projections are converging toward an equilibrated, isotropic structure.

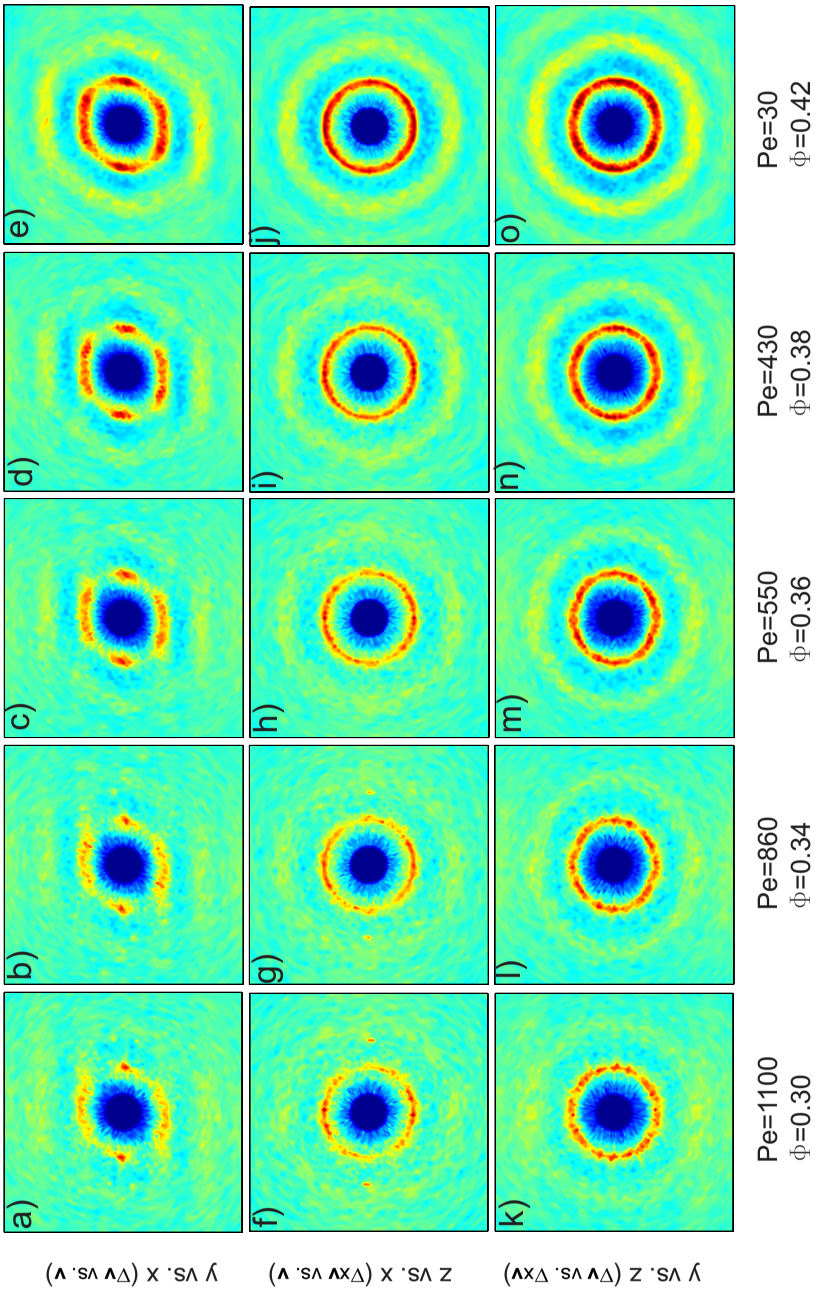

Figure 3.5: $g(\mathbf{r})$ as a function of Pe and ϕ.

3.3.2 Calculation of viscometric functions

Rheological measurements of suspensions have been conducted extensively in the last few decades. Krieger (1972) measured the shear viscosity of various systems and obtained coefficients for the Dougherty-Krieger relation (Krieger & Dougherty, 1959). The shear rates in his study are mostly in the shear-thinning regime. Chan & Powell (1984) found if ϕ <0.3 and the interstitial fluid is Newtonian, the suspension behaves mostly like a Newtonian fluid for shear rates up to 100 s^{-1}. de Kruif *et al.* (1985) and van der Werff & de Kruif (1989) measured shear rate and concentration dependence of viscosities at low- and high-shear limits also in the shear-thinning regime and discussed the effect of concentration on shear-thinning transition. D'Haene *et al.* (1993) performed systematic rheo-optic study of shear-thickening and suggested the hydrocluster theory is the proper mechanism.

are challenging and only relatively recently (Zarraga *et al.*, 2000) was able to obtain results consistent enough for comparison with computations (Phung *et al.*, 1996).. The first and second normal stress differences, N_1 and N_2 (defined in Eq.1.17) are both negative and $|N_2| > |N_1|$. Constitutive relations involving normal stress have been applied to model shear-induced migration (Morris & Boulay, 1999; Frank *et al.*, 2003; Miller & Morris, 2006) and viscous resuspension (Ramachandran & Leighton, 2007).

In this study we calculate shear viscosity and normal stress differences based on the $g(\mathbf{r})$ data shown in the last section. The assumption here is the leading contribution to rheology is from near-contact pair-wise interactions, i.e. lubrication and short-range Brownian forces. We follow the method elaborated in Foss & Brady (2000),

according to which the stress tensors can be approximated as

$$\mathbf{S}^H \approx \mathbf{S}^H_{b.l.} \approx -n^2 \int_{b.l.} \mathbf{r}\mathbf{F}^{shear} g(\mathbf{r}) d\mathbf{r} \tag{3.2}$$

$$\mathbf{S}^B \approx \mathbf{S}^B_{b.l.} \approx -n^2 kTa \int_{r=2a} \hat{\mathbf{r}}\hat{\mathbf{r}} g(\mathbf{r}) dS \tag{3.3}$$

Here $\mathbf{S}^H$ and $\mathbf{S}^B$ are hydrodynamic and Brownian contributions to the total stress tensor; *b.l.* stands for a boundary layer with thickness of $O(Pe^{-1})$ at particle-particle contact (Brady & Morris, 1997); a is particle radius, n the number density, $\hat{\mathbf{r}}$ the unit vector in $\mathbf{r}$ direction; and

$$\mathbf{F}^{shear} \approx -3\pi\eta'_\infty(\phi) a^2 \dot{\gamma} \hat{\mathbf{r}} (\hat{\mathbf{r}} \cdot \mathbf{E} \cdot \hat{\mathbf{r}}) \tag{3.4}$$

where $\eta'_\infty(\phi)$ is the high-frequency dynamic viscosity.

Fig. 3.6 shows the calculated relative viscosity (upper) and its Brownian component (lower) at different locations across the channel. The Brownian part is generally insignificant and decays as hydrodynamics is enhanced, which is qualitatively consistent with Foss & Brady (2000). Apparently it seems the system demonstrated a shear-thinning behavior, however, as mentioned earlier the volume fraction changes across the channel with opposite trend to Pe. The data need to be rescaled to take into account implicit factors.

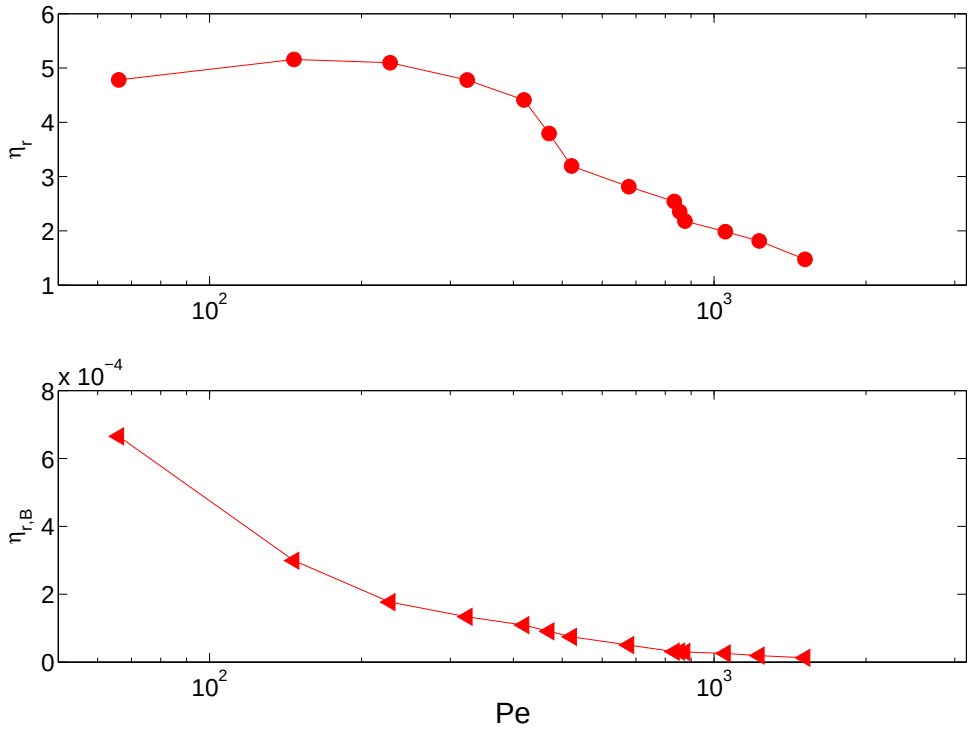

Figure 3.6: Relative viscosity (upper) and its Brownian component (lower) as a function of Pe.

We followed the scaling method of Foss & Brady (2000), where Pe is normalized by $\eta_\infty^{'}(\phi)/\eta$ and the newly scaled relative viscosity

$$\eta_{r,n} = (\frac{\eta_r}{\eta_\infty^{'}(\phi)} - 1)/\phi^2 g^0(2;\phi) \tag{3.5}$$

in which $g^0(2;\phi)$ is the equilibrium pair distribution function for hard spheres, given by Carnahan-Starling equation of state for ϕ <0.50 (Carnahan & Starling, 1969),

$$g^0(2;\phi) = \frac{1 - \frac{1}{2}\phi}{(1-\phi)^3} \tag{3.6}$$

The rescaled data are plotted in Figs. 3.7 and 3.8. From the plots, it can be seen that although both show a thinning-thickening trend, the scaling law of Foss & Brady (2000) does not collapse our data onto their master curve. Generally the Brownian contribution to the viscosity predicted by us is lower than Foss & Brady (2000) by two orders of magnitude, while our total or hydrodynamic viscosity is higher. Foss & Brady (2000) have compared relative viscosity from their simulation with experimental results by van der Werff & de Kruif (1989) and D'Haene *et al.* (1993), and underestimate of thickening by the simulation also occurs for high-shear-rate and high-concentration conditions. The reason is generally attributed to mismatch between reality and computation. Factors like interparticle forces in the real system and uncertainty in determining volume fraction may lead to this quantitative deviation (Foss & Brady, 2000). Normal stress differences across the channel are plotted

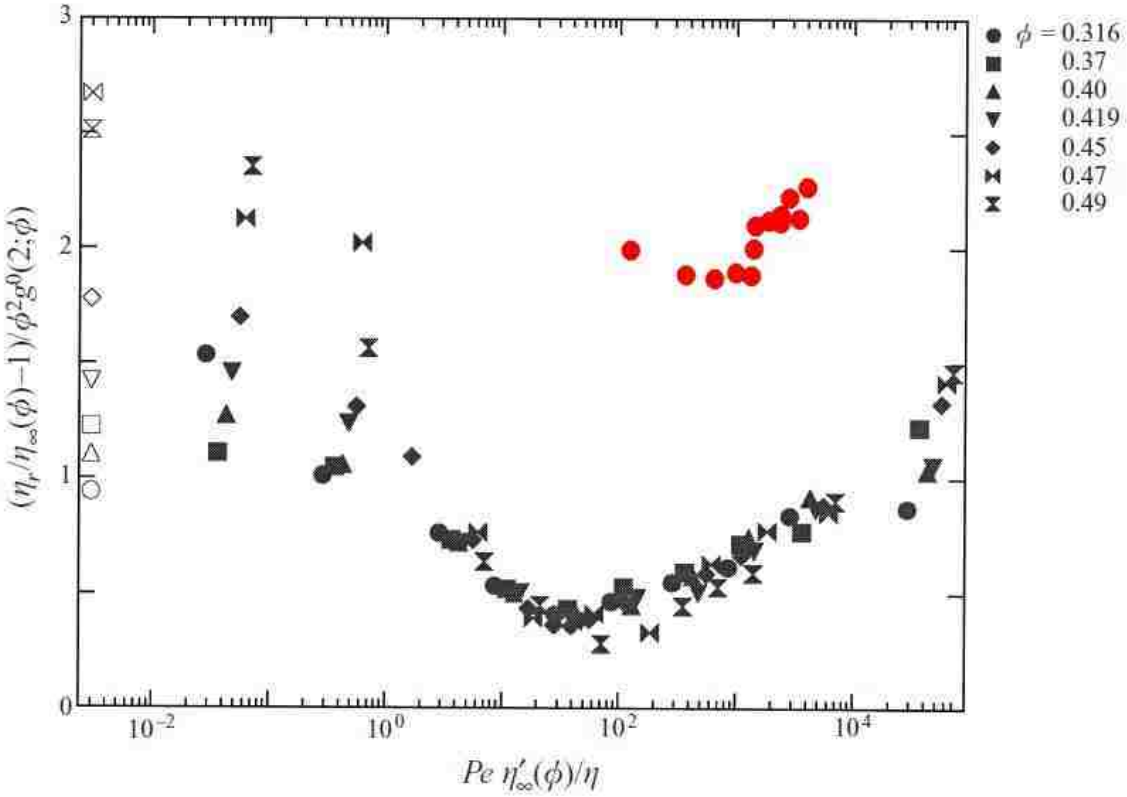

Figure 3.7: Relative viscosity vs Pe, rescaled. Black symbols: data from Foss & Brady (2000); red symbols: current work.

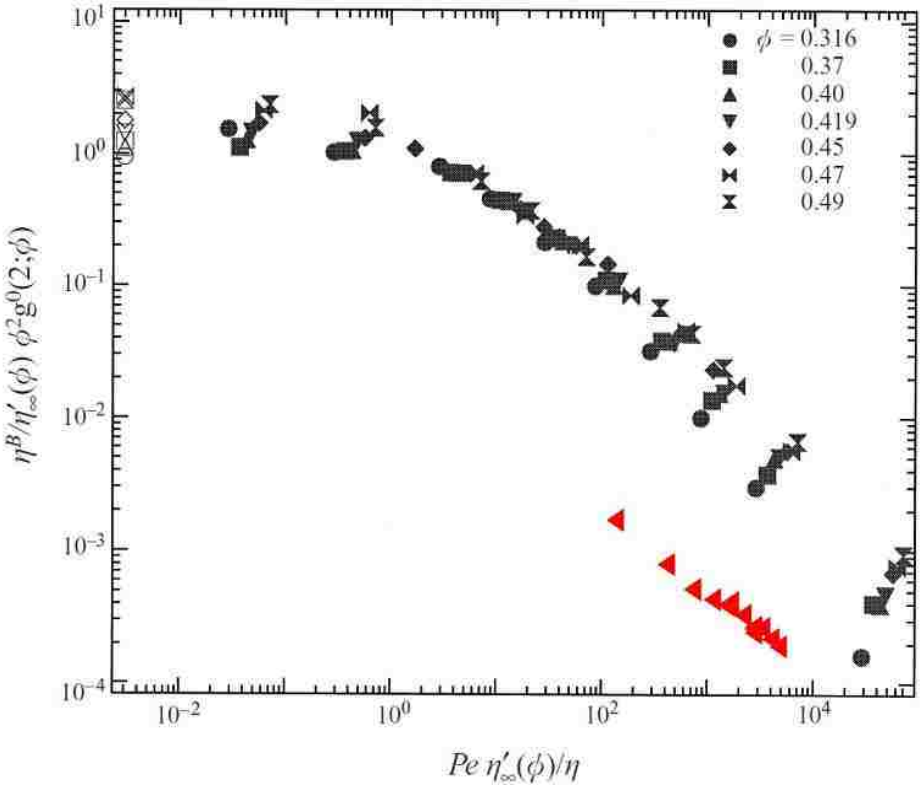

Figure 3.8: Brownian relative viscosity vs Pe, rescaled. Black symbols: data from Foss & Brady (2000); red symbols: current work.

in Fig. 3.9. The negative sign of N_1 and N_2 confirms previous results (Phung *et al.*, 1996; Zarraga *et al.*, 2000), which indicate the compressive nature of sheared suspensions. For the same reason mentioned above, the normal stress differences are again scaled by the factor $\eta_\infty^{'}\phi^2 g^0(2;\phi)$ (Foss & Brady, 2000).

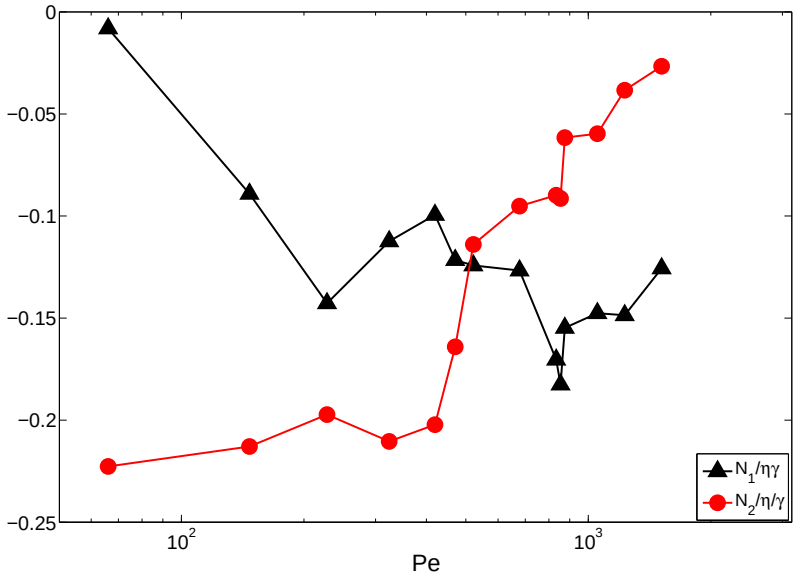

Figure 3.9: Variation of normal stress differences with Pe across the channel.

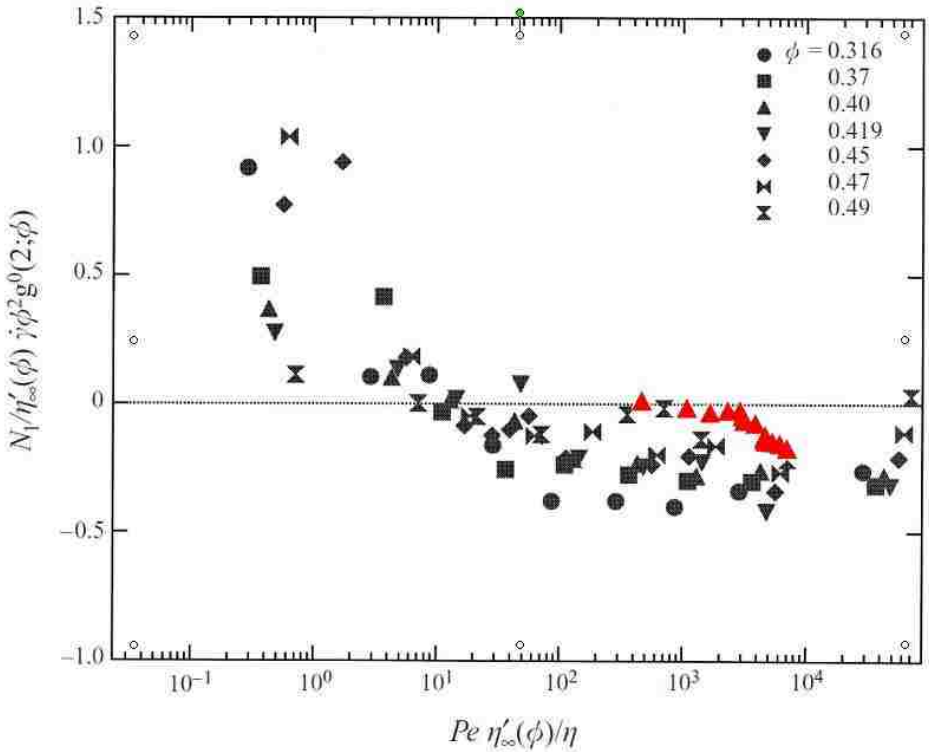

Figure 3.10: First normal stress difference N_1 vs Pe, rescaled. Black symbols: data from Foss & Brady (2000); red symbols: current work.

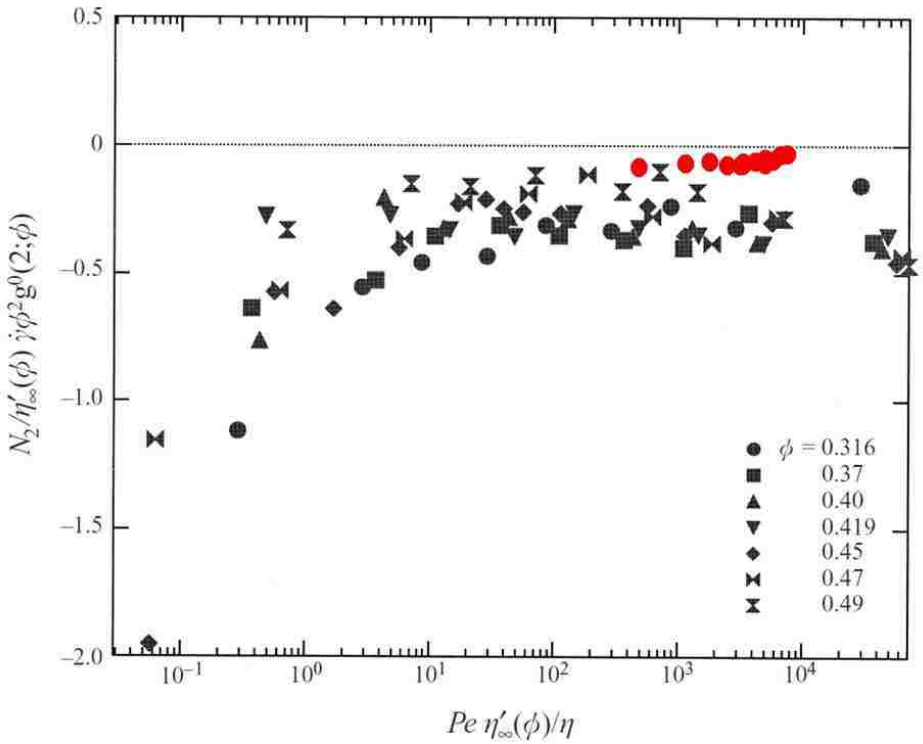

Figure 3.11: Second normal stress difference N_2 vs Pe, rescaled. Black symbols: data from Foss & Brady (2000); red symbols: current work.

It is obvious that even after rescaling, Foss & Brady (2000)'s data still show a fair amount of scattering. Besides the qualitative agreement between our and their data, it appears that our data demonstrate a smooth ascending trend of normalized $|N_1|$ and descending of normalized $|N_2|$ as the scaled Pe increases from 10^3 to 10^4 where there is a crossover of these two quantities. This feature is not clear in Foss and Brady's results. Zarraga *et al.* (2000) reported a maximum of the positive $N_1 - N_2$ as shear rate is increased. However, their experiment did not reach higher shear rates to reveal the possibility of a crossover.

It is also interesting to see the normal stress in vorticity direction Σ_{33} is catching up with Σ_{22} at high shear rates. People primarily recognize Σ_{22} as the predominant feature of sheared suspension, i.e. the "dilatancy" effect as well as shear-induced particle diffusion. Evolution of Σ_{33} and the corresponding diffusion coefficient may worthy of further investigation.

3.3.3 Hydrocluster analysis

The now widely accepted mechanism for shear-thickening is hydrocluster formation. When particles pass around each other in a shear flow, hydrodynamic force brings them close together to form dynamic clusters. Due to the lubrication and interactions between near-contact particles, clusters can greatly increase the system resistance against shear, which causes thickening. Brady & Bossis (1985) first observed this clustering in their numerical simulations of a monolayer of spheres. Bossis & Brady (1989) discussed the role of Brownian motion in destroying large clusters and proposed hydrocluster formation as the mechanism for shear-thickening at high shear rates. Results from Rheo-SANS measurements of suspensions of spherical (Bender & Wagner, 1996; Maranzano & Wagner, 2001, 2002) and prolate ellipsoidal particles (Egres *et al.*, 2006) agreed well with the hydrocluster model. Kalman & Wagner (2009) performed Rheo-USANS experiment on hard-sphere suspensions to probe the structure and confirmed hydroclusters are transient and precede the measured shear-thickening. Gopalakrishnan & Zukoski (2004) extended the hydrocluster model to suspension of attractive particles. Nevertheless, direct experimental investigation of hydroclusters did not appear until Cheng *et al.* (2011). Again, their experimental design fails to eliminate wall effects and particle tracking error due to shear-induced diffusion.

Clustering is readily quantified from our particle tracking data. With all particle locations available, any two particles of which the center-to-center distance is less than or equal to about one particle diameter are considered part of one hydrocluster. It is easy to identify all hydroclusters and their size in the suspension. Reasonable variation of the criterion for center-to-center distance affects the resulting number

and size of clusters, but the qualitative behavior is preserved, also observed by Bossis & Brady (1989).

Here we define the number of particles in each cluster as its length, L and total number of clusters as N. Then the average cluster length for a certain Pe and ϕ is obtained as $l = \frac{L}{N}$. Taking into account the concentration variation, it is reasonable to rescale l: $l_n = \frac{l}{\phi^l}$. We plot the normalized cluster size l_n vs Pe in Fig. 3.12. And it is clearly seen that the dynamics differentiate in low and high Pe cases. At low Pe, the average size of the hydroclusters decays slowly with shear rate. In the high Pe region(Pe >800), the hydrocluster size does not appear to asymptote to some constant value, but tends to grow indefinitely as is seen in Foss & Brady (2000), for all shear rates investigated here. But the growth rate slows down significantly as Pe keeps increasing. We assumed $l_n \sim ln(Pe)$ and fit the data with this relation in Fig. 3.13). In this rate, it is not clear whether hydroclusters will not develop to the container size as Pe approaches infinity.

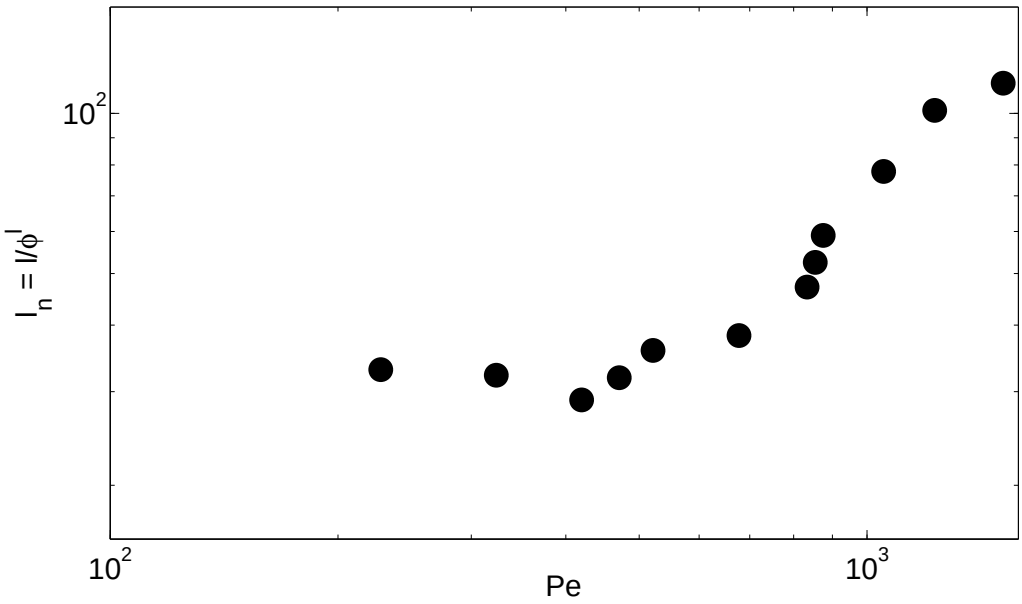

Figure 3.12: Normalized average cluster length as a function of Pe.

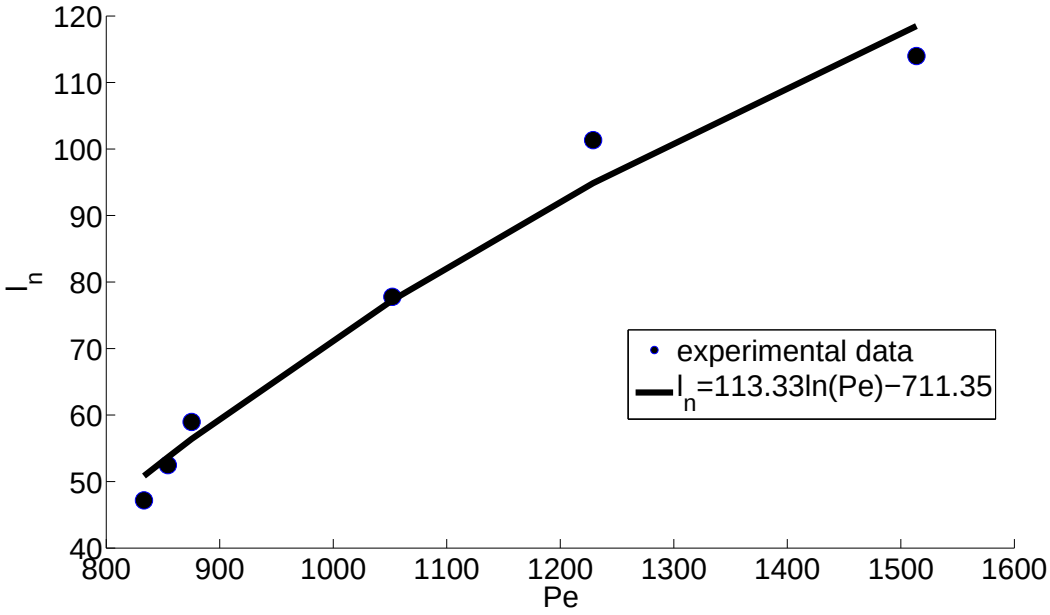

Figure 3.13: A linear growth of l_n with $ln(Pe)$ is fitted from experiments.

3.3.4 Shear-induced crystallization

It has been established that high shear rate can bring order into the system (Wu *et al.*, 2009). On the other hand, based on his experimental finding, Hoffman (1972) hypothesized that it is the breakdown of layered structures where particles form 2D hexagonal closed packing along the x-z plane, or an order-disorder transition that gives rise to shear-thickening. Although it has been shown that order-disorder transition is neither the sufficient nor the necessary condition for shear-thickening to happen (Maranzano & Wagner, 2002; Kalman & Wagner, 2009), this theory has received support from some evidences (Gondret & Petit, 1996; Hoffman, 1998). In order to judge over the controversy, it is of necessity to examine the validity of this hypothesis as well. The key parameter is the 2D local bond orientational order parameter Ψ_6 defined as (Wu *et al.*, 2009):

$$\Psi_6(r_{kj}) = \frac{1}{n_C} \sum_{j=1}^{n_C} e^{i6\theta(r_{kj})} \tag{3.7}$$

where n_C is the number of nearest neighbors around particle k and θ is the angle between the vector extending from center of particle k to center of particle j and an arbitrary axis. The closer Ψ_6 is to unity, the higher degree of crystallinity the system shows.

We calculated the order parameter Ψ_6 for different Pe's. Fig. 3.14 shows magnitude of Ψ_6 on x-z plane as well as the corresponding volume fraction ϕ. It is clearly seen that for Pe <1000, crystallinity follows well with the concentration curve, suggesting ordering mainly caused by solid exclusion. For Pe >1000, the mechanism is clearly shear-induced and strongly counteracts the descending trend of concentration.

For instance, at Pe=1500, concentration drops significantly, while $|\Psi_6|$ stays almost as high as in Pe=800.

It is therefore believed that ordered structures persist and are even enhanced by shear. In these experiments we have observed shear-thickening without order-disorder transition, a conclusion in agreement with other researchers such as Wagner (Bender & Wagner, 1995, 1996).

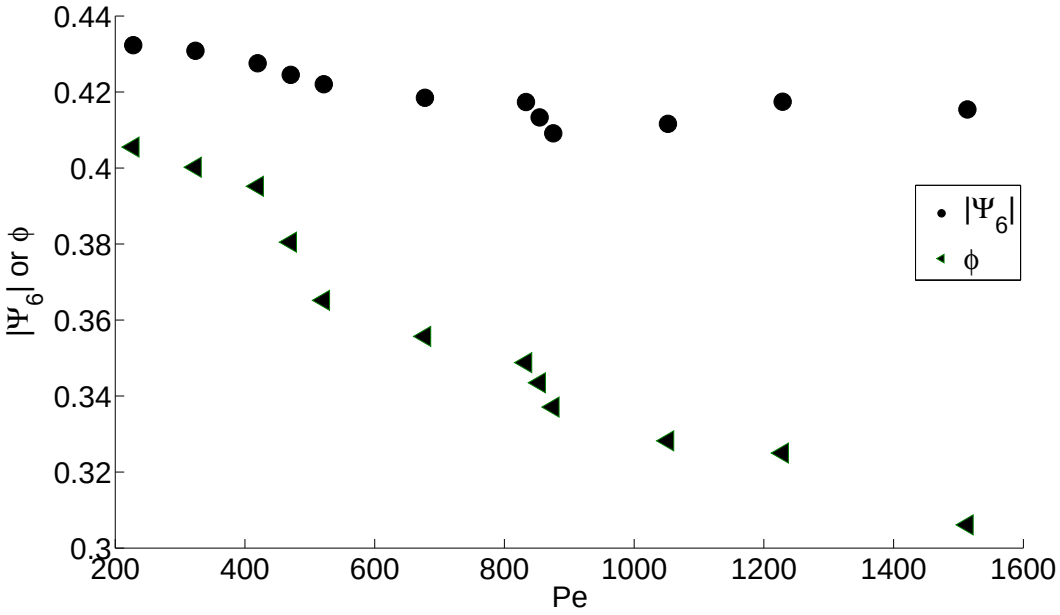

Figure 3.14: Order parameter $|\Psi_6|$ on x-z plane and volume fraction ϕ as functions of Pe.

3.3.5 Effect of electrostatics

The most common and effective way of tuning the electrostatic interactions in a colloidal system is to control its ionic strength. By reducing the [NaCl] in suspension, particles can have larger Debye length and the electrostatic interactions will be stronger. In this study particles with Debye lengths $\kappa^{-1} = 30$ and 80nm are examined along with the previous hard-sphere system of which $\kappa^{-1} = 8$nm.

As is shown in Fig. 3.15a) and b), when the Debye length κ^{-1} increases from 8 to 30nm, the first and second rings of nearest-neighbor on x-y plane is attenuated and dissipated; the same trend is observed on the other two planes as well, i.e. a decrease in the intensity of nearest-neighbor rings. This may suggest enhanced fluctuation induced by electrostatic interactions between particles, equivalent to Brownian motion (Stickel *et al.*, 2006). However when κ^{-1} keeps increasing up to 80 nm, the order is restored in that the ring intensity is raised. Particularly in Fig. 3.15c), the anisotropy along compressional axes is to some extend resisted in favor of a more symmetric structure. One may argue that it is because electrical repulsion has altered the original structure after flow is stopped, but first, κ^{-1} is still one order of magnitude less than particle diameter, which is the length scale for the $g(\mathbf{r})$ calculation; second, pair distribution is symmetric, that is when particles are pushing around each other, the net force on one particle is statistically zero. Therefore this more isotropic structure is very likely due to the long range ordering induced by strong electrostatic force. Plots on all three planes, when viewed from the left to right columns, indicate electrostatic force can reduce order by reinforcing fluctuation and promote order when it is strong enough to induce long-range correlations.

We also studied the microstructure variation across channel for the system with the strongest electrostatics. Fig. 3.16 shows $g(\mathbf{r})$ on all three planes (along the rows) at different Pe and ϕ's (Pe decreasing from left to right columns). Order is clearly enhanced on x-y and z-y planes as Pe goes down, evidenced by the more pronounced outer rings and raising intensity of all rings. Particularly on x-y plane the anisotropic first ring gradually closes up to form a more or less uniform circle, even when Pe is still on the order of hundreds. The high κ^{-1} clearly contributes to this ordering.

However, on the x-z plane, compared with Fig. 3.5f)-j), it seems in this system the shear-induced crystallization occurs at much lower Pe and decreasing Pe will diminish the ordered structures. It is hypothesized that long range correlation in this system makes particles more coordinative with each other under the influence of shear rate.

Large Debye length raises particle interactions, but on the other hand it also increases particle effective volume fraction. The trend observed in Figs. 3.15 and 3.16 generally conforms with one's expectation. However, it is also found the resulting microstructures based on individual data sets are not congruent with one another (remember all plots are averaged over at least ten sets). A more systematic study is needed to sort out possible hidden factors that affect structure and /or account for this discrepancy perhaps based on how interparticle forces may alter stability of solutions to the Smoluchowski equation.

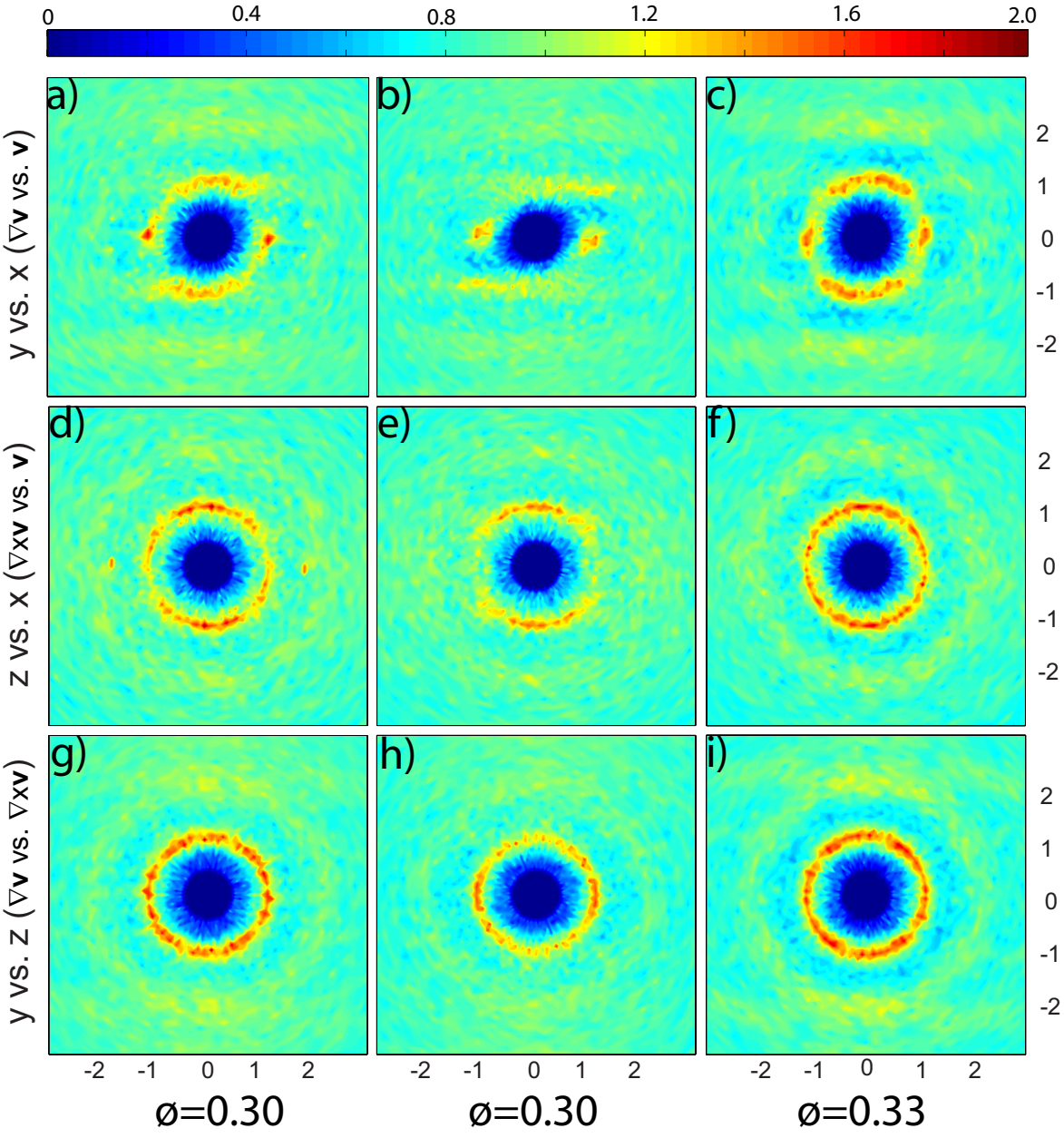

Figure 3.15: $g(\mathbf{r})$ as a function of κ^{-1}. Pe of all samples are greater than 1000.

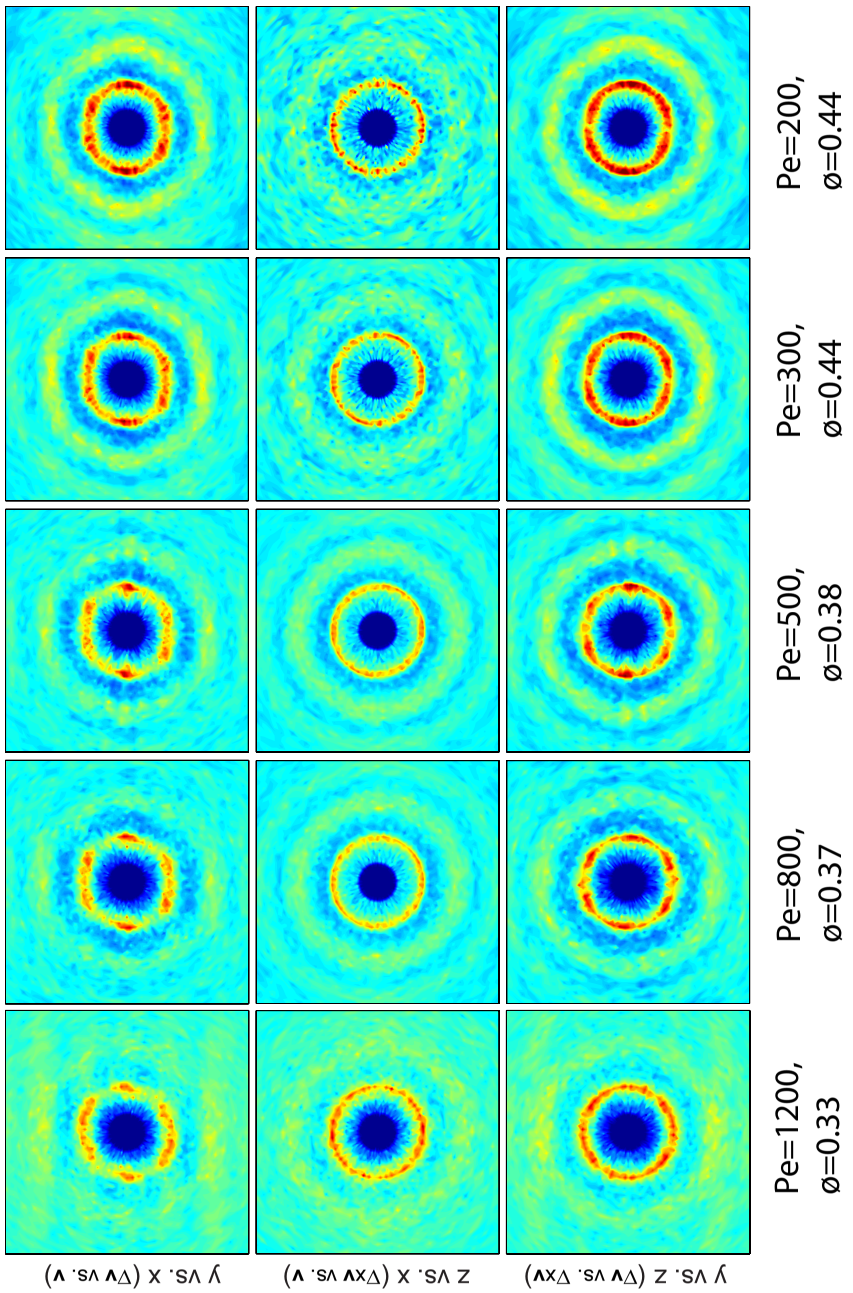

Figure 3.16: $g(\mathbf{r})$ as a function of Pe and ϕ when $\kappa^{-1} = 80$ nm.

3.4 Conclusions

We have improved an experimental method previously developed in our laboratory for direct measurement of microstructure in suspension flows. Our experiments typically operate under high Pe conditions, in which the anisotropy on x-y plane predicted by theory is clearly identified. Results obtained for a spectrum of Pe's in a near-hard-sphere system demonstrate interplay between hydrodynamics and concentration, the former in favor of anisotropy and the latter ordering and symmetry.

Calculated viscosity and normal stress differences agree qualitatively with the SD simulation by Foss & Brady (2000), e.g. shear-thickening at high Pe, and the trend for $|N_1|$ and $|N_2|$. However, quantitative mismatch may indicate a gap between computation and reality. Analyses on the cluster and crystalline structures under shear suggest the hydrocluster theory is proper for explaining shear-thickening. It is found the growth of normalized hydrocluster size scales with $ln(Pe)$ and crystallinity is particularly enhanced by shear for Pe >1000.

The effect of electrostatics on microstructure is also investigated. It is found that electrostatic force has a dubious role in ordering the particles: it enhances fluctuation, but eventually brings in long range ordering. Shear-induced crystallization is also affected by this force in that it is noticeable under lower Pe than hard-sphere system.

Chapter 4

Shear-induced migration and segregation in one-dimensional shear flow

4.1 Introduction

The preceding chapters elaborate the rheological behaviors of suspension flow and their roots. Based on such understanding, we will be looking at one fingerprint phenomenon, the shear-induced particle diffusion and migration, and its impact on practical processes. Shear-induced diffusion is caused by the hydrodynamic interactions when the suspension is in motion and differs from the Brownian diffusion in the sense that the particles are pushed to cross streamlines by constituents independent of temperature. These interactions depend on local deformation and scale nonlinearly in volume fraction. In a simple shear flow with uniform concentration, this mechanism leads particles to undergo a random walk with zero net flux (Eckstein

et al., 1977; Leighton & Acrivos, 1987*a*), which is termed shear-induced self-diffusion. However, when the shear or concentration distributions have gradients, this process results in non-zero mean and incur a flux in the flow, coined shear-induced migration (Gadala-Maria & Acrivos, 1980; Leighton & Acrivos, 1987*b*). As is evidenced in Fig. 4.1, shear-induced migration greatly influences the configuration of the system through the coupling of rheology and volume fraction. Shear-induced migration can be regarded either as a relaxation for the normal stress or a diffusion process. Gadala-Maria & Acrivos (1980) reported a long-time viscosity decay in a Couette viscometer, which is one of the earliest instances of shear-induced migration. Leighton & Acrivos (1987*b*) confirmed this finding through further experiments and attributed the decrease in viscosity to migration of particles from the shearing gap into the stationary outermost reservoir. Since it has been shown that the interaction between two spheres in Stokes flow is reversible (Batchelor & Green, 1972*b*), it is hypothesized that this migration arises from the irreversible interactions between particles as a result of surface roughness, multibody hydrodynamic interactions, plastic and elastic particle deformation, and even cavitation (Pine *et al.*, 2005). In all of these accounts, interactions lead to anisotropy in the suspension microstructure. Early models accounting for migration describe shear-induced migration in an analogy to the diffusion process with the coefficient obtained through a scaling argument (Leighton & Acrivos, 1987*b*). Phillips *et al.* (1992) divided the migration into one flux caused by gradients in collision frequency of particles and another by viscosity gradients.

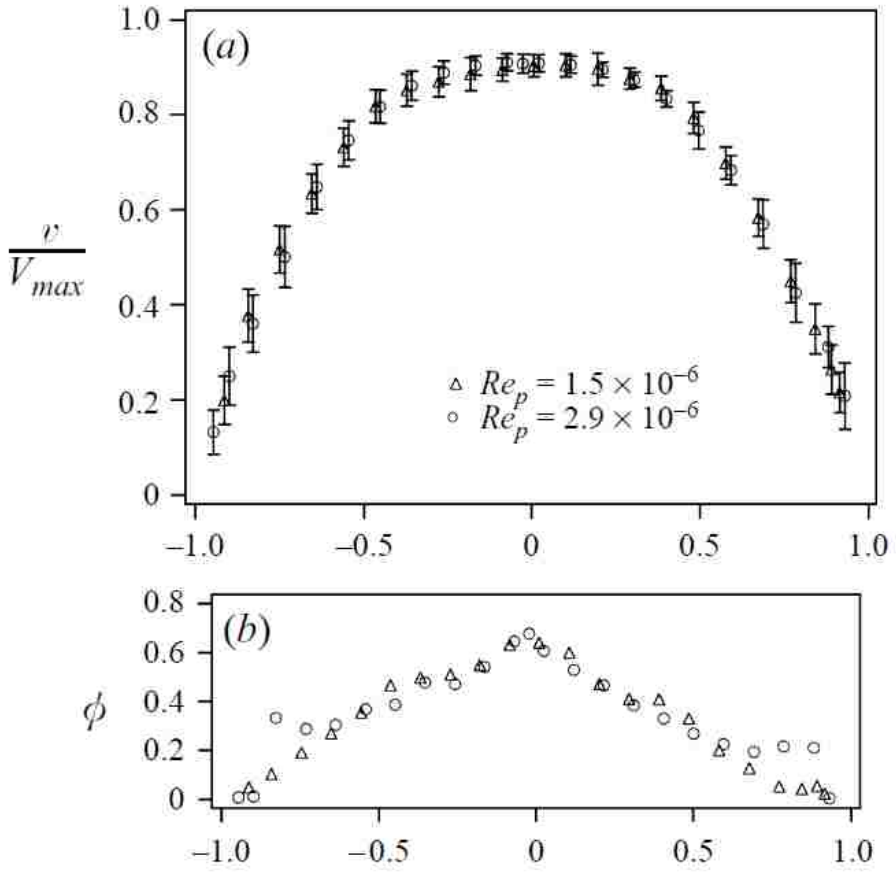

Figure 4.1: Shear-induced migration in a plane Poiseuille flow. (a) The velocity profile is blunted by higher concentrations in the low shear rate region near the center; (b) the corresponding concentration profile (Lyon & Leal, 1998).

Although the diffusive flux models manage to fit experimental data and are therefore widely adopted, they fail to account for the absence of migration, e.g. in parallel-plate torsional flow (Chow *et al.*, 1994). Krishnan *et al.* (1996) proposed a "curvature-induced migration" mechanism which adds an additional flux term to the conventional diffusive flux model to address the difficulty in curved flows. Merhi *et al.* (2005) determined the ratios between the coefficients for each flux by fitting simulation results to data from their experiments and those by Phillips *et al.* (1992).

Suspension stress models establish constitutive relations of shear-induced particle-phase stress and resort to stress balance for the particle migration. Nott & Brady (1994) built such a relation based on the suspension temperature, a quantity defined to measure the particle fluctuational velocity. However in their model the normal stress is isotropic. Morris & Boulay (1999) proposed a "normal stress viscosity", η_n, which connects particle pressure to shear rate; the particle phase stress tensor is

$$\Sigma_p = -\eta_n \dot{\gamma} \hat{\mathbf{Q}} + \eta_s \mathbf{E} \tag{4.1}$$

where η_s is the shear viscosity of the suspension, $\mathbf{E}$ the rate of strain tensor, $\dot{\gamma} = (\mathbf{E} : \mathbf{E})^{\frac{1}{2}}$ is the shear rate and $\hat{\mathbf{Q}} = diag(1, \lambda_2, \lambda_3)$ is a constant tensor representing the anisotropy in flow. The migration flux is shown to be a consequence of normal stress balance. But as most diffusive flux models, this one will suffer a singularity at zero shear rate; i.e. wherever local shear rate is zero, the normal stress will be zero and will not balance until maximum packing of particle is reached. To overcome this difficulty, the authors came up with a correction term of "non-local shear rate", $\dot{\gamma}_{NL}$, which makes the shear rate globally nonzero.

Fang *et al.* (2002) proposed an anisotropic suspension model based on the "flow-aligned tensor", defined in a very similar way to the $\hat{\mathbf{Q}}$ in Morris and Boulay's. Instead of non-local shear, the suspension temperature (Nott & Brady, 1994) was adopted in their model to eliminate the singularity at zero shear rate.

Zarraga *et al.* (2000) found the normal stress components of sheared concentrated suspensions, Σ_{ii}, scale with the magnitude of shear stress τ. They determined through various measurements and previous data the coefficients for each component,

$$\Sigma_{11} = -1.15\alpha\tau, \Sigma_{22} = -\alpha\tau, \Sigma_{33} = -0.46\alpha\tau \tag{4.2}$$

where α is a constant and the subscripts "1", "2" and "3" denote the direction of flow, velocity gradient and vorticity, respectively.

In connection with these efforts to define constitutive relationships that properly describe shear migration, many particle-level simulations such as Stokesian Dynamics simulations (Brady & Bossis, 1988) have been used to empirically scale these phenomena and probe the underlying structure that generates the normal stresses in these flows. Extensive results from Stokesian Dynamics calculation demonstrate anisotropy of microstructure and irreversibility as a consequence of either Brownian motion (Phung *et al.*, 1996; Brady & Morris, 1997; Morris & Katyal, 2002) or surface roughness (Brady & Morris, 1997; Sierou & Brady, 2002; Drazer *et al.*, 2004). Experimental evidences also support the anisotropic structure in sheared suspensions (Rampall *et al.*, 1997; Gao *et al.*, 2010). Generally, the structure of suspension under deformation indicates a greater number of nearest-neighbor interactions along the compression direction of the flow than the extensional axis, which consequently causes the irreversible migration.

Besides its mechanism and flow-related properties, shear-induced migration can be viewed as a segregation or demixing process and its ability to generate inhomogeneity may have huge impacts on real life activities. This chapter aims to address shear-induced demixing in 1D pressure-driven flow where no active mixing is applied, while the next chapter will study the interplay between demixing and chaotic mixing.

4.2 Results

In modeling shear migration, it is often preferable to employ a normal stress balance model, however current models have a significant limitation due to a singularity that occurs at points in flow that have zero shear rate. This limits prediction in the simplest of flows. For instance, in pressure-driven flows maximum concentration that results in infinite viscosity is predicted at the center regardless of the suspension bulk volume fraction. We have probed the validity of suspension models by scaling a previously proposed correction factor, a 'nonlocal shear rate' that aims to average suspension properties over many particle diameters (Morris & Boulay, 1999), to experimental measurements (Gao *et al.*, 2009). In this study, we also aim to predict at what concentration is shear migration strongest.

In our experiments, the channel has a width of 100μm and height of 40μm. A coordinate is set up such that the origin is located at the center of the entrance cross section; x axis points to the flow direction and y and z axes along width and height, respectively(see Fig. 4.2). We only analyze the downstream data from the center of the straight channels (around y=0) investigating the shear in the z-direction, which is much stronger than the shear in the y-direction. The migration at the center of the channel is strongly dependent on the shear in z-direction, while the concentration gradient in y-direction near the center is low. Thus, only data within $-20\mu\text{m} \leq y \leq 20\mu\text{m}$ are averaged to give a 1D concentration profile. In a fully developed pressure-driven 1D suspension flow at steady state, the normal stress in

the particulate phase must balance:

$$\nabla \cdot \Sigma_P^{NS} = \frac{\partial \Sigma_{P,zz}^{NS}}{\partial z} = 0 \tag{4.3}$$

where Σ_P^{NS} is the normal stress tensor in particulate phase, and z is the direction of velocity gradient.

It should also be noted that when considering the data near $y = 0$, the apparent bulk volume fraction, ϕ_{bulk}^a in this region is significantly higher due to particle migration toward the center. A set of experiments were carried out in the straight channels: $\phi_{bulk} = 0.21$, 0.22, 0.24, 0.275, 0.3, 0.33 and 0.35, with their corresponding $\phi_{bulk}^a = 0.25$, 0.27, 0.29, 0.34, 0.37, 0.39 and 0.41.

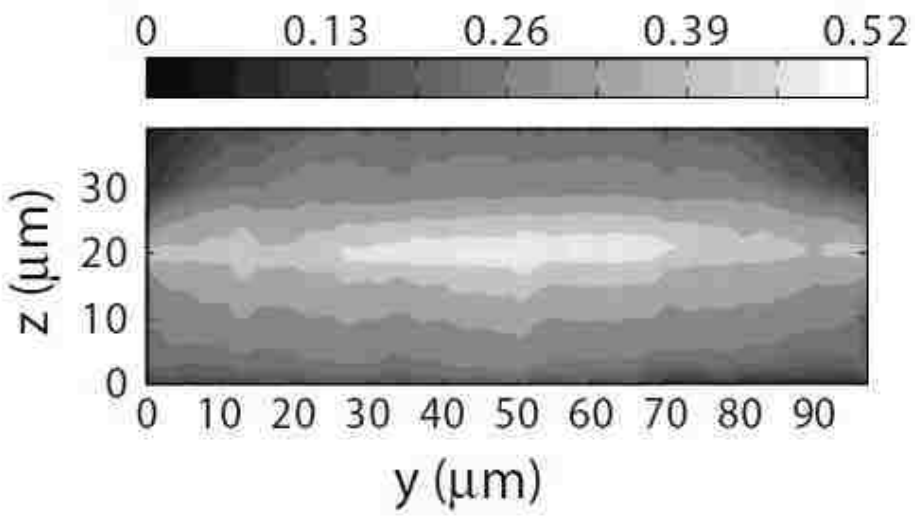

Figure 4.2: Concentration distribution on channel cross section, ϕ_{bulk}=0.30 (Gao *et al.*, 2009).

Particle phase normal stress can be expressed as Morris & Boulay (1999)

$$\Sigma_P^{NS} = -\eta_n(\dot{\gamma} + \dot{\gamma}_{NL})\mathbf{Q} \tag{4.4}$$

where

$$\eta_n = \frac{0.75\eta_0(\phi/\phi_m)^2}{(1-\phi/\phi_m)^2} \tag{4.5}$$

is the estimation of the normal stress viscosity (Morris & Boulay, 1999), $\dot{\gamma}$ is the local shear rate and $\mathbf{Q}$ is a constant tensor describing the anisotropy of the flow. $\dot{\gamma}_{NL}$ is the nonlocal shear rate. Without $\dot{\gamma}_{NL}$, this model predicts a physically unrealistic sharp peak in concentration at the center as a result of zero local shear rate, $\dot{\gamma} = 0$. The incorporation of $\dot{\gamma}_{NL}$ accounts for effects of finite particle size, Brownian motion and higher order interactions that occur for moderate to high ϕ's. In the previous work, the authors assume that $\dot{\gamma}_{NL}$ is primarily a function of particle size (Miller & Morris, 2006). The analysis presented here assumes that $\dot{\gamma}_{NL}$ is a function of ϕ_c, the local volume fraction at $y = 0$, which is also the maximum volume fraction measured in each profile. All concentrations are averaged over one particle diameter to represent the effective averaging resulting from the experimental measurement. To simplify the analysis, the non-local shear rate is assumed to be constant across the channel and used as a fitting parameter for the experimental data.

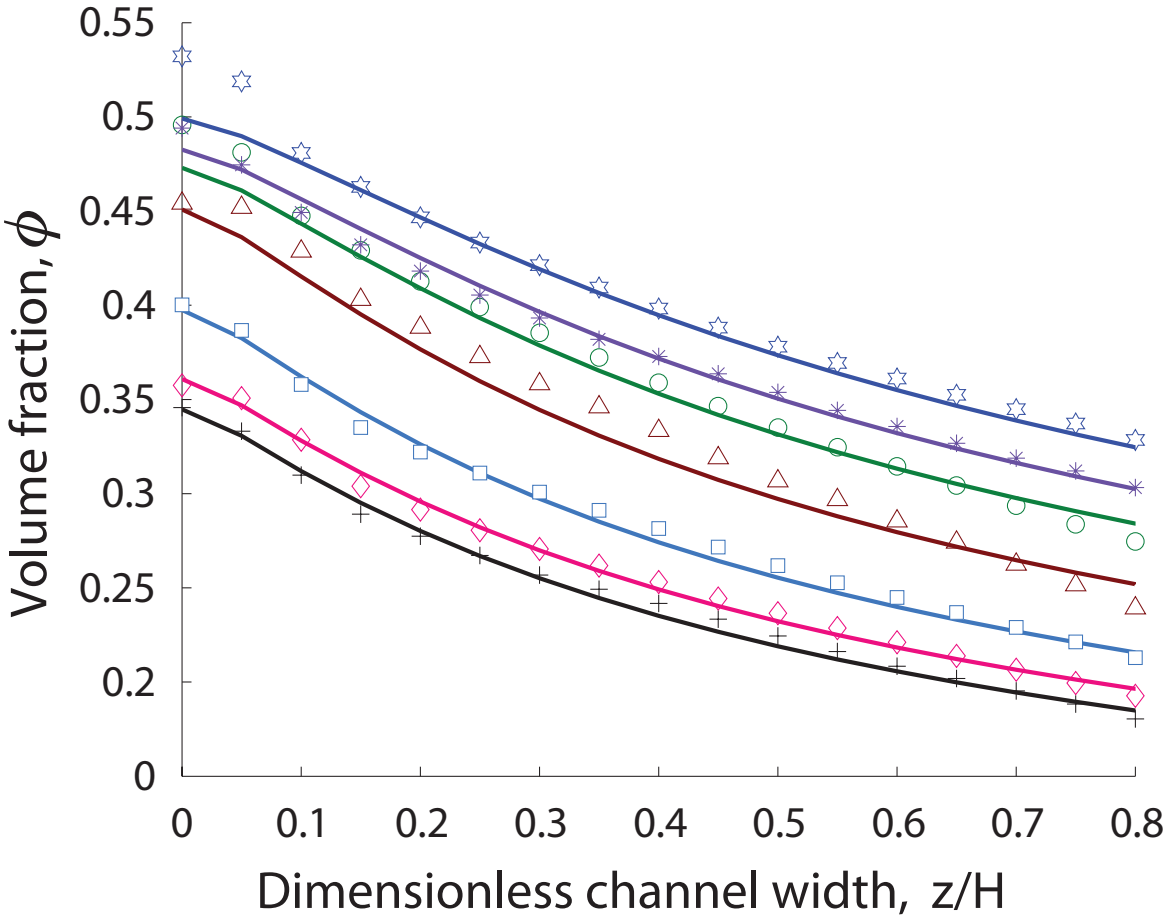

Figure 4.3: Model (solid lines) vs. experiment at average volume fractions, $\phi^a_{bulk} =$ 0.25 (crosses), 0.27 (diamonds), 0.29 (squares), 0.34 (triangles), 0.37 (circles), 0.39 (asterisks) and 0.41 (hexagrams).

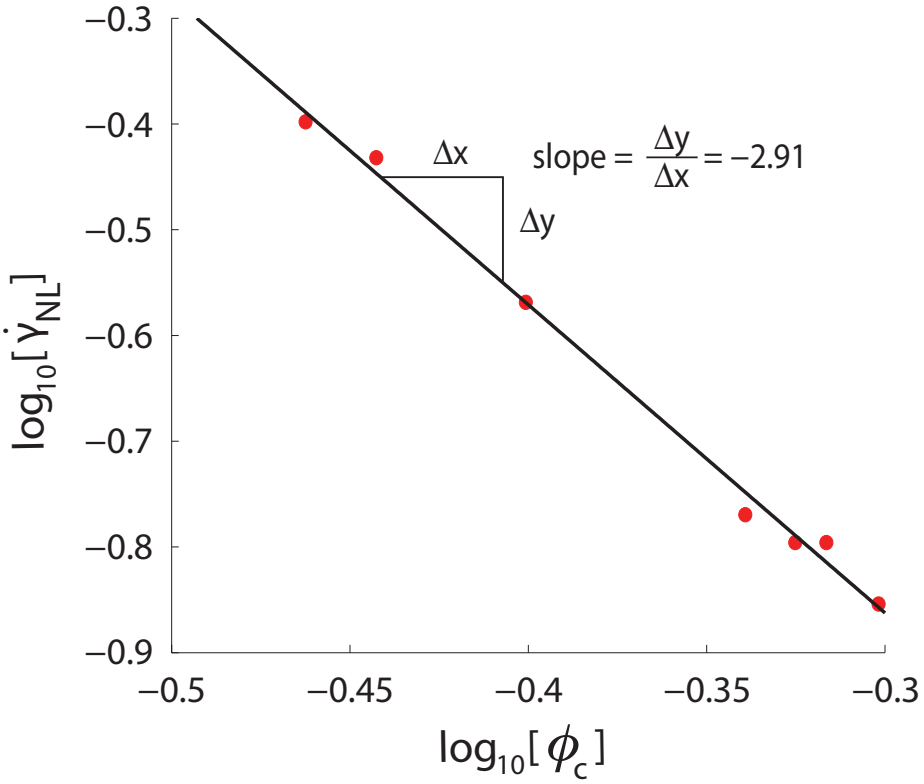

Figure 4.4: Power law correlation between the non-local shear rate $\dot{\gamma}_{NL}$ and volume fraction at channel center, ϕ_c.

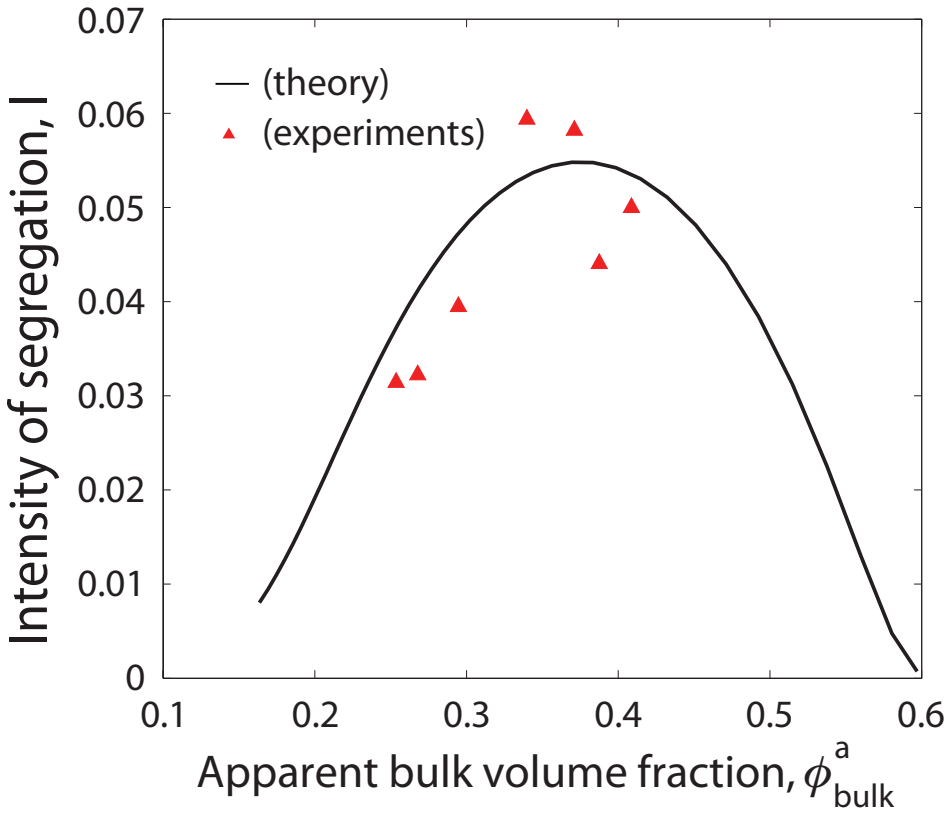

Figure 4.5: Predicted intensity of segregation vs. experiment.

The resulting predicted profiles of volume fraction are plotted against the experimental data sampled near the channel center in Fig. 4.3. Data near the wall are excluded in the analysis because the migration near the wall is enhanced by particle-wall interactions which are lacking from this normal stress balance. The model fits the data well, based on an optimum value of $\dot{\gamma}_{NL}$. The empirical relation between $\dot{\gamma}_{NL}$ and ϕ_c is shown in Fig. 4.4. The magnitude of $\dot{\gamma}_{NL}$ is typically one order of magnitude lower than the average local shear rate. A power law fit results in:

$$\dot{\gamma}_{NL} = 0.0176(\phi_c)^{-2.91} \tag{4.6}$$

The fitting in Eq. 4.6 allows extension of the model to predict the volume fraction profile at different ϕ^a_{bulk} and thus the corresponding intensity of segregations, which is a tool to quantify mixing and/or segregation. Intensity of segregation is defined as

$$I \equiv \frac{\sigma^2}{\phi_{ave}(\phi_{max} - \phi_{ave})} \tag{4.7}$$

modified based on the definition given by Danckwerts (1952), where σ is the standard deviation of ϕ. $I = 0$ indicates perfect mixing and $I = 1$ occurs for complete segregation. Figure 4.5 demonstrates the predicted intensity of segregation for different average volume fractions. It is clearly seen that the model captures the general trend of intensity of segregation and for a plane Poiseuille flow, shear-induced migration is strongest (poorest mixing) near $\phi^a_{bulk} = 0.38$. The experimental data also show a decrease in the intensity of segregation roughly for $\phi^a_{bulk} > 0.34$ (subject to noise), which supports the prediction from the model. This is the first prediction on mixing quality of particle suspension under a certain flow condition.

4.3 Conclusions

A suspension balance model (Morris & Boulay, 1999) was used to predict concentration profile determined by shear-induced migration in a 1D pressure-driven flow. A power-law relation between the non-local shear rate and volume fraction at center was obtained by fitting experimental data of Gao *et al.* (2009) to the model. This relation enables calculation of concentration distribution across the channel at arbitrary bulk volume fractions, which leads to the first prediction of mixing performance for all bulk concentration in the 1D Poiseuille flow. A maximum demixing is expected when $\phi^a_{bulk} = 0.38$.

Chapter 5

Chaotic mixing of suspensions in two-dimensional flow

5.1 Introduction

The previous chapter investigates demixing caused by shear-induced migration in a simple flow. Studies of shear-induced migration in various viscometric flows also exist, e.g. Couette flow (Leighton & Acrivos, 1987*b*; Phillips *et al.*, 1992), flow between parallel plates (Chow *et al.*, 1994), pressure-driven channel flows (Phillips *et al.*, 1992; Lyon & Leal, 1998; Gao *et al.*, 2009), and oscillatory shear flows (Gadala-Maria & Acrivos, 1980; Bricker & Butler, 2006). The general heuristic is that shear-induced migration in steady flows will drive particles to migrate from high-shear regions to low-shear regions while in oscillatory flows it is apparent the steady concentration profiles are more complicated. Interplay between this migration causing gradients in volume fraction ϕ and the concentration-dependent suspension rheology distorts the flow from that of Newtonian fluids. As seen in Fig. 4.1, shear-induced migration

yields concentration gradients and alters velocity variation simultaneously, and thus can have profound interplay with the underlying concentration-dependent rheology.

In a select few studies, shear migration in more complicated geometries that have been explored include steady flows in rectangular lid-driven cavities (Ritz *et al.*, 2000), symmetric and asymmetric channel bifurcations (Altobelli *et al.*, 1997; Moraczewski *et al.*, 2005; Xi & Shapley, 2008; Miller *et al.*, 2009), and open cavity flows (Miller *et al.*, 2009). Recent investigations have expanded to include complex flows exhibiting instability due to shear migration (Gao & Gilchrist, 2008) and chaotic advection (Gao & Gilchrist, 2008; Gao *et al.*, 2009). However, the role underlying flow topology plays in mediating or enhancing shear migration and shear migration's influence on the flow topology is unclear. Developing this understanding is critical since the vast majority of industrial and natural suspension flows exhibit transient and chaotic properties.

In reality more complex time-dependency may be encountered, including that which can induce chaotic advection. Chaos is widely used to enhance mixing, especially under low-Reynolds-number conditions, where instabilities leading to turbulence are suppressed. However often the Péclet number (defined as $Pe \equiv \frac{6\pi\eta_0\dot{\gamma}a^3}{kT}$) is large, meaning that Brownian diffusion is limited and fluid elements move primarily along well-defined streamlines with little randomness. This is pronounced in microfluidics applications and apparent in industrial processes; as a result mixing rates are slow and progress linearly with time. To achieve better mixing, one may resort to chaotic advection by applying time- or space-periodic driving forces to the fluid (Ottino, 1990). In this work, we refer to 'chaos' as continuum transport property as opposed to the chaotic motion of individual constituents leading to diffusion and migration. It can exist when symmetry are broken in a 3D flow or when 2D or 3D flows

undergo time modulation. By making the flow topologically complex, fluid elements that are successively stretched and folded reach molecular length scales exponentially fast, eventually allowing diffusion to dominate. Examples include journal-bearing flow (Muzzio *et al.*, 1992; Niederkorn & Ottino, 1994), lid-driven rectangular-cavity flow (Ottino, 1989*b*) and egg-beater flow (Muzzio *et al.*, 1992).

The relation between chaos and periodicity can be appreciated mathematically (Ottino, 1990). Consider a time-periodic or steady flow that moves a particle initially at position X to x at time t

$$x = \Phi_t(X) \tag{5.1}$$

In Eq.5.1 the flow is expressed as an invertible mapping. A periodic point P with period S satisfies

$$P = \Phi_{nS}(P) \tag{5.2}$$

for $n = 1, 2, 3...$ but not for any $t < S$.

For flows in a closed system, the existence of periodic points is guaranteed by Brouwer's fixed point theorem for every S. In a fluid flow there are three possible sorts of periodic points: elliptic, hyperbolic and parabolic (Fig. 5.1). Elliptic points are surrounded by regular regions, where all particles undergo a net rotation during the cycles. Regular regions form barriers for mixing and inhibit chaotic motions such as stretching and folding. On the other hand, a hyperbolic or saddle point will have some particles approaching while others moving away from it. The former set of particles is called a stable manifold and the latter an unstable manifold. The combination of these two manifolds of one or more hyperbolic points will incur stretchings and foldings of fluid elements, which leads to chaos. Therefore hyperbolic points are essential for

chaotic mixing. While the role of parabolic points on mixing is less important, the coexistence of elliptic and hyperbolic points in fluid systems is ubiquitous and has profound influence on mixing. For instance, in a time-periodic lid-driven cavity flow shown in Fig. 5.2, it is easy to spot regions of good and poor mixing. For the former, many striations develop by stretchings and foldings from a small blob; while regions of poor mixing are characterized by the dark central area where another blob sits, slowly deformed– it marks the regular region around an elliptic point. A useful tool to visualize the periodic points and the manifolds around them is a stroboscopic or Poincaré map, which will be introduced later.

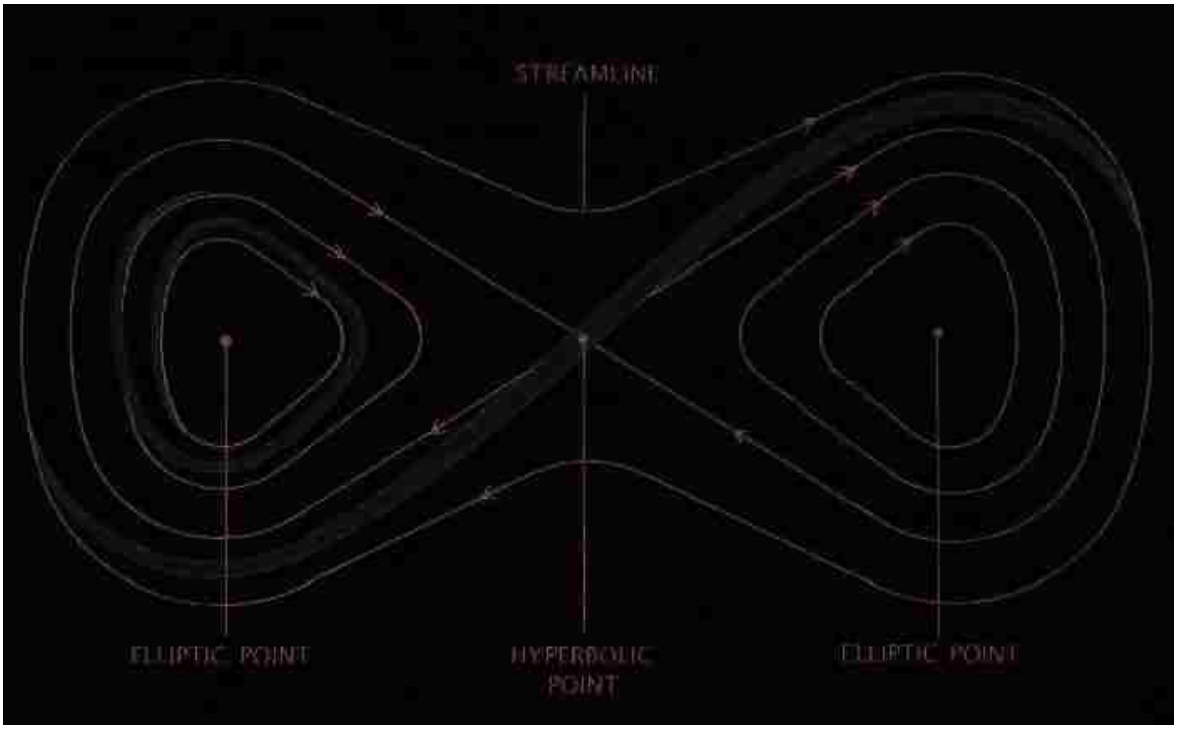

Figure 5.1: Periodic points in fluid flow (Ottino, 1989*b*).

Chaotic advection in fluid flow is complex, and many physical systems have increasing degrees of complexity including scalar (heat or mass) transport and chemical reactions. Interplay between chaotic mixing and segregation driven by body forces, (e.g. (Maxey & Riley, 1983; Abatan *et al.*, 2006)) is more complex, and the interplay between chaos and rheology-driven migration is perhaps the most complex. Permutations of combinations of these effects become increasingly complex (e.g. heat transport and reaction in chaotic flows). Studies have considered the effects of shear thinning (Niederkorn & Ottino, 1994) and elasticity (Niederkorn & Ottino, 1993) on the flow topology of chaotic advection without migration or phase change. The general assumption is chaotic advection, without the increase of shear rate or energy input, would mediate shear migration-driven segregation and enhance dispersion. In contrast, granular flows are known to segregate readily due to body force-driven demixing during chaotic advection in 2D (Kharkhar *et al.*, 1999; Hill *et al.*, 1999) and 3D (Gilchrist & Ottino, 2003) flows.

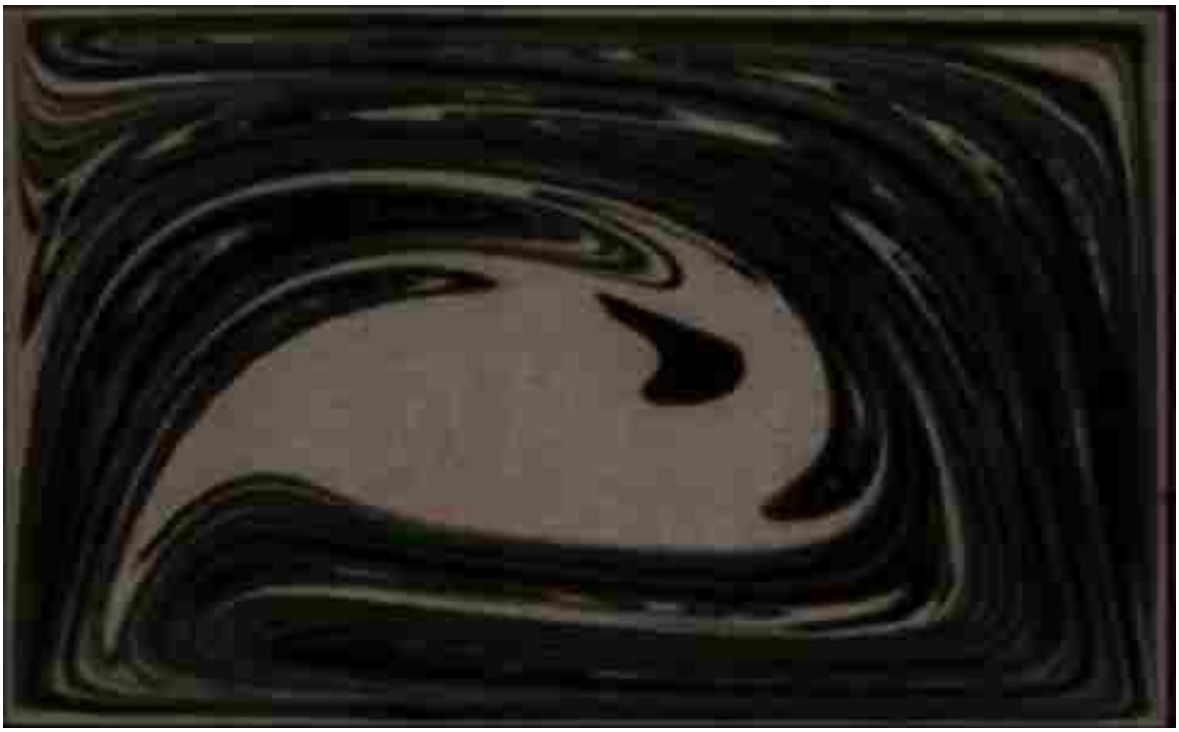

Figure 5.2: Chaotic mixing in a cavity flow (Ottino, 1990).

We study the behavior of suspensions with varying degrees of shear migration in a prototypical chaotic flow known as time-periodic lid-driven cavity flow (Ottino, 1989*a*,*b*). This allows for the following two independent modes of probing the interplay between chaotic advection and segregation resulting from shear migration. First, we can adjust the topology of the flow without increasing the energy input into the system. This breaks the symmetry of the flow and tunes the time-periodicity to generate very weakly chaotic to chaotic advection-dominated flows. Second, we can adjust the suspension properties including relative particle size and average volume fraction to tune the rate of migration. This study aims to generate a set of heuristics by which one can better understand the effect of this interplay between rate of migration and chaotic mixing in the generation of nontrivial segregation patterns. The following sections are based on the work published in Xu & Gilchrist (2010).

5.2 Formulation

Widely used models that have been proposed fall into two categories: the diffusive flux approach (Phillips *et al.*, 1992; Subia *et al.*, 1998) and the suspension stress approach (Nott & Brady, 1994; Morris & Boulay, 1999). Each of these models have limitations, including neglecting particle-wall interactions and excluded volume and singularity at localized zero shear rate (Morris & Boulay, 1999) and high curvature. For simplicity of implementation, non-colloidal spherical particles dispersed in a Newtonian fluid is modeled by a diffusive-flux approach (Phillips *et al.*, 1992), where the change of local volume fraction ϕ is governed by

$$\frac{D\phi}{Dt} = a^2 K_c \nabla \cdot (\phi^2 \nabla \dot{\gamma} + \phi \dot{\gamma} \nabla \phi) + a^2 K_\eta \nabla \cdot (\dot{\gamma} \phi^2 \frac{1}{\eta} \frac{\partial \eta}{\partial \phi} \nabla \phi) \tag{5.3}$$

where a is particle radius, $\dot{\gamma}$ is shear rate. The coefficients K_c and K_c for the two fluxes are assumed constant and fitted from experimental data in Couette and pressure-driven tubular flows: $K_c = 0.41$ and $K_\eta = 0.62$. Note that for a characteristic system size of L, the characteristic rate of migration is proportional to $\lambda = (a/L)^2$. The viscosity of the suspension is approximated by the Krieger-Dougherty relation (Krieger, 1972)

$$\eta = \eta_0 (1 - \frac{\phi}{\phi_m})^{-1.82} \tag{5.4}$$

where η_0 is the viscosity for the interstitial Newtonian fluid.

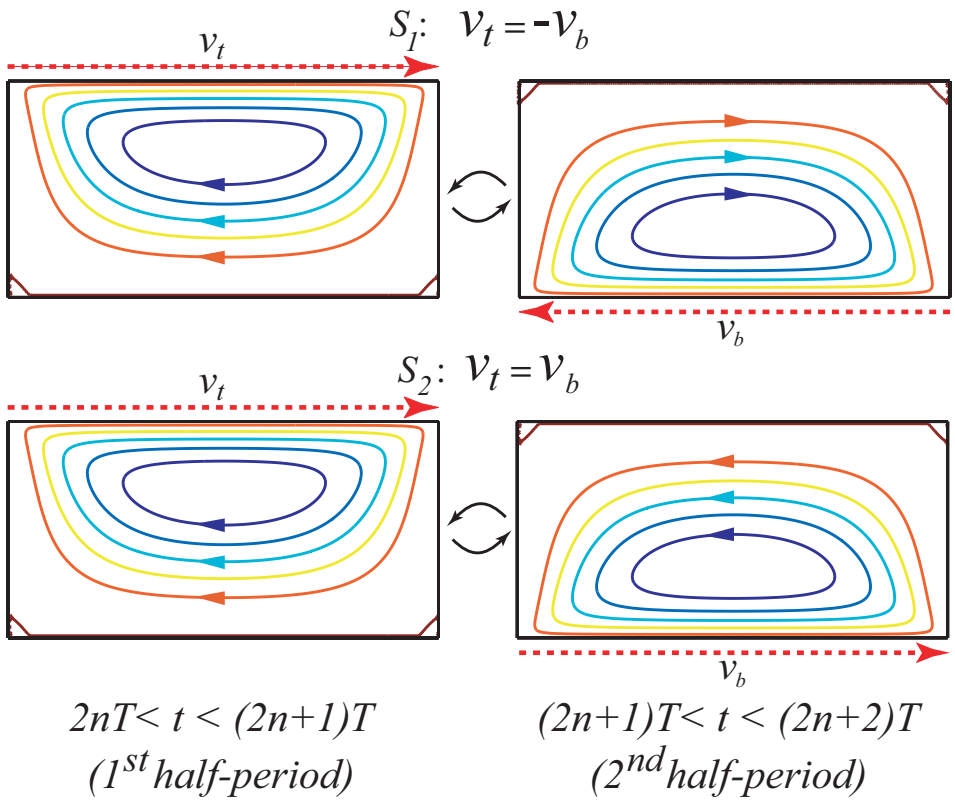

Figure 5.3: Mixing protocols and instantaneous streamlines for the time-periodic lid-driven cavity. S_1 (top) advances the upper lid to the right at velocity v_t for time T the half-period of the cycle and then advances the lower lid to the left at $v_b = -v_t$ for T. S_2 (bottom) advances the upper lid v_t for T and the lower lid $v_b = v_t$ for T. Each protocol is repeated until a steady concentration profile at the end of each cycle $2T$ is obtained.

Neumann boundary condition is applied to ensure no flux across any wall and ϕ is assumed a uniform value ϕ_{ave} at $t = 0$. In relation to the limitations described above, this model does not consider curvature-driven flux (Krishnan *et al.*, 1996) resulting from particle interactions on neighboring curved trajectories. In select simulations incorporating this flux, the effect of curvature-induced migration is strongest near the corners strengthening the near-corner concentration gradients presented here. The continuum description of the behavior of discrete particles for increasing λ is challenged in these regions, not considered in any of the above models.

It is shown that within Stokes-flow regime, 2D steady flow results only in simple closed streamlines. Chaotic advection can be achieved by applying periodic driving forces to the fluid (Ottino, 1990). Examples of closed flow exhibiting chaos include journal-bearing flow (Muzzio *et al.*, 1992; Niederkorn & Ottino, 1994), lid-driven rectangular-cavity flow (Ottino, 1989*b*) and egg-beater flow (Muzzio *et al.*, 1992). In this work, we consider the 2D time-periodic lid-driven cavity flow in a rectangular cavity with height L and an aspect ratio 2:1. As is shown in 5.3, the top and bottom walls are sliding alternately with equal velocity, for some equal length of time. We normalize time length by dividing by a characteristic time $t_{slide} = L/v_{slide}$. Therefore, $t_{slide} = 1$ is the time for an element on the wall to traverse L. Another parameter that affects mixing is the moving wall direction. Two different situations are possible: when the top and bottom walls slide in opposite directions (e.g. top wall from left to right, then bottom wall from right to left), it is called S_1; when the two walls move in the same direction (e.g. top wall from left to right, then bottom wall), we call it S_2. The length for a full cycle of alternating flow is defined as a "period" T. Assuming a

vanishingly small Reynolds number, the momentum transport of the flow is given by

$$-\nabla p + \nabla \cdot (\eta(\nabla \mathbf{v} + \nabla \mathbf{v}^t = 0) \tag{5.5}$$

and

$$\nabla \cdot \mathbf{v} = 0 \tag{5.6}$$

The boundary condition can be described as

$$v_{top} = v_{slide},\ v_{bottom} = 0, \quad 2nT < t < (2n+1)T; \tag{5.7}$$

$$v_{top} = 0,\ v_{bottom} = \pm v_{slide}, \quad (2n+1)T < t < 2(n+1)T \tag{5.8}$$

where on the second line, the plus sign stands for S_2 and minus sign for S_1 and $n = 0, 1, 2, ...$

We simulate the evolution of concentration and velocity in time (Comsol Multiphysics 3.4). A dimensionless 2D rectangular container with an aspect ratio of 2:1 is used. The flow velocity and pressure are represented by 2D $P_2^+P^{-1}$ (Crouzeix-Raviart) elements and concentration by 2D quadratic Lagrange elements. Equations (1-4) combined with the boundary conditions are solved by the GMRE solver. We have varied different values for particle radius λ, period T and average volume fraction ϕ_0 to investigate their impact on particle distribution under the two different scenarios, S_1 and S_2, previously defined.

5.3 Results

Steady lid-driven cavity flow is studied at an average bulk volume fraction $\phi_{ave} = 0.2$. Although many previous studies of shear migration investigate $\phi_{ave} > 0.4$, $\phi_{ave} > 0.1$ is sufficient to drive significant concentration gradients (Gao & Gilchrist, 2008; Gao *et al.*, 2009). Fig. 5.4a shows the steady-state shear rate profile from the lid-driven cavity flow at $\lambda = 0.01$. Despite the strong viscosity gradients resulting from migration, the horizontal symmetry suggests only a small deviation (6%)of $\mathbf{v}$ in a Newtonian fluid. As expected, $\dot{\gamma}$ is highest near the upper moving boundary and lowest in the lower corners opposite the moving boundary. A band of lower $\dot{\gamma}$ extends from the upper corners to just below the center of the cavity. There are no transients associated with the start or stop of the wall at $Re = 0$.

Concentration profiles for steady cavity flows with increasing degrees of migration $\lambda = 1\times10^{-4}$, 2.5×10^{-3}, and 1×10^{-2} are shown in Fig. 5.4b-d to demonstrate the effect of migration in this shear profile in the absence of chaotic advection. The concentration scale bar in these plots is the same [0,0.4] for direct comparison, and shows that these results are nearly identical to previous simulations (Ritz *et al.*, 2000). For relatively weak migration, $\lambda = 1\times10^{-4}$, the steady concentration profile is uniform with the exception of two bands of slightly higher and lower concentration extending from the upper corners to the lower boundary. Concentration gradients are slightly larger on the right side of the cavity downstream of the flow near the upper wall. The closed streamlines of this flow inhibit migration toward the center. With increasing degree of migration the concentration gradients become more pronounced and more asymmetric with respect to a reflection across the vertical midplane. At $\lambda = 2.5\times10^{-3}$ particles migrate further into the center and more strongly into the lower corners. The local minimum in shear rate, which forms a curved valley extending from center to the two upper corners (Fig. 5.4a)), results in a local maximum concentration region as well. Instead of sitting exactly in the low shear rate basin, however, this high-concentration band is deformed and transported by convection forming discernible asymmetry. At $\lambda = 1\times10^{-2}$ the island in the center exists as well, but it has more pronounced asymmetry with particles concentrated on the left side and a lobe of low concentration near the right wall. Conditions approach $\phi = 0$ and $\phi = 0.4$ in localized low and high concentration regions of the flow. The bottom corners have two spires having the highest concentration that point toward the upper corners. The same high concentration regions are also found in the previous study (Ritz *et al.*, 2000). Generally, the particles migrate from regions of high shear rate to regions of low shear

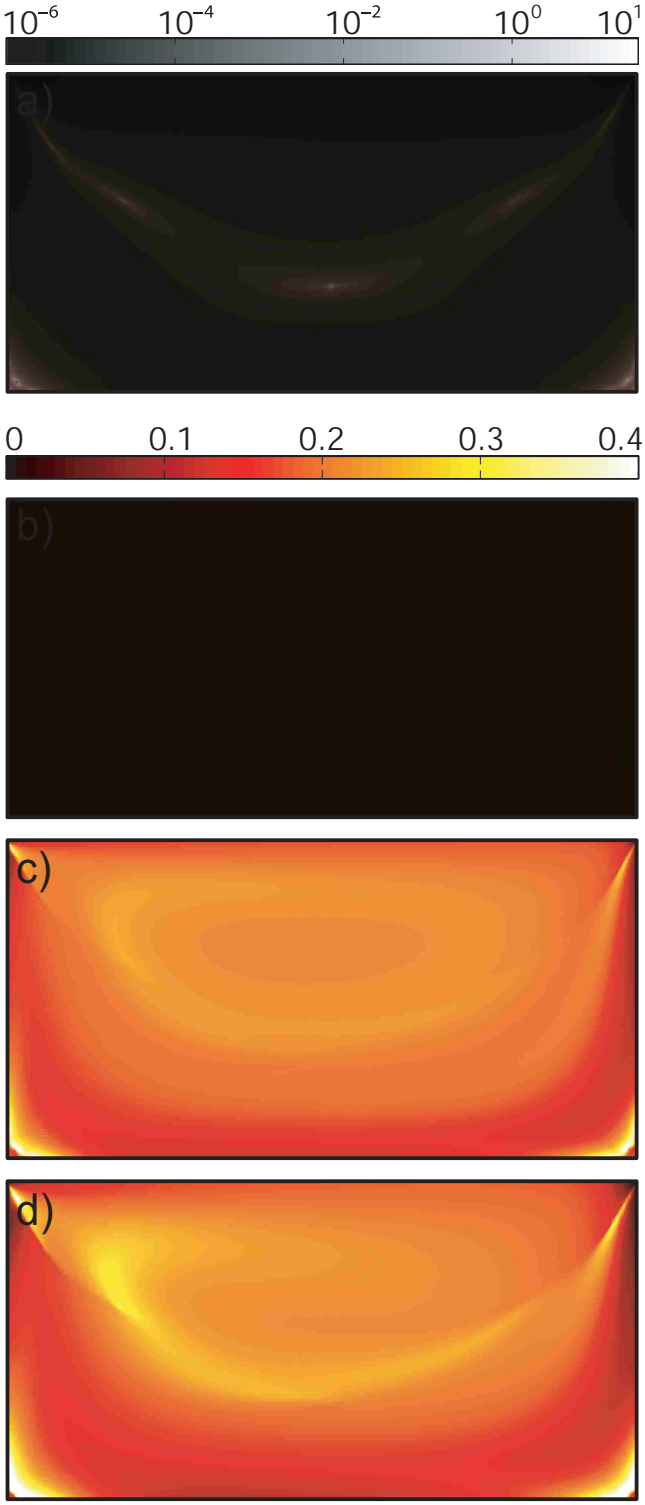

Figure 5.4: a): Shear rate profile in a steady lid-driven cavity flow with $\phi_{ave} = 0.2$ and $\lambda = 1{\times}10^{-2}$; b), c) and d): Steady concentration profiles for $\lambda = 1{\times}10^{-4}$ (b), $2.5{\times}10^{-3}$ (c) and $1{\times}10^{-2}$ (d).

rate; this migration breaks the symmetry that would exist without migration in the underlying flow and this material convection forms the central high concentration island. This segregation resulting from shear migration has significant ramifications regarding heat or mass transport from the walls to the center.

We now consider the effect of migration in chaotic flows. Figs. 5.5 and 5.6 show the simulations results of 16 different flows for S_1 and S_2, respectively. T increases from top to bottom, effectively increases the degree of chaotic mixing. Increasing T also means that the system spends more time as a steady flow during each half-cycle of the period. From left to right the degree of migration increases. The first column is the Poincaré or stroboscopic map of the Newtonian flow with increasing T. This is produced by advecting a number of initial positions and selectively plotting their locations at the end of each cycle. This results in a cross section of the underlying dynamics and highlights invariant features of the flow including elliptical periodic points at the center of regular regions, unstable periodic points that can result in regions of chaotic mixing, and closed trajectories and chains of periodic orbits that form KAM surfaces (Lichtenberg & Lieberman, 1983; Hilborn, 1994) which both act as barriers to transport. The columns to the right of the Poincaré maps are concentration profiles with increasing strength of migration and decreasing λ. Each column has a scale bar highlighting concentration gradients and allowing comparison with the underlying flow portrayed by the corresponding Poincaré map.

For S_1, the boundary conditions of the two half-periods of the flow have rotational symmetry through the center. For Newtonian fluids the topology of the flow has x-axis symmetry as seen in the Poincaré maps. For $T = 3/4$ (Fig. 5.5a) a regular region exists to the right of center and most of the flow is non- or weakly chaotic. With migration at $\lambda = 1{\times}10^{-4}$ (Fig. 5.5b), the Poincaré map's underlying structure is apparent and the concentration profile has similar features to those resulting from migration in steady flow. The lowest concentration is at the boundaries, and higher concentration rings are found just inside the boundary and slightly right of the center

Figure 5.5: Poincaré maps and concentration profiles of suspensions in S_1. The vertical direction probes the influence of time T the half-period of the cycle, while the horizontal direction examines increasing degree of migration. The left column is Poincaré maps representing the evolution of initial conditions plotted after every period $2T$, with vertically symmetric topology stemming from the symmetry of the boundary conditions. The 2^{nd}, 3^{rd}, and 4^{th} columns are concentration profiles plotted at the end of each cycle demonstrating the topology of segregation with $\lambda = 1{\times}10^{-4}$, $2.5{\times}10^{-3}$, and $1{\times}10^{-2}$. The topology represented in the Poincaré map is visible at low T and λ. High T and λ result in segregation profiles that mimic the steady profile seen in Fig. 5.4d rotated 180°

Figure 5.6: Poincaré maps and concentration profiles of suspensions in S_2. The vertical direction probes the influence of time T the half-period of the cycle, while the horizontal direction examines increasing degree of migration. The left column is Poincaré maps representing the evolution of initial conditions plotted after every period $2T$, with 180° rotationally symmetric topology stemming from the symmetry of the boundary conditions. The 2^{nd}, 3^{rd}, and 4^{th} columns are concentration profiles plotted at the end of each cycle demonstrating the topology of segregation with increasing rates of shear migration $\lambda = 1\times10^{-4}$, 2.5×10^{-3}, and 1×10^{-2}. The topology represented in the Poincaré map is visible at low T and λ. High T and λ result in segregation profiles that when vertically reflected mimic the steady profile seen in Fig. 5.4d and when horizontally reflected mimic Fig. 5.5p.

of the channel. The invariant structures surrounding the center island are barriers to transport. At $\lambda = 2.5\times10^{-3}$ (Fig. 5.5c) the concentration profile resulting from stronger shear migration shows features deviating from the underlying topology. The central ring is much higher in concentration and lines of higher concentration extend from each corner toward the center. At $\lambda = 1\times10^{-2}$ (Fig. 5.5d) shear migration pushes most particles in suspension toward the middle with the exception of thin lines of higher concentration near the upper left and lower corners oriented toward corresponding higher-concentration lines extending from the center.

For S_1 and $T = 3/2$ (Fig. 5.5e-h) the Poincaré map looks significantly different from $T = 3/4$. A regular region exists right of center; however, here the flow topology is dominated by a period-5 chain of islands. This topography is a common bifurcation when breaking flow symmetries. Material in each of the period-5 islands and the center-most island is confined by KAM surfaces. Transport across these surfaces in a Newtonian fluid is diffusion-limited and in a suspension occurs either through diffusion or migration. This underlying structure is apparent in $\lambda = 1\times10^{-4}$, where each island is close to $\phi_{ave} = 0.2$, and is surrounded by higher concentration regions. These islands still exist at $\lambda = 2.5\times10^{-3}$, but the positions of the period-5 regular regions have shifted slightly counter clockwise. A center ring of high concentration is more pronounced and the boundaries share profile characteristics with $T = 3/4$ and $\lambda = 2.5\times10^{-3}$. At $T = 3/2$ and $\lambda = 1\times10^{-2}$ the concentration profile is most similar to $T = 3/4$ and $\lambda = 1\times10^{-2}$ - the exception to this similarity is that the center region is slightly higher in concentration and shifted to the right.

At $T = 5/2$ for S_1 (Fig. 5.5i-l) the flow is more chaotic, with the topology again dominated by regular regions, islands to the right of the center are much smaller than

those seen at lower T, and two sets of larger period-3 islands. One set of period-3 islands has one left island and two additional islands located near the top and bottom chaotic regions following close to the boundaries. The other set of period-3 islands, located in a chaotic region bounded by a KAM surface and completely surrounded by the chaotic region near the boundaries, has two islands near the left and one island near the right boundaries. In this concentration map shear migration does not follow the underlying topology as closely as in flows with shorter T. The concentration gradients are increasingly striated and the concentration is lower within the internal chaotic region; two lobes of lower concentration extend from the center to the left corners suggesting the bounding KAM surface inhibits migration into this region. At $\lambda = 2.5\times10^{-3}$ the concentration profile is the inverse of that at $\lambda = 1\times10^{-4}$. The concentration in the center region is higher, two bands of higher concentration extend from the center toward the left corners, and one band extends toward the lower right corner. Near the boundaries the concentration profile is similar to $T = 3/4$ and $3/2$ at $\lambda = 2.5\times10^{-3}$. The segregation patterns at the corners feed particles into the interior chaotic region. Stronger concentration gradients exist at $\lambda = 1\times10^{-2}$ and the center region of high concentration is more pronounced than at $T = 3/2$ and shifted further to the right.

At $T = 6$ (Fig. 5.5m-p) in the Poincaré map chaotic advection dominates everywhere except in a small group of islands located to the left. Many bifurcations occur in the range $5/2 < T < 6$ and are too numerous to make practical an elaboration of the entire evolution. The concentration profile at $\lambda = 1\times10^{-4}$ has many striations including a larger band of higher concentration circulating upward from the lower left corner. With increasing λ the suspension segregates more. At $\lambda = 1\times10^{-2}$ the

concentration profile rotated 180° is similar to the steady profile shown in Fig. 5.4d because this flow spends a significant amount of time in each half cycle and is the limiting case as $T \to \infty$.

A similar analysis is performed for S_2 in Fig. 5.6. This flow generates the exact same instantaneous shear rate distribution as S_1, except that boundary conditions have horizontal reflectional symmetry across the x midplane. This broken symmetry results in 180° rotationally symmetric topology. In Fig. 5.6a the Poincaré map for $T = 3/4$ shows two regular regions separated by an invariant surface extending from the right to left boundary. Circulation is clockwise in the upper regular region and counter-clockwise in the lower regular region. The regular regions are smaller at $T = 3/2$ (Fig. 5.6e) and surrounded by higher period island chains and a chaotic region extending to the boundaries. For $T = 5/2$ (Fig. 5.6i), these regular regions are smaller and each has surrounding large period-4 islands. At $T = 6$ (Fig. 5.6m) the original regular regions are no longer discernible with two distinct sets of period-2 islands taking their place.

Concentration profiles for S_2 is significantly different than those for S_1 because of the transport from the right to the left boundary through the center of the cavity. Fig. 5.6b, $\lambda = 1{\times}10^{-4}$, shows lower concentration at the right and left boundaries as well as across the center in a horizontal jet. On either side of the jet $\phi_{ave} > 0.2$ bounding the two regular regions with $\phi \approx 0.2$. The topology of the Poincaré map dominates the shape of the segregation profile at low T. For $T = 3/2$ and $5/2$ at $\lambda = 1{\times}10^{-4}$ (Figs. 5.6f,j respectively) the center jet of lower concentration buckles but does not enter the area corresponding to the Poincaré map regular regions. At $T = 6$ (Fig. 5.6n), the jet is located far from the center near the upper wall and between the

two upper islands. This buckling breaks the rotational symmetry of the underlying topology.

For stronger migration at $\lambda = 2.5\times10^{-3}$ (column 3, Figs. 5.6c,g,k,o) the concentration profile has stronger concentration gradients with similar topology to $\lambda = 1\times10^{-4}$. The higher concentration regions form near the corners as in S_1, $\lambda = 2.5\times10^{-3}$ and 1×10^{-2}. For very strong migration, $\lambda = 1\times10^{-2}$, the jet of lower concentration is less clear (right column, Figs. 5.6d,h,l,p). These concentration profiles, if reflected across the x midplane, have similar features to Fig. 5.4d and thus demonstrate that unlike in S_1 the underlying flow topology has little effect on demixing regardless of T.

The effect of T on demixing in each concentration profile can be quantified by calculating the intensity of segregation. Intensity of segregation, used as a tool to compare these results across the various flow profiles, is defined as

$$I \equiv \frac{\sigma^2}{\phi_{ave}(\phi_m - \phi_{ave})} \tag{5.9}$$

based on the definition given by Danckwerts (1952), where σ is the standard deviation of ϕ. $I = 0$ indicates perfect mixing and $I = 1$ occurs for perfect segregation. Fig. 5.7 shows S_1 and S_2 at $\lambda = 1\times10^{-2}$ and $\phi_{ave} = 0.2$. I is normalized by I_0 the intensity of segregation in the steady lid-driven cavity, calculated for Fig. 5.4b. For $T \leq 6$ S_1 enhances segregation equal to or exceeding that found in steady lid-driven cavity where $I \cong 0.0225$. This enhanced segregation is due to the formation of the high concentration island seen in Fig. 5.5d,h,l,p. For $T > 6$ this island becomes insignificant and results in a sharp drop in I. This island is not formed in S_2 and thus chaotic advection only reduces segregation resulting from shear migration. Both S_1 and S_2 have asymptotes at $I \cong 0.0225$ as $T \to \infty$ because each half of the period is long

enough to reach a steady profile similar to that found in steady lid-driven cavity flow.

Finally, we investigate the effect of ϕ_{ave} on mixing and shear migration in this flow. Fig. 5.8 shows $0.1 \leq \phi_{ave} \leq 0.4$ for S_1, $T = 3/2$. Shear migration-driven segregation is non-existent at $\phi_{ave} = 0$ and $\phi_{ave} = \phi_m$ is strongest at an intermediate ϕ_{ave} Gao & Gilchrist (2008). For $\phi_{ave} \leq 0.3$ (Figs. 5.7a-c) the underlying topology shown in Fig. 5.5e influences the segregation pattern and $\phi > \phi_{ave}$ surrounds the period-5 and central islands. For $\phi_{ave} \geq 0.3$ migration to the center of the cavity effectively washes out the period-5 islands. As $\phi_{ave} \rightarrow \phi_m$, the computation becomes unstable due to lack of resolution; in this limit the underlying flow varies significantly due to the increasingly non-Newtonian behavior of the suspension.

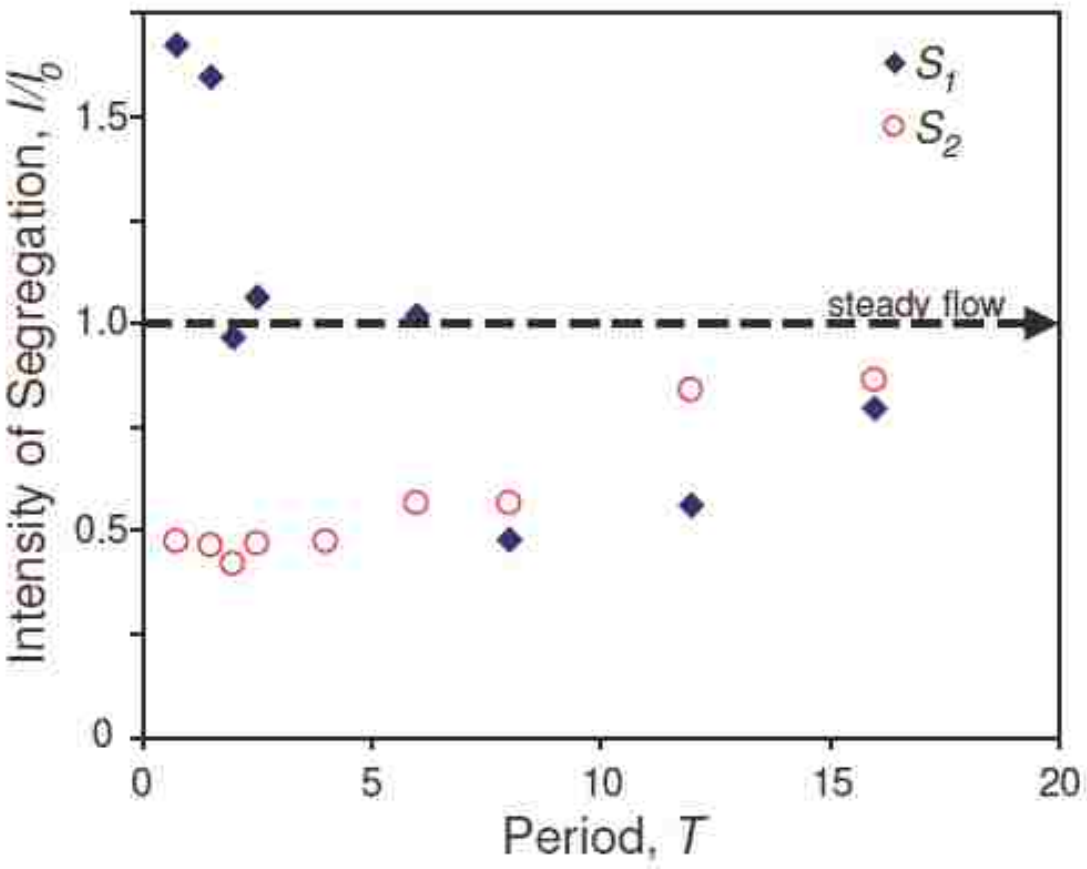

Figure 5.7: Intensity of segregation I/I_0 vs. period T for S_1 (diamonds) and S_2 (circles) at $\lambda = 1{\times}10^{-4}$ and $\phi_{ave} = 0.2$. The dotted line indicates I/I_0 in the steady lid-driven cavity under the same conditions equivalent to $T \to \infty$, .

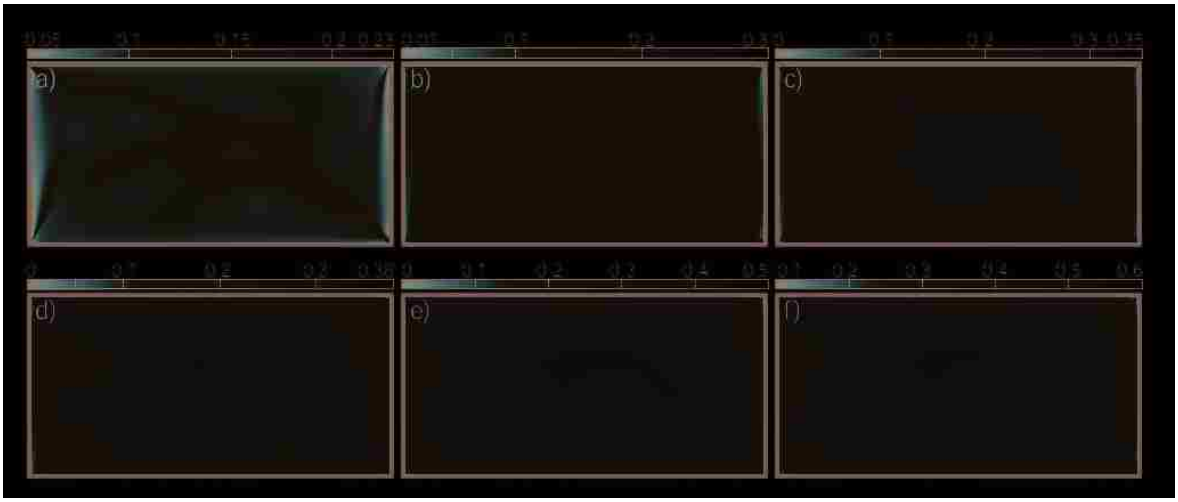

Figure 5.8: Concentration profiles plotted at the end of each cycle of $T = 3/2$, $\lambda = 1{\times}10^{-4}$ and $\phi_{ave} = 0.1$ (a), 0.15 (b), 0.25 (c), 0.3 (d), 0.35 (e), 0.45 (f). The scalebar of each profile has been adjusted to enhance the resolution of the segregation structure. There is no segregation in the limits $\phi_{ave} \to 0$ and $\phi_{ave} \to \phi_m$

5.4 Conclusion

The interplay between 2D time-periodic chaotic advection in a lid-driven cavity and shear migration of a suspension is highly complex. Though S_1 and S_2 only differ in the translation direction of the bottom wall, this difference has a large effect on resulting flow topology. At low T S_1 produces a single recirculating flow with structure topologically similar to that of a steady lid-driven cavity. Because shear migration is strongest near the walls S_1 effectively has twice the surface area acting to shear fluid and I is roughly twice that of the steady case. In contrast S_2 produces two recirculation regions at low T with fluid convecting across the middle from the right to left boundary. Concentration gradients produced near the wall are advected into the center and as a result I is roughly half that of the steady flow. Consequently, the same energy input into the system the flow can either enhance or reduce segregation. Similarly, at higher T the underlying topology has a much larger area covered by chaotic trajectories. However, the interplay with migration is such that for $T \to \infty$, S_1, S_2, and steady flow converge on the same intensity of segregation. Both of these results contradict the perception that increasing the degree of chaos in the flow will enhance overall mixing.

To develop a full set of heuristics for the influence of shear migration on mixing and segregation in chaotic flows, a broader class of flows needs to be explored, especially 3D flows and open flows. This analysis could develop mixing and separations on microscale platforms that depend only on suspension rheology eliminating the need to incorporate complicated MEMS to achieve desired concentration profiles.

Chapter 6

Conclusions and outlook

In this work we have studied microstructure and rheology of sheared suspension under microfluidic conditions. Direct visualization of the microstructure is rendered possible by confocal microscopy. The results agree with previous theoretical predictions and computations. Pair-wise calculation is conducted to obtain rheological functions from the microstructure. Comparison with SD simulation is made and qualitative agreement established. Analyses show hydroclusters exist in sheared suspensions and grow linearly with $ln(Pe)$, responsible for shear-thickening under high shear rates. Shear-induced crystallization is pronounced for Pe >1000. Electrostatic force is found to play a dubious role in either reducing or enhancing order in structure, depending on its magnitude. Strong electrostatics will make shear-induced crystallization noticeable for $Pe \sim O(100)$. The microstructural study helps us understand rheology in real life processing of suspensions. Investigation of shear-migration effect on mixing is carried out in this context. Macroscopic model reveals competition as well as coordination between flow topology and migration, further complicating suspension rheology. Mixing protocols with the same strain rate can perform very differently

in terms of the intensity of segregation. New insights are shed on design of mixing device for suspensions.

Our current experimental setting, though is convenient and economical to produce large amount of data over a spectrum of Pe's, has its limitations. First, the nonlinear shear field in pressure-driven channel flow causes concentration inhomogeneity as a result of shear-induced migration, making decoupling of shear rate and concentration difficult. Second, all the rheological functions in this study are obtained based on pair correlation data under near-field approximation. It is always preferential to have rheo-optics measurement simultaneously to provide more objective mechanical results. Third, the nitrogen-driven flow in microchannel is stable in steady flow, but the current system is not easy to realize operations such as oscillatory shear or reversed shear with precisely controlled strain.

An upgrade of the system may thus be amounting to confocal microscope a mechanically-driven shear cell which carries out simple shear, oscillatory shear, quick flow cessation and force/torque measurement, etc. Synchronization between the force/torque measurement and imaging part is needed. With this setting, factors like concentration and shear rate can be individually controlled and rheological effects like shear-thinning/thickening are readily captured with their corresponding microstructures. Cheng *et al.* (2011)'s design is toward this direction, but not careful enough to rule out influences from the cell wall.

With the new system, it is possible to study the destroy and formation of microstructure with shear. From Gadala-Maria & Acrivos (1980) we know when shear is reversed, structure will decompose and reform in the new direction. A microstructural study in reversed shear flow with precise strain would be very meaningful in

understanding the mechanism and dynamics of this process. Oscillatory shear experiments can obtain the complex viscosity, loss and storage moduli, etc, of a suspension along with the microstructure, therefore provide new insights into the coupling of structure and rheology.

Although our numerical study reveals much information in real processing of suspensions, up to now, as our understanding of microstructure-based suspension rheology is not sufficiently deep, most macroscopic models may fall short of being quantitatively accurate for a *general* circumstance. Particle-level simulations, e.g. Stokesian Dynamics are more reliable but meanwhile costly. It is envisioned that a multi-scale approach integrating simulations on both levels would yield an optimal performance.

Bibliography

Abatan, A. A., McCarthy, J. J. & Vargas, W. L. 2006 Particle migration in the rotating flow between co-axial disks. *AICHE J.* **52**, 2039–2045.

Ackerson, B. J., Hayter, J. B., Clark, N. A. & Cotter, L. 1986 Neutron scattering from charge stabilized suspensions undergoing shear. *J. Chem. Phys.* **84**, 2344–2349.

Adamson, A. W. & Gast, A. P. 1997 *Physical chemistry of surfaces*, sixth edn. John Wiley & Sons Inc.

Aidun, C. K. & Clausen, J. R. 2010 Lattice-Boltzmann method for complex flows. *Annu. Rev. Fluid Mech.* **42**, 439–472.

Altobelli, S. A., Fukushima, E. & Mondy, L. A. 1997 Nuclear magnetic resonance imaging of particle migration in suspensions undergoing extrusion. *J. Rheol.* **41**, 1105–1115.

Arora, A. K. & Tata, B. V. R. 1998 Interactions, structural ordering and phase transitions in colloidal dispersions. *Adv. Colloid Interface Sci.* **78**, 49–97.

Banchio, A. J. & Brady, J. F. 2003 Accelerated Stokesian Dynamics: Brownian motion. *J. Chem. Phys.* **117**, 10323–10332.

Batchelor, G. K. 1976 Brownian diffusion of particles with hydrodynamic interaction. *J. Fluid Mech.* **74**, 1–29.

Batchelor, G. K. & Green, J. T. 1972*a* The determination of the bulk stress in a suspension of spherical particles to order c^2. *J. Fluid Mech.* **56**, 401–427.

Batchelor, G. K. & Green, J. T. 1972*b* The hydrodynamic interaction of two small freely-moving spheres in a linear flow field. *J. Fluid Mech.* **56**, 375–400.

Beckham, R. E. & Bevan, M. A. 2007 Interfacial colloidal sedimentation equilibrium. I. intensity based confocal microscopy. *J. Chem. Phys.* **127**, 164708.

Bender, J. W. & Wagner, N. J. 1995 Optical measurement of the contributions of colloidal forces to the rheology of concentrated suspensions. *J. Colloid Interface Sci.* **172**, 171–184.

Bender, J. W. & Wagner, N. J. 1996 Reversible shear thickening in monodisperse and bidisperse colloidal dispersions. *J. Rheol.* **40**, 899–916.

Berend, K. & Richtering, W. 1995 Rheology and diffusion of concentrated monodisperse and bidisperse polymer latices. *Colloids Surf.* **99**, 101–119.

van Blaaderen, A. & Vrij, A. 1992 Synthesis and characterization of colloidal dispersions of fluorescent, monodisperse silica spheres. *Langmuir* **8**, 2921–2931.

Blanc, F., Peters, F. & Lemaire, E. 2011 Local transient rheological behavior of concentrated suspensions. *J. Rheol.* **55**, 835–854.

Bossis, G. & Brady, J. F. 1989 The rheology of Brownian suspensions. *J. Chem. Phys* **91**, 1866–1874.

Brady, J. F. & Bossis, G. 1985 The rheology of concentrated suspensions of spheres in simple shear flow by numerical simulation. *J. Fluid Mech.* **155**, 105–129.

Brady, J. F. & Bossis, G. 1988 Stokesian Dynamics. *Annu. Rev. Fluid Mech.* **20**, 111–157.

Brady, J. F. & Morris, J. F. 1997 Microstructure of strongly sheared suspensions and its impact on rheology and diffusion. *J. Fluid Mech.* **348**, 103–139.

Breedveld, V., van den Ende, D., Jongschapp, R. & Mellema, J. 2001 Shear-induced diffusion and rheology of noncolloidal suspensions: time scales and particle displacements. *J. Chem. Phys* **114**, 5923–5936.

Brenner, H. 1963 The Stokes resistance of an arbitrary particle. *Chem. Eng. Sci.* **18**, 1–25.

Brenner, H. 1964*a* The Stokes resistance of an arbitrary particle-ii an extension. *Chem. Eng. Sci.* **19**, 599–629.

Brenner, H. 1964*b* The Stokes resistance of an arbitrary particle-iii shear fields. *Chem. Eng. Sci.* **19**, 631–651.

Brenner, H. 1964*c* The Stokes resistance of an arbitrary particle-iv arbitrary fields of flow. *Chem. Eng. Sci.* **19**, 703–727.

Brenner, H. 1966 The Stokes resistance of an arbitrary particle- part v. symbolic operator representation of intrinsic resistance. *Chem. Eng. Sci.* **21**, 97–109.

Brenner, H. & O'Neill, M. E. 1972 On the Stokes resistance of multiparticle systems in a linear shear field. *Chem. Eng. Sci.* **27**, 1421–1439.

Bricker, J. M. & Butler, J. E. 2006 Oscillatory shear of suspensions of noncolloidal particles. *J. Rheol.* **50**, 711–728.

Butera, R. J., Wolfe, M. S., Bender, J. & Wagner, N. J. 1996 Formation of a highly ordered colloidal microstructure upon flow cessation from high shear rates. *Phys. Rev. Lett.* **77**, 2117–2120.

Carnahan, N. F. & Starling, K. E. 1969 Equation of state for nonattracting rigid spheres. *J. Chem. Phys.* **51**, 635–636.

Chan, D. & Powell, R. L. 1984 Rheology of suspensions of spherical particles in a Newtonian and non-Newtonian fluid. *J. non-Newtonian Fluid Mech.* **15**, 165–179.

Chen, S. & Doolen, G. D. 1998 Lattice Boltzmann method for fluid flows. *Annu. Rev. Fluid Mech.* **30**, 329–364.

Cheng, X., McCoy, J. H., Israelachvili, J. N. & Cohen, I. 2011 Imaging the microscopic structure of shear thinning and thickening colloidal suspensions. *Science* **333**, 1276–1279.

Chow, A. W., Sinton, S. W., Iwamiya, J. H. & Thomas, T. S. 1994 Shear-induced particle migration in couette and parallel-plate viscometers: Nmr imaging and stress measurements. *Phys. Fluids* **6**, 2561–2576.

Danckwerts, P. V. 1952 The definition and measurement of some characteristics of mixtures. *Appl. Sci. Res. A* **3**, 279–296.

Darabaner, C. L. & Mason, S. G. 1967 Particle motions in sheared suspensions xxii: Interactions of rigid spheres (experimental). *Rheol. Acta* **6**, 273–284.

D'Haene, P., Mewis, J. & Fuller, G. G. 1993 Scattering dichroism measurements of flow-induced structure of a shear thickening suspension. *J. Colloids Interface Sci.* **156**, 350–358.

Drazer, G., Koplik, J., Khusid, B. & Acrivos, A. 2004 Microstructure and velocity fluctuations in sheared suspensions. *J. Fluid Mech.* **511**, 237–263.

Durlofsky, L., Brady, J. F. & Bossis, G. 1987 Dynamic simulation of hydrodynamically interacting particles. *J. Fluid Mech.* **180**, 21–49.

Eckstein, E. C., Bailey, D. G. & Shapiro, A. H. 1977 Self-diffusion of particles in shear flow of a suspension. *J. Fluid Mech.* **79**, 191–208.

Egres, R. G., Nettesheim, F. & Wagner, N. J. 2006 Rheo-SANS investigation of acicular-precipitated calcium carbonate colloidal suspensions through the shear thickening transition. *J. Rheol.* **50**, 685–709.

Einstein, A. 1926 *Investigations on the theory of the Brownian movement*. E. P. Dutton and Company Publishers: New York, edited with notes by R. F

Fang, Z. W., Mammoli, A. A., Brady, J. F., Ingber, M. S., Mondy, L. A. & Graham, A. L. 2002 Flow-aligned tensor models for suspension flows. *J. Multiphas. Flow* **28**, 137–166.

Foss, D.R. & Brady, J.F. 2000 Structure, diffusion and rheology of brownian suspensions by stokesian dynamics simulation. *J. Fluid Mech.* **407**, 167–200.

Frank, M., Anderson, D., Weeks, E. R. & Morris, J. F. 2003 Particle migration in pressure-driven flow of a brownian suspension. *J. Fluid Mech.* **493**, 363–378.

Gadala-Maria, F. & Acrivos, A. 1980 Shear-induced structure in a concentrated suspension of solid spheres. *J. Rheol.* **24**, 799–814.

Gao, C. 2010 Three-dimensional measurements of microstructure and particle migration in suspension flows. PhD thesis, Lehigh University.

Gao, C. & Gilchrist, J. F. 2008 Shear-induced particle migration in one-, two-, and three-dimensional flows. *Phys. Rev. E* **77**, 025301.

Gao, C., Kulkarni, S. D., Morris, J. F. & Gilchrist, J. F. 2010 Direct investigation of anisotropic suspension structure in pressure-driven flow. *Phys. Rev. E* **81**, 041403.

Gao, C., Xu, B. & Gilchrist, J. F. 2009 Mixing and segregation of microspheres in microchannel flows of mono- and bidispersed suspensions. *Phys. Rev. E* **79**, 036311.

Gilchrist, J. F. & Ottino, J. M. 2003 Competition between chaos and order: Mixing and segregation in a spherical tumbler. *Phys. Rev. E* **68**, 061303.

Gondret, P. & Petit, L. 1996 Viscosity of periodic suspensions. *Phys. Fluids* **8**, 2284–2290.

Gopalakrishnan, V. & Zukoski, C. F. 2004 Effect of attractions on shear thickening in dense suspensions. *J. Rheol.* **48**, 1321–1344.

Happel, J. & Brenner, H. 1965 *Low Reynolds Number Hydrodynamics*, 1st edn. Prentice-Hall, Inc., Englewood Cliffs, N.J.

Heymann, L., Peukert, S. & Aksel, N. 2002 Investigation of the solidliquid transition of highly concentrated suspensions in oscillatory amplitude sweeps. *J. Rheol.* **46**, 93–112.

Hilborn, H. C. 1994 *Chaos in nonlinear systems*. Oxford University Press, New York.

Hill, K. M., Kharkhar, D. V., Gilchrist, J. F., McCarthy, J. J. & Ottino, J. M. 1999 Segregation-driven organization in chaotic granular flows. *PNAS* **96**, 11701–11706.

Hoffman, R. L. 1972 Discontinuous and dilatant viscosity behavior in concentrated suspensions.I. observation of a flow instability. *Trans. Soc. Rheol.* **16**, 155–173.

Hoffman, R. L. 1998 Explanations for the cause of shear thickening in concentrated colloidal suspensions. *J. Rheol.* **42**, 111–123.

Hoogerbrugge, P. J. & Koelman, J. M. V. A. 1992 Simulating microscopic hydrodynamic phenomena with Dissipative Particle Dynamics. *Europhys. Lett.* **19**, 155–160.

Horn, F. M., Richtering, W., Bergenholtz, J., Willenbacher, N. & Wagner, N. J. 2000 Hydrodynamic and colloidal interactions in concentrated charge-stabilized polymer dispersions. *J. Colloids Interface Sci.* **225**, 166–178.

Husband, D. M. & Gadala-Maria, F. 1987 Anisotropic particle distribution in dilute suspensions of solid spheres in cylindrical Couette flow. *J. Rheol.* **51**, 95–110.

Ito, K., Yoshida, H. & Ise, N. 1994 Void structure in colloidal dispersions. *Science* **263**, 66–68.

Jeffrey, D. J. & Acrivos, A. 1976 The rheological properties of suspensions of rigid particles. *AICHE J.* **22**, 417–432.

Jeffrey, D. J. & Onishi, Y. 1984 Calculation of the resistance and mobility functions for two unequal rigid spheres in low-Reynolds-number flow. *J. Fluid Mech.* **139**, 261–290.

Kalman, D. P. & Wagner, N. J. 2009 Microstructure of shear-thickening concentrated suspensions determined by flow-USANS. *Rheol. Acta* **48**, 897–908.

Kharkhar, D. V., McCarthy, J. J., Gilchrist, J. F. & Ottino, J. M. 1999 Chaotic mixing of granular materials in two-dimensional tumbling mixers. *Chaos* **9**, 195–205.

Kim, S. & Karrila, S. J. 1991 *Microhydrodynamics– principles and selected applications*. Butterworth-Heinemann, Boston.

Kim, S. & Mifflin, R. T. 1985 The resistance and mobility functions for two equal spheres in low-Reynolds-number flow. *Phys. Fluids* **28**, 2033–2045.

Kose, A., Ozaki, M., Takano, K., Kobayashi, Y. & Hachisu, S. 1973 Direct observation of ordered latex suspension by metallurgical microscope. *J. Colloid Int. Sci.* **44**, 330–338.

Krieger, I. M. 1972 Rheology of monodisperse latices. *Adv. Colloid Interface Sci.* **3**, 111–136.

Krieger, I. M. & Dougherty, T. J. 1959 A mechanism for non-Newtonian flow in suspensions of rigid spheres. *Trans. Soc. Rheol.* **3**, 137–152.

Krishnan, G. P., Beimfohr, S. & Leighton, D. T. 1996 Shear-induced radial segregation in bidisperse suspensions. *J. Fluid Mech.* **321**, 371–393.

de Kruif, C. G., van Iersel, E. M. F., Vrij, A. & Russel, W. B. 1985 Hard sphere colloidal dispersions: Viscosity as a function of shear rate and volume fraction. *J. Chem. Phys* **83**, 4717–4725.

Kulkarni, S. D. & Morris, J. F. 2009 Ordering transition and structural evolution under shear in brownian suspensions. *J. Rheol.* **53**, 417–439.

Ladd, A. J. C. & Verberg, R. 2001 Lattice-Boltzmann simulations of particle-fluid suspensions. *J. Statistical Phys.* **104**, 1191–1251.

Lamb, H. 1932 *Hydrodynamics*, sixth edn. Cambridge University Press, New York.

Leighton, D. T. & Acrivos, A. 1986 Viscous resuspension. *Chem. Eng. Sci.* **41**, 1377–1384.

Leighton, D. T. & Acrivos, A. 1987*a* Measurements of the shear induced coefficient of self-diffusion. *J. Fluid Mech.* **181**, 415–439.

Leighton, D. T. & Acrivos, A. 1987*b* The shear-induced migration of particles in concentrated suspensions. *J. Fluid Mech.* **181**, 415–439.

Lichtenberg, A. J. & Lieberman, M. A. 1983 *Regular and Stochastic Motion*. Springer, New York.

Lin, C. J., Lee, K. J. & Sather, N. F. 1970 Slow motion of two spheres in a shear field. *J. Fluid Mech.* **43**, 35–47.

Lyon, M. K. & Leal, L. G. 1998 An experimental study of the motion of concentrated suspensions in twodimensional channel flow. i. monodisperse systems. *J. Fluid Mech.* **363**, 25–56.

Maranzano, B. J. & Wagner, N. J. 2001 The effects of particle size on reversible shear thickening of concentrated colloidal dispersions. *J. Chem. Phys.* **114**, 10514–10527.

Maranzano, B. J. & Wagner, N. J. 2002 Flow-small angle neutron scattering measurements of colloidal dispersion microstructure evolution through the shear thickening transition. *J. Chem. Phys.* **117**, 10291–10302.

Maxey, M. R. & Riley, J. J. 1983 Equation of motion for a small ridged sphere in a nonuniform flow. *Phys. Fluid* **26**, 883–889.

Melrose, J. R. & Ball, R. C. 2004*a* "contact networks" in continuously shear thickening colloids. *J. Rheol.* **48**, 961–978.

Melrose, J. R. & Ball, R. C. 2004*b* Continuous shear thickening transitions in model concentrated colloids- the role of interparticle forces. *J. Rheol.* **48**, 937–960.

Merhi, D., Bossis, G., Lemaire, E. & Moukald, F. 2005 Particle migration in a concentrated suspension flowing between rotating parallel plates: Investigation of diffusion flux coefficients. *J. Rheol.* **49**, 1429–1448.

Mewis, J. & Wagner, N. J. 2009 Current trends in suspension rheology. *J. Non-Newtonian Fluid Mech.* **157**, 147–150.

Miller, R.M. & Morris, J.F. 2006 Normal stress-driven migration and axial development in pressure-driven flow of concentrated suspensions. *J. Non-Newton. Fluid Mech.* **135**, 149–165.

Miller, R. M., Singh, J. P. & Morris, J. F. 2009 Suspension flow modeling for general geometries. *Che. Eng. Sci.* **64**, 4597–4610.

Moraczewski, T., Tang, H. Y. & Shapley, N. C. 2005 Flow of a concentrated suspension through an abrupt axisymmetric expansion measured by nuclear magnetic resonance imaging. *J. Rheol.* **49**, 1409–1428.

Morinaga, T., Ohno, K., Tsujii, Y. & Fukuda, T. 2008 Structural analysis of "semisoft" colloidal crystals by confocal laser scanning microscopy. *Macromolecules* **41**, 3620–3626.

Morris, J. F. 2009 A review of microstructure in concentrated suspensions and its implications for rheology and bulk flow. *Rheol. Acta* **48**, 909–923.

Morris, J. F. & Boulay, F. 1999 Curvilinear flows of noncolloidal suspensions: The role of normal stresses. *J. Rheol.* **43**, 1213–1237.

Morris, J. F. & Katyal, B. 2002 Microstructure from simulated brownian suspension flows at large shear rate. *Phys. Fluids* **14**, 1920–1937.

Murray, C. A. & Grier, D. G. 1995 Colloidal crystals. *Am. Sci.* **83**, 238–245.

Murray, C. A. & Grier, D. G. 1996 Video microscopy of monodisperse colloidal systems. *Annu. Rev. Phys. Chem.* **47**, 421–462.

Muzzio, F. J., Meneveau, C., Swanson, P. D. & Ottino, J. M. 1992 Scaling and multifractal properties of mixing in chaotic flows. *Phys. Fluid A* **4**, 1439–1456.

Narumi, T., See, H., Honma, Y., Hasegawa, T., Takahashi, T. & Phan-Thien, N. 2002 Transient response of concentrated suspensions after shear reversal. *J. Rheol.* **46**, 295–305.

Narumi, T., See, H., Honma, Y., Suzuki, A. & Hasegawa, T. 2005 Response of concentrated suspensions under large amplitude oscillatory shear flow. *J. Rheol.* **49**, 71–85.

Newstein, M. C., Wang, H., Balsara, N. P., Lefebvre, A. A., Shnidman, Y., Watanabe, H., Osaki, K., Shikata, T., Niwa, H. & Morishima, Y. 1999 Microstructural changes in a colloidal liquid in the shear thinning and shear thickening regimes. *J. Chem. Phys.* **111**, 4827–4838.

Niederkorn, T. C. & Ottino, J. M. 1993 Mixing of viscoelastic fluids in time-periodic flows. *J. Fluid Mech.* **256**, 243–268.

Niederkorn, T. C. & Ottino, J. M. 1994 Mixing of shear thinning fluids in time-periodic flows. *AIChE Journal* **40**, 1782–1793.

Nir, A. & Acrivos, A. 1973 On the creeping motion of two arbitray-sized touching spheres in a linear shear field. *J. Fluid Mech.* **59**, 209–223.

Nott, P. R. & Brady, J. F. 1994 Pressure-driven flow of suspensions: simulation and theory. *J. Fluid Mech.* **275**, 157–199.

Ohtsuka, T., Royall, C. P. & Tanaka, H. 2008 Local structure and dynamics in colloidal fluids and gels. *EPL* **84**, 46002.

Ottino, J. M. 1989*a* *The Kinematics of Mixing*. Cambridge University Press, Cambridge, UK.

Ottino, J. M. 1989*b* The mixing of fluids. *Scientific American* **260**, 56–67.

Ottino, J. M. 1990 Mixing, chaotic advection and turbulence. *Annu. Rev. Fluid Mech.* **22**, 207–253.

Pan, W. X., Caswell, B. & Karniadakis, G. E. 2010 Rheology, microstructure and migration in Brownian colloidal suspensions. *Langmuir* **26**, 133–142.

Parsi, F. & Gadala-Maria, F. 1987 Fore-and-aft asymmetry in a concentrated suspension of solid spheres. *J. Rheol.* **31**, 725–732.

Phillips, R. J., Armstrong, R. C., Brown, R. A., Graham, A. & Abbott, J. R. 1992 A constitutive equation for concentrated suspensions that accounts for shear-induced particle migration. *Phys. Fluids A* **4**, 30–40.

Phung, T. N., Brady, J.F. & Bossis, G. 1996 Stokesian Dynamics simulation of Brownian suspensions. *J. Fluid Mech.* **313**, 181–207.

Pine, D. J., Gollub, J. P., Brady, J. F. & Leshansky, A. M. 2005 Chaos and threshold for irreversibility in sheared suspensions. *Nature* **438**, 997–1000.

Popova, M., Vorobieff, P., Ingber, M.S. & Graham, A.L. 2007 Interaction of two particles in a shear flow. *Phys. Rev. E* **75**, 066309.

Ramachandran, A. & Leighton, D. T. 2007 Viscous resuspension in a tube: The impact of secondary flows resulting from second normal stress differences. *Phys. Fluids* **19**, 053301.

Ramette, R. W. & Sandell, E. B. 1956 Rhodamine b equilibria. *J. Am. Chem. Soc.* **78**, 4872–4878.

Rampall, I., Smart, J. R. & Leighton, D. T. 1997 The influence of surface roughness on the particle-pair distribution function of dilute suspensions of non-colloidal spheres in simple shear flow. *J. Fluid Mech.* **339**, 1–24.

Ritz, J. B., Bertrand, F., Thibault, F. & Tanguy, P. A. 2000 Shear-induced particle migration in a short-dwell coater. *Chem. Eng. Sci.* **55**, 4857–4867.

Royall, C. P., van Roij, R. & van Blaaderen, A. 2005 Extended sedimentation profiles in charged colloids: the gravitational length, entropy, and electrostatics. *J. Phys.: Condens. Matter* **17**, 2315–2326.

Russel, W. B. 1980 Review of the role of colloidal forces in the rheology of suspensions. *J. Rheol.* **24**, 287–317.

Russel, W. B. 2009 Structure-property relations for the rheology of dispersions of charged colloids. *Ind. Eng. Chem. Res* **48**, 2380–2386.

Russel, W. B. & Gast, A. P. 1986 Nonequlllbrium statistical mechanics of concentrated colloidal dispersions: Hard spheres in weak flows. *J. Chem. Phys.* **84**, 1815–1826.

Russel, W. B., Saville, D. A. & Schowalter, W. R. 1989 *Colloidal Dispersions*. Cambridge University Press, Cambridge, UK.

Sierou, A. & Brady, J. F. 2001 Accelerated stokesian dynamics simulations. *J. Fluid Mech.* **448**, 115–146.

Sierou, A. & Brady, J. F. 2002 Rheology and microstructure in concentrated noncolloidal suspensions. *J. Rheol.* **46**, 1031–1056.

Singh, A. & Nott, P. R. 2000 Normal stresses and microstructure in bounded sheared suspensions via Stokesian Dynamics simulations. *J. Fluid Mech.* **412**, 279–301.

Stickel, J. J., Phillips, R. J. & Powell, R. L. 2006 A constitutive model for microstructure and total stress in particulate suspensions. *J. Rheol.* **50**, 379–413.

Stickel, J. J. & Powell, R. L. 2005 Fluid mechanics and rheology of dense suspension. *Annu. Rev. Fluid Mech.* **37**, 129–149.

Stone-Masui, J. & Watillon, A. 1968 Electroviscous effects in dispersions of monodisperse polystyrene latices. *J. Colloids Interface Sci.* **28**, 187–202.

Subia, S. R., Ingber, M. S., Mondy, L. A., Altobelli, S. A. & Graham, A. L. 1998 Modelling of concentrated suspensions using a continuum constitutive equation. *J. Fluid Mech.* **373**, 193–219.

Tanner, R. I. 2000 *Engineering Rheology*. Oxford University Press, Oxford, UK.

Wagner, N. J. & Brady, J. F. 2009 Shear thickening in colloidal dispersions. *Phys. Today* **62**, 27–32.

van der Werff, J. C. & de Kruif, C. G. 1989 Hard-sphere colloidal dispersions: The scaling of rheological properties with particle size, volume fraction, and shear rate. *J. Rheol.* **33**, 421–454.

Wu, Y. L., Derks, D., van Blaaderen, A. & Imhof, A. 2009 Melting and crystallization of colloidal hard-sphere suspensions under shear. *PNAS* **106**, 10564–10569.

Xi, C. & Shapley, N. C. 2008 Flows of concentrated suspensions through an asymmetric bifurcation. *J. Rheol.* **52**, 625–647.

Xu, B. & Gilchrist, J. F. 2010 Shear migration and chaotic mixing of particle suspensions in a time-periodic lid-driven cavity. *Phys. Fluids* **22**, 053301.

Yurkovetsky, Y. & Morris, J. F. 2006 Triplet correlation in sheared suspensions of brownian particles. *J. Chem. Phys.* **124**, 204908.

Zarraga, I. E., Hill, D. A. & Leighton, D. T. 2000 The characterization of the total stress of concentrated suspensions of noncolloidal spheres in Newtonian fluids. *J. Rheol.* **44**, 185–220.

Vita

I was born on August 10, 1979, as the only child to Mr. Ya-Qing Xu and Mrs. Ming-Lei Kang in the coastal city of Qingdao (also known as Tsing-Tao) in People's Republic of China. I attended the No. 1 and No. 2 Middle Schools in Qingdao for my secondary and high school, respectively. An ambition of being a scholar was developed during this time. I entered Beijing University of Chemical Technology in 1998 and obtained a degree of Bachelor of Science in Chemical Engineering & Process in 2002. I won some prizes for my performance in college, one of the most prominent being the Cheng Yuan Scholarship in 2001. After graduation I spent two years in Beijing in preparation for studying abroad. During this period I was employed by Beijing Wisemen Sci. & Tech. Development Corp. Ltd. for nine months from 2003 to 2004. My duty was to interface with our partner in Switzerland, translate documents and provide technical support to customers.

My academic life restarted in 2004 when I attended the National University of Singapore as a masters student. I worked on controller design under Dr. Min-Sen Chiu in the Department of Chemical & Biomolecular Engineering and was later awarded degree of Master of Engineering. I went on to get enrolled in the PhD program in Department of Chemical Engineering at Lehigh in 2006, under the direction of Dr. James F. Gilchrist. Colloidal science and suspension dynamics have since then become my central theme of research.

My publications include:

1) Mixing and segregation of microspheres in microchannel flows of mono- and bidispersed suspensions, C. Gao, B. Xu and J. F. Gilchrist, *Physical Review E*, **79**, 036311, 2009;

2) Shear migration and chaotic mixing of particle suspensions in a time-periodic lid-driven cavity, B. Xu and J. F. Gilchrist, *Physics of Fluids*, **22**, 053301, 2010;

3) Effect of Surface Nanotopography on Immunoaffinity Cell Capture in Microfluidic Devices, B. Wang, A. L. Weldon, P. Kumnorkaew, B. Xu, J. F. Gilchrist and X. Cheng, *Langmuir*, **27**, 11229-11237, 2011;

4) PID Controller Design Directly from Plant Data, X. Yang, B. Xu and M. S. Chiu, *Industrial & Engineering Chemistry Research*, **50**, 1352-1359, 2011.